Cand.Scient.

NTNU
Norwegian University of
Science and Technology
Faculty of Natural Sciences
and Technology
Department of Physics

Leif Ove Hansen

Disk Accretion and the Spin Evolution of Pulsars

Trondheim, June 2007

NTNU

Disk Accretion and the Spin Evolution of Pulsars

by
Leif Ove Hansen

Cand.Scient-Thesis in Astrophysics at
Institute of Physics
The Norwegian University of Science And Technology (NTNU)

June 2007

"Directly overhead in the daytime sky,
a new, strange star was suddenly seen..."

Chinese astronomer, July 4th, 1054AD
(Annals of the Sung Dynasty).

Contents

Preface

The present work is a dissertation for the Cand.Scient (Master)-degree in Astrophysics at the Norwegian University of Science and Technology (NTNU).

Professor Erlend Østgaard suggested the theme for my thesis, and also was my advisor during the first part of the work. But for unfortunate medical reasons he was not able to continue. However, his presence during years of studies is truly appreciated, both by me and many other students. In his absence I have benefited from cooperation with my new advisor professor Jan Myrheim. Also thanks to Tommy Øvergaard in the neighbouring office for acknowledgement and inspiration.

I am also indebted to NAV and Prima (Martin Hokstad and Berit Stenersløkken) for all support. Without their goodwill this thesis would probably never have been completed. Also thanks to Sylvi Vefsnmo and the Department of Physics.

I would also like to thank my parents for standing up to me all these years, through a long and very winding road.

Summary

This thesis is a theoretical investigation and inquiry into the general theory of accretion disks, and the connection between this theory and the spin-up evolution of accreting X-ray pulsars.

In Chapter 1, an historical introduction to the discovery of X-ray sources originating from beyond the solar system is given. The identification of some of these systems as binary systems with a mass transfer from an evolving star, onto a compact object is important in this context. Also observations that lead to the idea that some of these mass transfer systems contain magnetic neutron stars (pulsars) are discussed. Since the accretion disk model is merely a paradigm (there exist no *direct* proof as to the existence of these disks), arguments in support of this model is given.

Once the accretion disk model is established, different modes of mass transfer is discussed in Chapter 2. The most important (since it will transfer the most angular momentum) is Roche lobe overflow. Also mass transfer by a stellar wind is considered. By defining low mass X-ray binaries (LMXB) and high mass X-ray binaries (HMXB), the important differences between these two types of X-ray binary systems are made clear. Finally the essential Eddington luminosity, which is considered to be a maximum luminosity (and thereby also a maximum mass transfer rate) is calculated.

The standard theory of thin Keplerian disks is established in Chapter 3, and a model is constructed and analyzed. This is the version of the disk in the unperturbed state without the pulsar magnetic field. The principal mechanics of such a disk, which concerns the internal viscous torques to remove angular momentum, is discussed. Since the mechanism that generates the viscosity in such disks is dubious, the α-parameterization is used. Equations for general thin disks are discussed, and then through a choice of equation of state, opacity and energy transport, a set of disk equations that govern the disk are presented for three different regions of the disk. Analytical solutions for the disk parameters are then given, in the same form as Shakura-Sunyaev disks. Many of the assumptions that went into the construction of the model are then justified, analytically and with numerical plots. The model returns good and consistent values, both regarding

timescales and disk parameter values. The exception is in the inner region of the disk, where the thin disk assumption seems to break down, and also other characteristics built into the disk model become invalid. This is of no concern however, since calculations of the disruption radius r_0 made later (in Chapter 4), indicate that the pulsar magnetic field will disrupt the disk before this inner region, or at least make the disk solutions in this region invalid in any case.

The disk spectra radiated from such a disk are essential from a observational point of view. Therefore an attempt to calculate the dominant spectra from the different parts of disk is made. This shows that the outer parts of the disk can be well approximated by a blackbody spectrum, while the middle region can be described by a modified blackbody spectrum. The spectrum from the inner region (which radiate with highest intensity) can be crudely described by a Wien cut-off spectrum. The concept of irradiated disks, and other influences on the spectra are discussed. Towards the end of Chapter 3, a short outline of the essentials of disk stability is included for completeness, since this is a vital area of accretion disk research. It is here shown that the inner region of the disk model (where the radiation pressure is dominant) is thermally unstable. Finally a short presentation of alternative disk models is given, such as ADAF and optically thin disks.

In Chapter 4, the torque exerted onto the star by the accretion disk and the interaction between the disk and the magnetic field of the pulsar, is investigated. The essential assumption is that the magnetic coupling between the disk and the dipolar magnetic field of the star, is of such a nature that the field is *threaded* onto the disk. This means that the magnetic field lines are frozen into the disk plasma, and thus will follow the fluid elements of the gas. If the disk and the magnetic field (which follows the rotation of the star) is not rotating at the same angular velocity, then there will be a shearing between the two. Generally, this shearing motion will generate a toroidal magnetic field B_ϕ inside the disk, and this causes a torque on the star. It is proved in Chapter 4 that the perturbation to the poloidal component B_z of the magnetic field inside the disk, is negligible, and this simplifies the calculations of the torques considerably.

The value of the torque (negative, positive or zero) at a certain radius depends on the relative size of the radius compared to the corotation radius r_{co}. All the important radii and their relation to the value of the torques, are then defined, including the disruption radius r_0. Also the important fastness parameter ω_s and the dimensionless fastness function $n(\omega_s)$ are defined, and their relation to the torque is analyzed. The validity of the model is then checked by comparing with pulsar data for 10 well known X-ray binary pulsars, and is found to be satisfactory.

A screening factor is then introduced, and an expression for the toroidal magnetic field

is found. On basis of the solutions for the middle (gas pressure and electron scattering dominated region) for the thin disk model developed in Chapter 3, the total torque on the pulsar is calculated. From this, a rather high value for the critical fastness parameter $\omega_c \simeq 0.96$ is estimated, and the equilibrium spin period P_{eq} is found. The link between the torque on the star, and the *variation* of the important parameters P (pulsar spin), $\dot{M}$ (mass accretion rate) and B (magnetic field strength) is outlined, and then calculated numerically by using an expression for $x_0 = r_0/r_{co}$. The latter understanding is then used to define and find a spin-up line for accreting X-ray pulsars. This spin-up line is plotted in Chapter 5, and found to be in agreement with regular pulsar data collected from the ATNF Catalogue. The dramatic and unexpected torque reversals found in such systems recently by the Compton Gamma Ray Observatory (CGO) are then discussed, and a few possible explanations are given.

The expression for P_{eq} found in Chapter 4 indicates that if the magnetic field of the pulsar is weak enough, then the pulsar could be spun up to values of P_{eq} that are in the order of milliseconds. This is in support of the idea that such accretion X-ray pulsar systems might be the progenitors of millisecond pulsars. In Chapter 5, the validity of this theory is discussed, generally and in light of the results from Chapter 4. The millisecond accretion X-ray pulsars that have been discovered during the last 7-8 years (by the NASA X-ray Timing Explorer (XTE) and Beppo/SAX satellite), and that might be said to represent a missing link here, are also discussed (and data are given in Appendix D).

In this thesis, all numerical calculations, figures and plots have been conducted using Maple 9.5. The exceptions are the more illustrative graphical figures Fig. 2.1, 3.1, 3.2, 4.1 and 4.2, where COREL Representations have been used.

Chapter 1

Discovery and Identification

1.1 The Birth of X-ray Astronomy

A new era in astronomy was born on June 18 1962, when an Aerobee-rocket carrying several Geiger-counters lifted off from New Mexico, USA. The objective of the experiment was to search for X-rays emitted by fluorescence from the Moon. Other X-ray sources were however soon discovered, originating in the constellation Scorpio. The source *Sco X-1* was the first clear evidence of X-rays coming from beyond the solar system. The intriguing possibility that there might be intense sources of X-rays other than the Sun acted as a catalyst in theoretical speculations, and it also encouraged experimenters to make further observations.

During the 1960's, astronomers carried out observations during brief rocket- and balloon flights that lifted experiments above the Earth's atmosphere. These flights confirmed the Aerobee observations, refined earlier measurements and identified a number of strong X-ray sources. The Crab nebula eventually became the first object outside the solar system to be identified as an X-ray source. It was however much more difficult to identify the strong point-source that had been discovered in the Scorpio constellation. Unlike the Crab nebula, there was no obvious sign of a supernova remnant in the area, and thus the nature of the X-ray source remained a mystery.

Sco X-1 Identification

In 1966 however, an optical counterpart to the *Sco X-1* source was located, with a faint blue 12^{th}-13^{th} magnitude star as a likely candidate. The *Sco X-1* system had an X-ray output 1000 times larger than the output in the optical area, and this made it such an unusual object that some previously unrecognized energy-mechanism was assumed to provide the intense X-ray radiation. In this manner optical astronomy provided the clues as to the energy mechanism in the *Sco X-1* source. It was in fact two objects in orbit

around their common center of gravity.

The theoretical activity concerning the nature of *Sco X-1* thus gathered momentum. Taking into consideration the binary nature of *Sco X-1*, it was speculated that the X-ray emission originated from high-temperature gas flowing onto a compact object from a close binary companion [1]. For this mechanism to work efficiently the star on which the material falls must be very much smaller, but of comparably solar mass. Due to the observed soft X-ray spectrum from *Sco X-1* many held that the accretion process was driven by a white dwarf [2], which was the only known compact object at that time with any degree of observational verification. Following these developments others argued that gas flowing onto a compact object from a binary companion generally would have too much angular momentum to flow radially (spherical). Instead the gas would form a thin accretion-disk around the compact object, with approximately Keplerian circular velocities and a small inward drift [3].

Discovery of Radio Pulsars

Although many contributions to the theory and possible existence of compact objects were made, the theoretical work on these objects proceeded with moderate pace until the discovery of radio-pulsars by Bell & Hewish in 1967. They observed rapid and regular pulsations in a galactic radio source, and this was interpreted as resulting from beams of radio waves emitted in the magnetic field of a rapidly rotating neutron star [4]. In spite of the expanding theoretical effort to explain the newly discovered galactic X-ray sources, there were no compelling evidence at that time, that these sources had anything to do with close binary systems and compact objects. But the discovery of pulsars made the notion of such systems a lot more credible.

By the end of the decade over 20 X-ray sources had been discovered, showing a great variety of properties. The temporal structure of the radiation was found to be highly variable on every timescale from milliseconds to years, and the variability was both random and periodic. The great majority of the sources were situated near the galactic plane, with distances ranging from 50 pc to 10 kpc, establishing the sources as galactic objects. Several strong extra-galactic X-ray objects have also been observed and identified over the last decades, giving X-ray astronomy recognition as relevant in the study of the most distant objects in the Universe as well.

1.2 Identification of X-ray Binaries

Intrigued by these preliminary discoveries astronomers began designing an Earth-orbiting X-ray satellite, that could make observations continuously. The Uhuru-satellite was en-

tirely devoted to non-solar X-ray observations, and revolutionized our understanding of cosmic X-ray sources and compact objects. And when the Uhuru-program was shut down in 1973, the catalog consisted of 339 X-ray sources.

1.2.1 Pulse Period and Spin Up

The discovery of pulsars was still fresh in everyone's mind, so the Uhuru-team was very excited to detect X-ray pulses coming from the constellation Centaurus in early 1971. The X-ray pulses had a regular period of 4.84 seconds. A few months later, similar pulses were discovered in the constellation Hercules, they had a period of 1.24 seconds [5]. These two sources were designated *Cen X-3* and *Her X-1*. Because the periods of these two X-ray sources were so short, it was suspected that they were rapidly rotating neutron stars. X-ray pulsations from luminous X-ray binaries provide a clear signature of accretion onto a magnetized neutron star. If the magnetic field of the neutron star is strong ($\gtrsim 10^8$ G), the inflowing material from the donor star can be channeled towards the magnetic poles, where it gives off most of its energy in the form of X-rays. If in addition, the magnetic and rotational axes are misaligned, this will create an X-ray beam which will sweep across space as the star rotates. If this beam sweeps across our line of sight, X-ray pulsations will be observed with the same period as the rotational period of the magnetic field of the star.

Spin-Up

The pulse period histories of a number of X-ray pulsars have been reliably charted for almost three decades now [6]. For some systems this monitoring has revealed a linear decrease of the pulse period with time, so-called *spin up*. The change of the pulse period in these cases is not always monotonic on short timescales, but the trend towards a secular decrease in pulse period seems evident [7]. Other X-ray pulsars show an opposite tendency, where the pulse period in fact increases, so-called *spin down*. This can be understood in terms of torques, which will be exerted by the accretion flow if the right conditions are present. Many such spin-up systems have been observed among accreting X-ray binary pulsars, and it seems reasonable to suppose that if conditions allow spin up to proceed far enough, a millisecond-period pulsar may be the result [8]. In view of this, some *millisecond pulsars* (spin period < 10 ms) are believed to have acquired their rapid spin via spin-up, during a phase of accretion from their companions[1]. Due to the estimated timescales at which these torques are assumed to operate, it is expected that this spin up phase may have to be of the order of $\sim 10^9$ years to create a millisecond pulsar.

[1] In 1998 the pulsar *SAX J1808.4-3658* was discovered. This pulsar has a pulse period of $\sim$ 2.5 ms and is orbiting a low-mass star with a very small orbital period $\sim$ 2 hours, which makes this an ultracompact binary system [9]. We shall return to this very interesting system later

1.2.2 Orbital Period

It soon became clear that the *Cen X-3* and *Her X-1* systems (and others) were not ordinary radio-pulsars like the Crab-pulsar. When they were observed for several days, it became evident that in addition to the pulsations, their X-ray emission was being cut off on a regular basis. The *Her X-1* source turns off for ~ 6 hours every 1.7 days. Apparently *Her X-1* is an eclipsing binary, and it takes ~ 6 hours for the X-ray source to pass behind its companion star. Moreover, careful timing of its X-ray pulses shows a periodic Doppler-shifting every 1.7 days, which is direct evidence of orbital motion about a companion star. Careful optical searches of the location of *Her X-1* soon led astronomers to a variable dim star with excess emission in the UV-region, that had already been cataloged as *HZ Her*. The apparent magnitude of this star varies between 13 and 15 (due to X-ray heating from the compact object), with a period of 1.7 days. Because this period is exactly the same as the orbital period of the X-ray source, one can conclude that *HZ Her* is the companion star around which *Her X-1* orbits [5].

Putting all pieces together, it was realized that the pulsating X-ray sources *Cen X-3* and *Her X-1* are binary systems in which one of the components is a pulsar, and the other visible component is an ordinary star. Similar conclusions have, as we shall see below, been drawn for many non-pulsating X-ray sources containing a white dwarf or black hole.

1.2.3 Non-Pulsating X-ray Binaries

The list of possible galactic X-ray source-candidates includes all three kinds of known compact objects. A large part of our information about these compact objects has been derived from the studies of X-ray binary sources. As for X-ray pulsars, knowledge of pulse profiles, pulse periods and orbital parameters from such systems provides key information regarding the physics of neutron stars in general. It is often possible to determine with some degree of confidence, the type of compact object present in an X-ray binary.

If consistent data on the mass of the components of a binary system exists, the nature of the compact object might be inferred from that. The theory of compact objects gives limiting values on the possible masses of compact objects, and we know that a white dwarf cannot have a mass exceeding the Chandrasekhar-limit ($\simeq 1.4\, M_\odot$). The maximum mass for neutron stars is however less certain, but probably smaller than $3\, M_\odot$ [10]

Cyg X-1

Considerations of the non-periodic, rapidly varying binary X-ray source *Cyg X-1* are conclusive [11]. The high mass (significantly higher than $5\, M_\odot$) inferred from this source from the combined optical and X-ray data, excludes the possibility of a white dwarf or

a neutron star. It is this, together with the compact nature of the object, that leads to the identification of the *Cyg X-1* X-ray source as a black hole. The nature and detailed structure of such objects are uncertain. But the fact remains: *Cyg X-1* and several other candidates, are with high certainty not a white dwarfs or neutron stars, but they are almost definitely some kind of compact object.

1.3 The Accretion Disk Model

As I mentioned earlier, the favored mechanism for explaining the observed behavior of these new systems was a gas accretion-flow from the visible star onto the compact object. When the gas falls in the gravitational well of a compact object like a neutron star/black hole, a substantial gravitational energy is lost. In most cases the gas will have too much angular momentum to fall directly in, and thus the accreting gasflow would form a disklike structure around the compact object. In 1969 Lyndon-Bell [12] proposed the concept of a *viscous* accretion disk. Here the gravitational energy is transformed, through an internal viscosity, into heat and radiation as the gas spirals towards the compact object.

It is important to realize however that the general description of an accertion disk (and certain other modes of mass-transfer) is itself a phenomenological model. Observations, across the whole spectrum, provide the primary data, but they are not immediately unambiguous. No one has ever directly imaged an accretion disk in a binary X-ray source, in the sense of producing a resolved photograph of such a system. However in spite of the lack of direct observational evidence, the accretion model for X-ray binaries must be credited considerable weight. This model, in addition to basic physical principles, can explain many qualitative and quantitative details in the observed characteristics of these sources:

- The rapid variability of the X-ray emission on short timescales implies a small emitting region. An object cannot be observed to vary in brightness faster than the time it takes light to travel across the object. It is a fundamental characteristic of astronomical objects that the larger they are, the less rapidly they can vary.

- Many of the objects are positively identified to be in binary systems, with identified optical components orbiting invisible counterparts.

- Mass accretion onto a compact object, especially a neutron star or a black hole, is an extremely efficient means of converting released gravitational potensial energy into radiation. Imagine a mass m falling from infinity onto a neutron star of radius R and mass M. If we define its potensial energy to be 0 at $r \rightarrow \infty$, then the loss in potential energy of the mass m, which equals the maximum released energy is

$$\Delta E_{acc} = \frac{GmM}{R} = Gm\left(\frac{M}{R}\right) \tag{1.1}$$

If this infall takes place in an accretion disk, then half of the energy will be released as the matter spirals inwards, while the other half will be released as the matter collides with the stellar surface or interacts with the neutron star magnetic fields. In other words we have $L_{disc} = L_{surface} = \frac{1}{2}L_{acc}$. If we for a neutron star assume: radius $R \sim 10\,\mathrm{km}$ and $M \sim 1\,M_{\odot}$, this gives

$$\frac{\Delta E_{acc}}{\Delta E_{mat}} = \frac{Gm\left(\frac{M}{R}\right)}{mc^2} = \frac{G}{c^2}\left(\frac{M}{R}\right) \simeq 0.15 \tag{1.2}$$

Considerably larger than for nuclear fusion ($\lesssim 1\%$).

- The observed Doppler-shifts in certain accretion binaries are consistent with a rotating disk of optically thin gas in the system. [13]. These observations can only be made in systems where the disk-light dominates all other system components at the relevant wavelengths. The only systems where such conditions are met are the cataclysmic variables (CV), in which the accreting object is a white dwarf and the mass donor is a small faint low-mass star. The other X-ray binaries (neutron star/black hole) largely fail to satisfy these conditions. For OB-systems the luminosity of the mass donor (mostly UV & optical) will completely swamp the disk contribution. The accretion luminosity (almost entirely hard X-rays) in these systems gives information about the accretion process very close to the compact object, but very little about possible disk flow.

- In *Her X-1* cyclic modulations of the overall X-ray and optical flux, that are not related to the orbital period, have been observed. This lends further qualitative evidence for an accretion disk in this systems, as this cycle can be interpreted as occultations of the X-ray source by a precessing and tilted accretion disk. This cycle in *Her X-1* has a period of 35 days [5].

A profound interpretation, supported by these facts, is:

Despite the great variation in the observed phenomena, it appears possible to describe almost the entire zoo of variable galactic X-ray sources in a general standard model: The accretion of gaseous matter in binary systems, consisting of a compact object and a non-compact donor star.

The accretion model (disk accretion in particular), has in general been instrumental to the understanding of many active phenomena in the Universe, such as the formation of

planetary systems, the evolution of binary stars, the production of astrophysical jets and perhaps even the formation of galaxies. Several large-scale accretion disks have been directly observed around young stars (the protoplanetary dust-disk around *β-Pictoris)*, and the Hubble Space Telescope reveals images of parsec-scale disks in the cores of active galactic nuclei (AGN). The most famous accretion disk of all is probably the rings of Saturn, where the disk is so gas poor its angular momentum transport is dominated by solid body collisions and disk-moon gravitational interactions. These cases makes the notion of various types of accretion disks in many systems, including X-ray binaries, more credible.

Chapter 2

Interacting Binary Systems

2.1 The Roche Model for Close Binary Systems

The majority of the stars that make up our galaxy are members of binary systems, and the stars in these systems are usually well separated. However, when either of the stellar radii is of the same order of magnitude as the orbital radius and/or one of the components is a neutron star or black hole, the presence of a near companion can dramatically alter the stars' appearance and evolution. The problems on the structure of such close binary systems were first studied by the 19^{th} century French mathematician Edouard Roche in connection with the destruction (or survival) of planetary satellites, and is usually associated with his name. The essence of the Roche approach is to consider the orbit of a test particle in the gravitational potential due to two massive bodies orbiting each other under the influence of their mutual gravitational attraction. The two bodies (in our case, two stars) execute Keplerian orbits in a plane, about each others common center-of-mass (CM), and the Roche problem assumes these orbits to be circular[1]. Another restriction on the Roche problem is the assumption that the two stars can be regarded as point masses for dynamical purposes (this is normally an excellent approximation).

We take the masses of the two objects to be M (neutron star) and M_d (donor star), and M_d will lie in the range $0.1 - 100\,M_\odot$ for most known types of genuine stars. Fig. 2.1 is drawn for $q = M_d/M = 4$, and thus the neutron star appears as the object to the right. The binary separation a is then given in terms of the fundamental observational quantity the binary period P, through Kepler's law:

$$4\pi^2 a^3 = G(M + M_d)P^2 \tag{2.1}$$

It is convenient to work in a frame of reference rotating with the binary system, with

[1]This is usually a good approximation for binary systems, since tidal effects tend to circularize originally eccentric orbits on timescales that are short compared to those relevant to our problem.

angular velocity $\omega = 2\pi/P = \sqrt{G(M + M_d)/a^3}$ relative to an inertial frame. The forces acting on a test particle in the system, as seen by an observer rotating with the system, appear to be

$$\boldsymbol{F}_{test} = \boldsymbol{F}_M + \boldsymbol{F}_{M_d} + \boldsymbol{F}_{centrifugal} + \boldsymbol{F}_{coriolis} \tag{2.2}$$

The last two terms take account of the centrifugal and Coriolis forces, that are introduced as a result of our frame of reference (these are "pseudoforces" and vanish in an inertial frame). The first two terms of course, are the Newtonian gravitational attraction from the individual stars. We introduce the Roche potential $\Phi_R(\boldsymbol{r})$ given by

$$\Phi_R(\boldsymbol{r}) = -\frac{GM}{|\boldsymbol{r} - \boldsymbol{r}_c|} - \frac{GM_d}{|\boldsymbol{r} - \boldsymbol{r}_d|} - \frac{1}{2}(\boldsymbol{\omega} \times \boldsymbol{r})^2 \tag{2.3}$$

where $\boldsymbol{r}_c$ and $\boldsymbol{r}_d$ are the position vectors of the compact object and donor star (their centers). Φ_R includes the effects of both gravitational and centrifugal forces (caused by the orbital motion), but some of the forces acting on flowing mass in the system, in particular the velocity dependent Coriolis-force $\sim (\boldsymbol{\omega} \times \boldsymbol{F})$ is not represented. To calculate the detailed motion of mass in the system, we need to consider the Coriolis-force.

However, we gain considerable insight into accretion problems by plotting the equipotential surfaces of Φ_R and, in particular, their two-dimensional sections in the orbital plane. This is seen in Fig. 2.1.

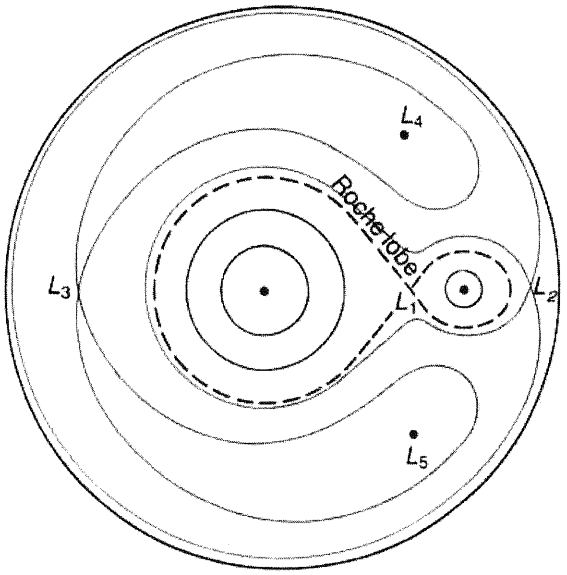

Fig. 2.1 *Sections of the Roche equipotentials Φ_R = constant, in the orbital plane of a binary system with mass ratio $q = 4$.*

The shape of the equipotentials is governed entirely by the mass ratio q, while the overall scale is given by the binary separation a. Fig. 2.1 is drawn for $q = 4$, but its qualitative features apply for any realistic mass ratio. Close to each star the potential is dominated by the gravity of that star, and the equipotential surfaces are spheres around the center of the star. Further out, the equipotential surfaces are deformed, and this is shown as highly non-spherical contours.

Lagrange Points

One unique surface intersects itself at the point L_1, called the *inner Lagrange point.* This surface defines two regions, one surrounding each star, which are called *Roche lobes.* Equipotential surfaces surrounding only one star lie within that star's Roche lobe, but surfaces outside a Roche lobe will surround both stars in most cases. At L_1, the potential reaches a critical point where $\nabla\Phi_R(\boldsymbol{r}) = 0$, which means that there is no force $\boldsymbol{F} = -\nabla\Phi_R(\boldsymbol{r})$ acting on a particle at rest there. The potential Φ_R may be regarded as having two deep valleys centered at $\mathbf{r}_c$ and $\mathbf{r}_d$ (the values of Φ_R are shown on Fig. 2.1), and the figure shows how these two valleys are connected through the saddle point L_1. To continue the analogy: L_1 is like a high mountain pass between two valleys. This means that material inside one of the two lobes in the vicinity of L_1, finds it much easier to pass through L_1 into the other lobe than to escape the critical surface. At other similar critical points of the potential, L_2 and L_3, the other lobes "opens up" much like the Roche lobes does at L_1. The last two Lagrange points in the binary system are the so-called "Trojan-asteroid"-points L_4 and L_5.

2.2 Mass-Transfer Mechanisms

There are three main reasons many binaries transfer matter at some stage of their evolutionary lifetimes:

- In the course of its evolution, one of the stars in a binary system may increase in radius, and/or the binary separation shrink. This may lead this star to fill its Roche lobe, to the point where the gravitational pull of the companion can remove the outer layers of its envelope *(Roche lobe overflow).*

- One of the stars may, at some evolutionary phase, eject much of its mass in the form of a stellar wind. Some of this material may be captured gravitationally by the companion *(Stellar wind accretion).*

- There is a third well-known type of mass loss among ordinary stars: the irregular outburst of equatorial mass-ejection observed in rapidly rotating B-stars, so-called B-emission stars *(Irregular equatorial mass loss).*

The detailed origin and evolution of such close binary systems are issues that generate a lot of scientific activity. The compact objects in X-ray binaries are remnants of relatively massive stars that evolved in a binary. Our understanding of the origin and evolution of X-ray binaries is thus based in good part on our understanding of the evolution of single massive stars. It is adversely affected by the appreciable uncertainty in our knowledge of the later evolutionary stages of such stars. Our knowledge about the effects of a supernova on such binary systems are for example, quite limited. Aspects specifically related to binaries include mass transfer between the stars, mass loss from the binary and evolution of stars that have lost or gained an appreciable fraction of their mass. We are here however mainly concerned with the basic mass-transfer mechanisms, which in some way are relevant to the study of the accretion process itself.

2.2.1 Roche Lobe Overflow

The most common expulsion mechanism is expansion of the donor star M_d beyond its critical equipotential lobe. The outer part (atmosphere) of the donor star then lies very close to L_1, and any perturbation of this material will cause it to flow into the Roche lobe of the neutron star, where it is quickly captured. The result is a gas stream from L_1 towards M.

In many systems the donor star has such a low mass that its main sequence lifetime exceeds the Hubble time, and the evolutionary expansion-mechanism cannot operate. Another possible catalyst for Roche lobe overflow is decrease in binary separation a, which may arise from loss of orbital angular momentum. A variety of effects can give $\dot{J} < 0$: in short-period systems gravitational radiation is efficient, and so is the loss of angular momentum through a stellar wind. In some systems with eccentric orbits, the Roche lobe overflow occurs only when the binary separation is minimal (at perigee), even though for most of the orbit the stars are too far apart for accretion to occur. This gives rise to highly transient X-ray sources.

Non-Rotating Frame

As matter flows through the L_1-point, the binary system rotates steadily with a period P (angular velocity $\omega = 2\pi/P$) around the CM. The flowing gas however, stops co-rotating with the system once it is removed from the stellar surface of the donor. In a non-rotating frame, the gas-stream thus appears to move with an velocity orthogonal to the line of centers as it emerges from L_1 (unless the binary period is very long). Further, it can be shown that the pressure forces driving the gas through L_1, and thus giving it a $v_{\perp}$, can be neglected in the trajectory calculations [14]. As the $v_{\perp}$ is much smaller than the velocities acquired during the free-fall towards the neutron star, the initial conditions

near L_1 have little effect on the trajectory, which therefore is essentially identical for all test particles in the flow. The stream will thus follow a ballistic trajectory determined by the Roche-potential Φ_R (gravitation + rotation) alone. If we assume that *before* it entered orbit, the gas had little opportunity to lose its initial angular momentum, it will tend to the orbit of lowest energy for a given angular momentum, i.e. a circular orbit. We thus expect the gas to start orbiting the neutron star in the binary plane at a radius R_d, such that the Keplerian orbit at R_d has the same specific angular momentum J as the transferring gas had on passing through L_1. Equating forces in this circular orbit gives

$$R_d = \frac{J^2}{GM} \tag{2.4}$$

The angular momentum J is given by the system parameters a and q, and in Fig. 2.1 we would have $R_d = 0.06a$. R_d is always (typically a factor 2-3 times) smaller than the Roche lobe-radius R_L of the accreting object [14]. The captured material will thus orbit well inside the Roche lobe, unless the accreting object already occupies this space, i.e. if its radius $R > R_d$. In systems where the accreting star is extended, for example a main-sequence star, it is quite possible that $R > R_d$. In this case the gas stream from the donor would hit the accretor directly. For X-ray binaries however, the accreting object is always a compact star, for which we have

$$R \ll R_d \tag{2.5}$$

for all realistic binary parameters. It is thus clear that in the Roche lobe overflow scenario, the captured plasma will always possess sufficient angular momentum to form an accretion disk around the compact object.

2.2.2 Stellar Wind

In many X-ray binaries the mass-donating star does not fill its Roche lobe (detached systems), and the compact component must accrete from a wind off the star. Massive stars may expel significant amounts of gas steadily in a stellar wind. These forms of expulsion may well be active in addition to Roche lobe overflow [15]. Indeed, any combination of them is conceivable for stars whose mass is not too low.

The stellar wind consists of particles (electrons and ions) that are driven out from the donor star at highly supersonic speeds. If we equal the wind speed with the escape velocity from the surface of the star we get (with R_{don} as the donor star radius)

$$v_w(r) \gtrsim v_{esc}(R_{don}) = \left(\frac{2GM_d}{R_{don}}\right)^{\frac{1}{2}} \tag{2.6}$$

For typical parameters, v_w is at least a few thousand kilometers per second. The wind particles which pass so close to the neutron star that their kinetic energy is less than the gravitational potential energy, will be captured and ultimately accreted by the neutron star. This gives

$$r_{acc} \simeq \frac{2GM}{v_{rel}^2} \tag{2.7}$$

where $v_{rel}^2 = v_w^2 + v^2$ (v is the neutron star orbital velocity, which may be substantial). The captured wind thus forms an accretion-cylinder where material within the radius r_{acc} will fall in on the neutron star, forming a bow shaped shock-front around it.

The captured wind material has rather low specific angular momentum compared with mass overflowing the Roche lobe, it is therefore difficult, on general grounds, to decide whether disc-formation conditions are satisfied. The captured gas always has *some* angular momentum with respect to M, but it may not be sufficient to form an accretion disk, in which case we have more or less spherical accretion.

However, accretion by stellar wind is an inherently less efficient process than Roche lobe overflow. Since the stellar wind is approximately isotropic, mass leaves the star in all directions, not just towards the accretor, and will usually escape the system unless it passes close to M. If the wind is emitted over a solid angle Ω and has total mass-loss rate $\dot{M}_w$ this implies an accretion rate

$$\dot{M} \sim \frac{\pi r_{acc}^2}{\Omega a^2}\dot{M}_w \tag{2.8}$$

In most X-ray binaries the winds are isotropic so $\Omega = 4\pi$, and have $v_w \sim 10^3\,\mathrm{km\,s^{-1}}$ ($\Rightarrow$ $r_{acc} \sim 10^8\,\mathrm{m}$. Setting the period $P \sim 10$ days (in some cases it is only a few days, or as high as ~ 100 days) gives $a \sim 10^{10}\,\mathrm{m} \gg r_{acc}$. This means that only a small fraction $\sim 10^{-4}\,\dot{M}_w$ of the plasma ejected from M_d is gravitationally captured by M. It is thus only because the mass-loss rates themselves are substantial, that sources powered in this way are observable.

2.2.3 Irregular Equatorial Mass Loss

Rapidly rotating B-type stars show, at irregular time intervals, eruptive outbursts of equatorial mass which produces a rotating ring of gas around the star. Some of these

stars may be rotating as fast as $\sim 70\%$ of the break-up velocity. Mass ejection is usually intrinsic to the B-star (i.e. it is independent of the presence or absence of a companion star). The star can appear as a normal main-sequence B-star for many years and suddenly go through a B-emission phase, becoming a Be-star for periods ranging from weeks to many years, while others are more or less permanent Be-stars.

If such a Be-star has a neutron star companion, this can suddenly become a bright X-ray transient when the B-star goes through a B-emission phase, and the matter in the ejection ring (or disk) is transferred onto the neutron star.

2.3 LMXB and HMXB

Binary systems are often divided into two main categories (with several subclasses):

- **LMXB**
  In the low-mass X-ray binary systems ($M_d \lesssim 2\,M_\odot$), the primary star is later than type A, usually G, K or M. A late type star does not have a natural stellar wind strong enough to power the observed X-ray spectra, and significant mass transfer is considered only to occur through Roche lobe overflow[2] [16]. The spectral features of the late type star are usually outshone by the reprocessing, at optical wavelengths, of the X-ray flux intercepted by the accretion disk. X-ray heating of the accretion disk thus dominates the optical light, and LMXBs appear as faint blue stars. The most well known LMXB (in addition to the before-mentioned *Her X-1)* is perhaps *4U1627-673*, which contains a pulsar and the low-mass red dwarf *KZ TrA*. The overwhelming majority of LMXBs however, are not pulsars, and thus probably lack magnetic fields strong enough to affect the accretion flow ($B \lesssim 10^9$ G).

- **HMXB**
  In high-mass X-ray binaries ($M_d \gtrsim 10\,M_\odot$), the donor star is an O or B-star whose optical/UV-luminosity generally exceeds that generated by the X-ray source. X-ray heating is minimal, with optical properties dominated by the donor. The OB-star has a substantial stellar wind, and may in some cases remove as much as $\sim 10^{-6}\,M_\odot\,yr^{-1}$ [18]. A neutron star in a close orbit could capture a significant fraction of this wind, sufficient to power the X-ray source. Prominent HMXBs containing pulsars are *Vela X-1* (wind fed), *Cen X-3* and the Magellanic-cloud sources *SMC X-1* and *LMC X-4* (all probably Roche lobe overflow-systems [19]).

[2] In a LMXB, a stellar wind from the mass donor may be a consequence of the absorption of X-rays from the compact object. A neutron star (or black hole) may capture as much as $\sim 10\%$ of this induced stellar wind (ISW), and the result could be a self-sustained ISW-driven system [17].

It is easy to realize that an optical identification, along with orbital parameters of the system are very useful. They establish the nature (spectral type) of the donor star, the mode of mass transfer and information on the overall accretion flow (geometry and rate).

2.4 The Eddington Limit

We have indicated earlier that the radial accretion (or infall) of material onto a neutron star converts gravitational potential energy into heat and radiation in a very efficient way (in units of the material's available rest-mass energy). If we now assume that the flow is spherical and neglect magnetic fields, the gas will be moving in free-fall radial velocity until it reaches the neutron star surface. The gas will then be decelerated abruptly, and its kinetic energy will be converted into heat and radiation. In the event of accretion onto a black hole this would not necessarily be the case, as the gas would take some part of its energy with it across the Schwarzchild-radius. This so-called Bondi accretion model would be a reasonably good approximation in the event of an isolated star accreting from a large gas cloud (for instance the interstellar medium).

From (1.1) we have the total luminosity L_{acc} from the neutron star surface and the accretion disk

$$L = L_{acc} = L_{disk} + L_{surface} = \frac{GM}{R}\dot{M} \tag{2.9}$$

Continuing our simple model, let us compute the upward force exerted on the infalling matter, taken to be ionized hydrogen, by the radiation flux from the surface. Under these circumstances, the radiation exerts a force mainly on the free electrons through Thompson-scattering. The scattering cross-section for protons is a factor $(m_e/m_p)^2 \approx 2.5 \cdot 10^{-7}$ smaller. The protons are however influenced by the upward force, through their electrostatic coupling to the electrons. Take the mean momentum of the photons to be $\overline{p}$, and since the Thompson-scattering is elastic, this is the mean momentum that will be transferred per collision. Assuming the photons are moving radially, the number of photons crossing unit area in unit time at radius r is $L_r = L/4\pi r^2(\overline{p}c)$. The number of collisions per electron per unit time is then $L_r\sigma_T$, where $\sigma_T = 6.6 \cdot 10^{-29}\,\mathrm{m}^2$ is the Thompson cross-section. The force per electron is then the rate at which momentum is transferred per unit time

$$F_{rad} = \frac{L\sigma_T}{4\pi r^2 \overline{p}c}\,\overline{p} = \frac{L\sigma_T}{4\pi r^2 c} \tag{2.10}$$

We should note that this expression holds even if the photons are not streaming radially,

since only the component p_r of the momentum is transferred radially per collision. The radiation pushes out electron-proton pairs against the total gravitational force $GM(m_e + m_p)/r^2 \simeq GMm_p/r^2$, acting on each pair at a radial distance r from the center. So the net inward force on an electron-proton pair is

$$F_{grav} - F_{rad} = \left(GMm_p - \frac{L\sigma_T}{4\pi c}\right)\frac{1}{r^2} \tag{2.11}$$

There is a limiting luminosity, the *Eddington luminosity*, for which this expression vanishes

$$L_{Edd} = \frac{4\pi GMm_p c}{\sigma_T} \simeq 1.3 \cdot 10^{31}\left(\frac{M}{M_\odot}\right) \mathrm{J\,s^{-1}} \tag{2.12}$$

At greater luminosities the outward pressure of radiation would exceed the inward gravitational attraction, and accretion would be halted unless some form of outside pressure acted on the infalling gas.

For accretion powered objects the Eddington luminosity implies a limit on the steady accretion rate $\dot{M}_{crit}$ (or $\dot{M}_{Edd}$), due to the fact that we must have $L_{acc} \lesssim L_{Edd}$. The critical mass-accretion rate $\dot{M}_{crit}$ associated with the Eddington luminosity is defined from (2.9)

$$\dot{M}_{crit} = \left(\frac{R}{GM}\right) L_{Edd} \tag{2.13}$$

Using (1.2) we get for the efficiency factor $\beta = L/\dot{M}c^2 = L_{Edd}\dot{M}_{crit}c^2 \simeq 0.15$. We then have

$$\dot{M}_{crit} = \frac{L_{Edd}}{\beta c^2} \sim 10^{-8}\, M_\odot\, \mathrm{yr}^{-1} \tag{2.14}$$

Several oversimplifications were made in the above argument, some of them partially justified. For a more complicated and realistic situation (non-spherical flow etc.) we cannot expect (2.12) to be any more than a crude estimate. It is interesting though, to note that no steady galactic X-ray binaries, with known or estimated distances, show luminosities that exceed a few times $10^{31}\,\mathrm{J\,s^{-1}}$. The Eddington luminosity is of great practical importance for the study of X-ray binaries, in particular because certain types of systems can be used as "standard candles", in the sense that their typical luminosities are always close to their Eddington limits.

Chapter 3

The Unperturbed Accretion Disk

In contrast to stars, which have been known from ancient eras, the presence of accretion disks has been recognized only quite recently. In this sense one might say that an accretion disk is a relatively new type of object. Theoretical studies of accretion flows were initiated as late as in the 1960s. The early history of accretion disk modeling includes publications by Prendergast [3], Shakura [20] and Pringle & Rees [21]. But the appearance of a monumental paper by Shakura & Sunyaev [22] established the classical picture of accretion disks. It marked the beginning of attempts to find a detailed self-consistent model, resolving both the hydrodynamics and the radiation properties of such disks. Today this Shakura-Sunyaev model is regarded as the standard model for thin accretion disks.

However, as a large body of observational data has accumulated, gaps between the classical models and some of the observations have become clear. More detailed, accurate and specialized models have been added, and the literature of accretion disks have grown as our confidence in the accretion model has become more settled. In spite of that, many of the major uncertainties of the early models are still with us at this time, and a firm general consensus is lacking.

3.1 Principal Mechanics of the Accretion Disk

The disk that forms under the mass-transfer mechanisms outlined in Chapter 2, has a definite radius R_d. The magnitude of R_d however depends on the mode of mass-transfer and the binary parameters. If we were considering a test-particle it would simply orbit the primary M in an ellipse at $R \sim R_d$. But for the continuous stream of gas captured from the donor-star, the corresponding configuration would be a ring of matter at $R \sim R_d$. Within such a ring there will be dissipative processes, which will convert some of the orbital energy of the bulk of matter into internal heat, which in turn is radiated and therefore

lost to the system. This loss of energy leads the gas to sink deeper into the gravitational potensial of the primary, and thus requires it to lose angular momentum. The timescale on which the orbiting gas can redistribute its angular momentum is normally much longer than both the energy-loss timescale t_{th} (by radiative cooling), and the dynamical timescale t_{dyn} (the approximate time for an orbit). Since a circular orbit has the least energy for a given angular momentum, we will expect most of the gas to spiral inwards towards the primary through a series of approximately circular orbits in the binary orbital plane. This configuration would be recognized as an *accretion disk*.

Outward Flow

In the absence of external torques, this can only occur by transfer of angular momentum outwards through the disk by internal torques. The matter inside the disk both gives away and gains angular momentum to gas at other radii. Most of the matter loses more angular momentum than it gains, and will therefore spiral inwards towards the compact object. Since however totally (for the whole disk) angular momentum is conserved, some matter at the outer rim of the disk will gain more angular momentum than it can give away, and will therefore spiral outwards and out of the disk, where it may or may not be lost to the binary system. This outwards spiraling (or loss) of gas from the outer parts of the disc is necessary to carry away the angular momentum from the main body of the disk. It should be emphasized that the mass of this fraction of the gass is actually small compared to the mass that actually accretes onto the compact object. We shall however not dwell into details concerning the disposal of this angular momentum in the total binary system, we only observe that the outer edge of the disk will in general be at a radius exceeding R_d (where R_d might be referred to as the minimum disk-radius).

3.1.1 Viscous Torques

The case of Keplerian rotation in the disk implies for the angular velocity

$$\Omega_K(r) = \left(\frac{GM}{r^3}\right)^{1/2} \tag{3.1}$$

This Keplerian rotation law implies differential rotation in the disk, i.e. material at neighboring radii will move with different Ω (and different v_ϕ). Fluid elements in neighboring streams will slide past each other, and due to random and turbulent motions of these fluid elements, matter will drift between different radii. Since the material originating in the two annuli on average will have different specific angular momentum, this will cause a transfer of angular momentum. This type of transport process is known as *shear viscosity*, as the effect must vanish if there is no shearing (or sliding) of adjacent gas streams past

one another. In for example solid body-rotation, the relative distances between any pair of fluid/gas elements remains constant, and thus no shear viscosity is generated.

Flow Assumptions

We assume that the gas flow takes the form of an accretion disk, with cylindrical polar coordinates (r, ϕ, z). We assume azimuthal symmetry, with gas flowing in a Keplerian fashion in the ϕ-direction with angular velocity $\Omega_K(r)$ about the origin. The gas flow lies between $z = \pm H$, where H generally will be a function of r. The basic picture is, as we have seen, one in which chaotic turbulent elements of the gas move at a typical random velocity $\bar{v}$, and travel a mean free path λ before mixing with other materials. This causes a radial mixing, where gas elements 1 and 2 are constantly exchanged across the surface with radius r. Thus the net angular momentum transfer (or net torque) across a radius r will be produced by the angular momenta of two streams of gas (Fig. 3.1). From material originating at $r - \lambda/2$ and moving outward across r to mix with annular material centered at $r + \lambda/2$, and the other starting at $r + \lambda/2$ and moving inward across r into the inner annulus at $r - \lambda/2$ (Fig. 3.1).

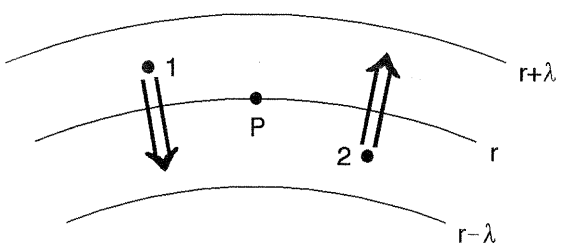

Fig. 3.1 *Radial mixing by drift of particles across radius r, causing angular momentum transfer.*

Because the chaotic motion takes place in an equilibrium flow, this process cannot result in any net transfer of matter between the two annuli. Mass therefore crosses the surface at r at equal rates in both directions, of the order $H\rho\bar{v}$ per unit arc length, where $\rho(r)$ is the mass density. There is however a transport of angular momentum, which effectively leads to a viscous torque exerted on the outer stream by the inner stream. Consider the material originating at $r - \lambda/2$, which is diffusing outwards and has an orbital velocity of

$$\begin{aligned} v\left(r - \frac{\lambda}{2}\right) &= \left(r - \frac{\lambda}{2}\right) \Omega\left(r - \frac{\lambda}{2}\right) \\ &= \left(r - \frac{\lambda}{2}\right) \left(\Omega(r) - \frac{\lambda}{2}\frac{d\Omega}{dr}\right) \end{aligned} \tag{3.2}$$

where we have approximated the angular velocity to first order in a Taylor-series. A similar expression can be found for the matter originating at $r + \lambda/2$:

$$v\left(r+\frac{\lambda}{2}\right) = \left(r+\frac{\lambda}{2}\right)\left(\Omega(r) + \frac{\lambda}{2}\frac{d\Omega}{dr}\right) \tag{3.3}$$

We introduce the *surface density* (mass density per unit area) as

$$\Sigma(r) = \int_{-H}^{H} \rho\, dz = 2\int_{0}^{H} \rho\, dz = \int_{-\infty}^{\infty} \rho\, dz \tag{3.4}$$

This means that the net outward transfer of angular momentum across r per unit length according to a corotating observer at P is

$$\Sigma\bar{v}\left[\left(r-\frac{\lambda}{2}\right)^2\left(\frac{-\lambda}{2}\right)\frac{d\Omega}{dr} - \left(r+\frac{\lambda}{2}\right)^2\left(\frac{\lambda}{2}\right)\frac{d\Omega}{dr}\right] = -\Sigma\bar{v}\lambda r^2\frac{d\Omega}{dr} \tag{3.5}$$

where we have assumed that λ is small compared to the scale over which Ω varies significantly. The transport *coefficient for kinematic viscosity* ν is often defined as

$$\nu = \lambda\bar{v} \tag{3.6}$$

The torque exerted by the inner ring on the outer ring gives the net outward angular momentum flux. The total torque of the outer annulus on the inner (= −total torque of the inner on the outer) at r is then

$$G(r) = 2\pi r\Sigma\nu r^2\frac{d\Omega}{dr} = 2\pi r^3\Sigma\nu\frac{d\Omega}{dr} \tag{3.7}$$

Note that a negative gradient of angular velocity leads this torque to be negative (opposite the angular velocity of the flow of gas in the inner annulus), so the faster moving inner annulus will decelerated, while the slower moving outer annulus will be accelerated. Or in other words: a positive outward flux of angular momentum. The same result may also be deduced in another alternative, and perhaps more formal way by use of the Navier-Stokes equation $\rho(\partial\mathbf{v}/\partial t + (\mathbf{v}\cdot\nabla)\mathbf{v}) + \nabla\tilde{\mathbf{t}} = 0$ for a viscous fluid, where the viscous stress tensor $\tilde{\mathbf{t}}$ is used. The dominant component of $\tilde{\mathbf{t}}$ that contributes in our Keplerian accretion disk model is[1]

$$t_{r\phi} = \rho\nu r\frac{d\Omega}{dr} \tag{3.8}$$

[1]The viscous stress tensor in the Navier-Stokes equation above is $t_{ij} = t_{ji} = \rho\nu\left(v_{i,j} + v_{j,i} - \frac{2}{3}\delta_{ij}v_{k,k}\right)$. In cylindrical coordinates the dominant component of $\tilde{\mathbf{t}}$ is $t_{r\phi} = t_{\phi r} = \rho\nu\left(\frac{1}{r}v_{r,\phi} + v_{\phi,r} - \frac{v_\phi}{r}\right)$ [23].

which then becomes the viscous stress (or viscous force per unit area) in the ϕ-direction at r.

Now we will use the result $G(r)$, to consider the *net* torque on a ring of gas between r and $r - \Delta r$. For practical reasons we choose r as the outer limit because (3.7) refers to an outward angular momentum transport. As this has both an inner and an outer edge it is subject to competing torques. The middle annulus is subject to the negative torque $G(r)$ from the outer, and the positive torque $-G(r - \Delta r)$ from the inner annulus (Fig. 3.2). We see that the rate of angular momentum loss of the annulus through the outer surface at r is $|G(r)|$ (it gains $G(r) < 0$) and the rate of angular momentum gain at $r - \Delta r$ is $|G(r - \Delta r|$ (it gains $-G(r - \Delta r > 0$). Then (from definition of the derivative) we get the net rate of angular momentum gain

$$G(r - \Delta r) - G(r) = \frac{\partial G}{\partial r} \Delta r \tag{3.9}$$

The net torque received by the gas in the annulus at r with unit length in the radial direction is thus dG/dr.

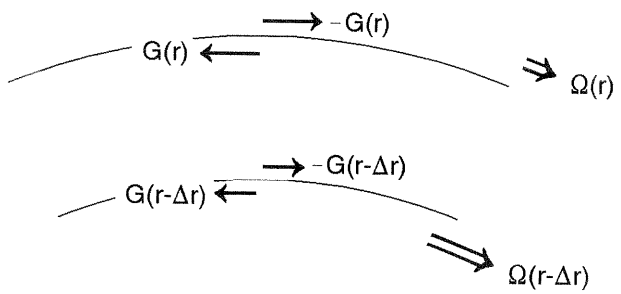

Fig. 3.2 *Competing torques from larger and smaller radii on annulus ar r.*
It is clear that for our accretion disk mechanism to work, we need $|G(r - \Delta r)| < |G(r)|$.

The total torque on the middle annulus $(\partial G/\partial r)\,\Delta r$ does an amount of work per unit time (a rate of working)

$$\frac{d}{dt}\left[\left(\frac{\partial G}{\partial r}\Delta r\right)\phi\right] = \Omega\frac{\partial G}{\partial r}\Delta r = \left[\frac{\partial}{\partial r}(G\Omega) - G\frac{d\Omega}{dr}\right]\Delta r \tag{3.10}$$

We can here observe that the term

$$\frac{\partial}{\partial r}(G\Omega)\,\Delta r \tag{3.11}$$

is the rate at which rotational energy is transferred throughout the disk, a convection of rotational energy if you want. While

$$-G\left(\frac{d\Omega}{dr}\right)\Delta r \tag{3.12}$$

is the loss of mechanical energy of the gas. This lost energy will be converted into internal energy (heat). The disk can deposit this energy in a number of ways, but most of it will be radiated away from the upper and lower surfaces of the disk. In so-called advection-dominated diskflows, the heat can be carried with the gas and eventually lost at other radii, but in most standard models the generated heat is radiated immediately. The disk has in any case two plane faces, and thus a plane area $4\pi r\,\Delta r$, and with a dissipation within the gas at a rate of $G(d\Omega/dr)\Delta r$ per ringwidth Δr, we get the dissipation rate per unit plane surface area as[2]

$$D(r) = \frac{G}{4\pi r}\frac{d\Omega}{dr} = \frac{1}{2}\nu\Sigma r^2\left(\frac{d\Omega}{dr}\right)^2 \tag{3.13}$$

We have now seen that the introduction of a viscosity in the disk has two major functions.

- It leads to the necessary outward angular momentum transfer, so that the gas slowly spirals towards the primary (compact) object (3.11).
- This type of shear viscosity also inevitably leads to heating of the gas, which makes the gas radiate and therefore to be readily observable (3.12).

3.1.2 Mass and Angular Momentum Conservation

The fact that the gas flow is limited to move between $z = \pm H$ leads us to the definition of geometrically thin disks

$$H \ll r \tag{3.14}$$

This is called the *thin disk condition*, and as we shall see it is in some way related to our assumption of Keplerian rotation. Generally for disks in which $T \sim 10^4\,\mathrm{K}$. we have $H/r \sim 0.01$, but as T increases the thin disk condition generally becomes less valid, and may eventually break down. In such cases the accretion disk may expand and become bloated, and this happens in the central region of many disk models.

As long as the thin disk condition is valid we can then decouple the equations in the z and r direction into a set of two, separate, one-dimensional descriptions. The first one

[2]Expression (3.13) may also be derived from the energy equation of the Navier-Stokes description for a viscous fluid. The $D(r)$ is then identified as the dominant term of the viscous dissipation function Φ.

describing the radial structure and the other describing the vertical structure of the disk. Also, it is reasonable to use a one-zone approximation for the vertical structure of the disk. In this one-zone approximation we put

$$\Sigma = \Sigma(r) = \int_{-\infty}^{\infty} \rho(r)\, dz = 2\rho(r)H \tag{3.15}$$

And we may also take the vertically integrated viscous stress at r (force per unit area) to be

$$T_{r\phi} = \int_{-\infty}^{\infty} t_{r\phi}\, dz = \nu\Sigma r\frac{d\Omega}{dr} \tag{3.16}$$

where (3.8) is used. We now exploit our knowledge of the principal mechanics of the accretion disk to deduce conservation equations for mass and angular momentum transport in the disk due to radial drift motions. We take an annulus of the disk material lying between r and $r - \Delta r$. This ring has a total mass $2\pi r\Delta r\Sigma$ and total angular momentum $2\pi r\Delta r\Sigma r^2\Omega$. The rate of change of both these quantities is given by the net flow from the neighbouring annuli. Conservation of mass in this annulus gives

$$\begin{aligned}\frac{\partial}{\partial t}(2\pi r\Delta r\Sigma) &= (v_r \cdot 2\pi r\Sigma)_{r-\Delta r} - (v_r \cdot 2\pi r\Sigma)_r \\ &\simeq -2\pi\Delta r\frac{\partial}{\partial r}(r\Sigma v_r)\end{aligned} \tag{3.17}$$

where it should be noted that $v_r < 0$ for inflow. We make the $\Delta r \to 0$, and get the mass continuity equation

$$r\frac{\partial\Sigma}{\partial t} + \frac{\partial}{\partial r}(r\Sigma v_r) = 0 \tag{3.18}$$

The conservation equation for angular momentum transfer in this annulus is similar, except that we must include the transport due to the net effects of the viscous torques $G(r)$

$$\begin{aligned}\frac{\partial}{\partial t}(2\pi r\Delta r\Sigma r^2\Omega) &= (v_r \cdot 2\pi r\Delta r\Sigma r^2\Omega)_{|r-\Delta r} - (v_r \cdot 2\pi r\Delta r\Sigma r^2\Omega)_{|r} + \frac{\partial G}{\partial r}\Delta r \\ &\simeq -2\pi\Delta r\frac{\partial}{\partial r}(r\Sigma v_r r^2\Omega) + \frac{\partial G}{\partial r}\Delta r\end{aligned} \tag{3.19}$$

Again in the limit $\Delta r \to 0$ we get

$$r\frac{\partial}{\partial t}(\Sigma r^2\Omega) + \frac{\partial}{\partial r}(r\Sigma v_r r^2\Omega) = \frac{1}{2\pi}\frac{\partial G}{\partial r} \tag{3.20}$$

By combining the two conservation equations and assuming $\partial\Omega/\partial t = 0$ (which will hold in a fixed gravitational potential) we get

$$r\Sigma v_r \frac{\partial(r^2\Omega)}{\partial r} = \frac{1}{2\pi}\frac{\partial G}{\partial r} \tag{3.21}$$

We would like to eliminate v_r in our equations by using (3.18) and (3.21), and this brings us to

$$r\frac{\partial \Sigma}{\partial t} = -\frac{1}{2\pi}\frac{\partial}{\partial r}\left[\frac{\partial G}{\partial r}\left\{\frac{\partial(r^2\Omega)}{\partial r}\right\}^{-1}\right] \tag{3.22}$$

If we substitute (3.7) for $G(r)$ and use the assumption of Keplerian orbits we get finally

$$\frac{\partial \Sigma}{\partial t} = \frac{3}{r}\frac{\partial}{\partial r}\left[r^{1/2}\frac{\partial}{\partial r}\left(\nu\Sigma r^{1/2}\right)\right] \tag{3.23}$$

This is the basic equation (together with a prescription for ν) governing the time evolution of surface density in a Keplerian disk. In general it is a non-linear diffusion equation for Σ, because ν may be a function of local variables in the disk.

If we assume that $\Sigma(r,t)$ is a solution of (3.23), we get v_r as

$$v_r = -\frac{3}{\Sigma r^{1/2}}\frac{\partial}{\partial r}\left(\nu\Sigma r^{1/2}\right) \tag{3.24}$$

Now that we have equation (3.23) we can illustrate the mechanics of the viscous accretion disk in a very nice way. For some special cases it is possible to solve (3.23) analytically. Generally if the viscosity is a power-law function of r, then (3.23) can in most cases be solved [24]. If we consider the case $\nu \sim r$ for example, and we also assume as boundary conditions an initial ring of matter of infinite consentration at $r = r_{in} \rightarrow \Sigma(r,0) \sim \delta(r - r_{in})$, we get an analytical solution[3]

$$\Sigma(x,\tau) = \frac{\Sigma_0}{2x^2\sqrt{\pi\tau}}\left[e^{\frac{(x-1)^2}{4\tau}} - e^{\frac{(x+1)^2}{4\tau}}\right] \tag{3.25}$$

where we have $x = \sqrt{r/r_{in}}$ and $\tau = t/t_0$. The parameters t_0 and Σ_0 are numerical constants, where t_0 corresponds to the viscous timescale $t_{visc} = r/v_r$ at r_{in}, that is $t_0 = t_{visc}(r_{in}) = r_{in}/v_r(r_{in})$. Fig. 3.3 shows the matter distribution in this system at six different values of τ (or t), and nicely demonstrates how the mass accretion process proceeds in a viscous disk. We can see that the outer part of the matter distribution moves outwards, taking away the angular momentum of the inner parts, which move inwards towards the accreting compact object. If we insert $\Sigma(x,\tau)$ into (3.24) we see that the radius at which v_r changes sign, moves outwards itself. Thus parts of the matter distribution which are at radii $r > r_{in}$ just after the initial release of the ring ($t \sim 0$), at first move to larger radii,

[3]See Appendix B for a general discussion.

but later begin themselves to lose angular momentum to parts of the disk at still larger radii and thus drift inwards. A very long time after the initial release ($\tau = 1.024$) we can see that the density profile begins to resemble one which we perhaps could expect in a steady version of such an accretion disk. Since we have no sink in which the matter can disappear in this model (a Schwarzschild radius or a neutron star surface), the matter will build up at $r = 0$, and we can see that this is beginning to happen already at $\tau = 0.032$. If there is a sink, then after a long time almost all of the original mass will have accreted on to the compact object ($r \sim 0$), and all of the original momentum have been carried to very large radii (back into the circumbinary envelope) by a very small fraction of the mass.

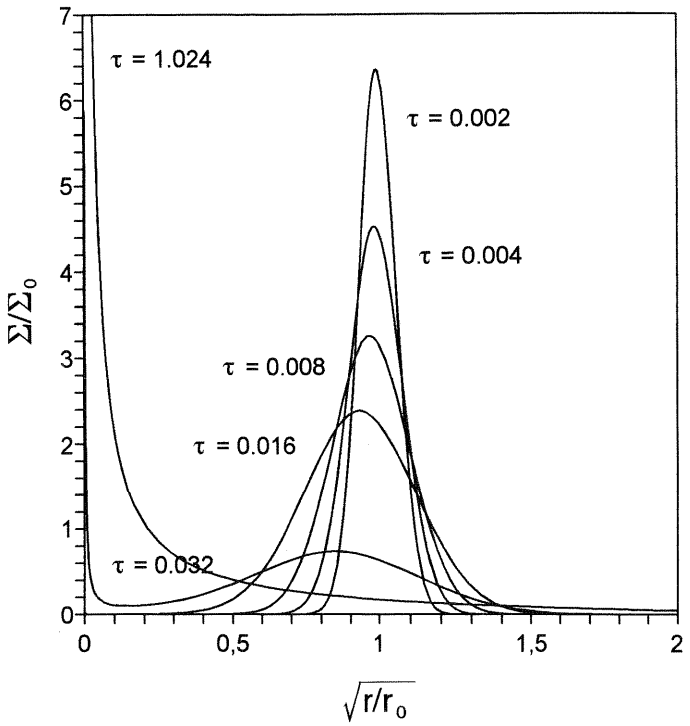

Fig. 3.3 *A ring of matter placed in orbit at $r = r_{in}$, spreads out under the action of viscous forces. The surface density Σ/Σ_0 is shown as a function of $x = \sqrt{r/r_{in}}$ and $\tau = t/t_0$*

There are several timescales that must be considered when looking at these disk models. It is now clear from the above that the disk mass gradually drifts inward with a radial velocity $v_r\,(< 0)$, while at the same time rotating around the compact object with Keplerian velocity v_ϕ. The assumption here is one of rapid rotation with slow inflow, that is

$$|v_r| \ll v_\phi \;\Rightarrow\; t_{visc} \equiv \left|\frac{r}{v_r}\right| \gg t_{dyn} \equiv \frac{r}{v_\phi} = \frac{1}{\Omega_K} \tag{3.26}$$

We will later look at other timescales, such as the hydrostatic timescale t_{hyd} over which

the vertical disk structure may distribute changes, and the thermal timescale t_{th} over which energy is transported inside, and out of the disk.

3.2 The α-disk Formulation

The nature of this prominent viscosity is one of the enigmas of accretion disk physics. We may try to establish the viscous timescale, over which transfer of angular momentum takes place, by observing that the rate of angular momentum gain in an annulus at r is $\sim G(r)/r \sim 4\pi r\Sigma\nu\Omega$, while the angular momentum contained in this annulus is $\sim 2\pi r\Sigma r^2\Omega$. The viscous timescale is then

$$t_{visc} \sim \frac{r^3\Sigma\Omega}{r\Sigma\nu\Omega} = \frac{r^2}{\nu} = \frac{r^2}{\lambda\bar{v}} \tag{3.27}$$

where r then denotes the typical dimension of the disk. For standard non-turbulent plasmas we have the proton-proton collision mean free path $\lambda = 10^9\,(T^2/N)\,\mathrm{m}$ [14], and we equate the mean velocity $\bar{v}$ with the sound speed in such a plasma, $\bar{v} = c_s \simeq 10^3\sqrt{T/10^4\,\mathrm{K}}\,\mathrm{m\,s^{-1}}$ [25]. With $T \sim 10^4\,\mathrm{K}$, $\rho \sim 10^{-5}\,\mathrm{kg\,m^{-3}} \Rightarrow N \sim 10^{22}\,\mathrm{m^{-3}}$ as parameter estimates that hold for the outer regions of most accretion disks in binaries (as we shall confirm later with the Shakura-Sunyaev model), this gives $\nu \sim 10^{-2}\,\mathrm{m^2\,s^{-1}}$. With $r \sim 10^8\,\mathrm{m}$ as the accretion disk radius (about the size of the Earth-Moon distance) we have

$$t_{visc} \sim 10^{18}\,\mathrm{s} \sim 10^{11}\,\mathrm{yr} \tag{3.28}$$

which is $\gtrsim$ Hubble-time t_H. It is therefore quite clear that the regular non-turbulent collision viscosity is not by far sufficient to generate the dissipation and angular momentum transfer that we require for such an accretion disk to operate. We need some other type of anomalous viscosity based on turbulence and/or magnetic fields. If we try to estimate the viscosity coefficient ν based on turbulence we take $\bar{v} \sim c_s \sim 10^3\,\mathrm{m\,s^{-1}}$ and $\lambda \sim H \sim 10^5\,\mathrm{m}$. We then get $\nu \sim 10^8\,\mathrm{m^2\,s^{-1}}$, and thus

$$t_{visc} \sim 10^8\,\mathrm{s} \tag{3.29}$$

A reasonably short angular momentum viscous timescale estimate (although maybe one or two orders of magnitude too high).

If we define the *Reynolds number* for such a system as follows [14]

$$Re = \frac{\text{Inertial}}{\text{Viscous}} \sim \frac{rv_\phi}{\lambda\bar{v}} \tag{3.30}$$

then this measures the importance of viscosity. We see that if $Re \ll 1$ then viscous forces dominate the flow, and if $Re \gg 1$ then viscosity associated with dynamics at the scale of the given λ and $\bar{v}$ is dynamically unimportant. We also have $rv_\phi = \sqrt{GMr}$. If we use the same estimates for T and r, and the number density is $N \sim 10^{21}\,\mathrm{m}^{-3}$ we get

$$Re > 10^{14} \tag{3.31}$$

The clue to the right kind of viscosity is provided by this estimate. It is known that if the Reynolds number in a fluid is gradually increased, there is a critical Reynolds number at which turbulence sets in. At this point the fluid velocity suddenly begins to exhibit large and chaotic variations on an arbitrarily short time and length scale.

The α-parameter

Turbulence, especially in the extreme conditions that an accretion disk provides, is one of the relatively uncharted areas in physics. Our present understanding of the onset of turbulence is limited, it is therefore difficult to determine the parameters λ_t and $\bar{v}_t$ with any degree of certainty. We can however try to place plausible limits on them. We can say that the largest turbulent movements (eddies) cannot exceed the disk thickness H, so $\lambda_t \lesssim H$. $\bar{v}_t$ is the velocity of turbulent cells relative to the mean gas motion. It is expected that shocks will dissipate turbulent kinetic energy into heat whenever the motion is supersonic [22], so we conclude that $\bar{v}_t \lesssim c_s$. Based on all this, we now introduce the α-prescription of Shakura-Sunyaev:

$$\nu = \alpha c_s H \tag{3.32}$$

where α is a nondimensional viscosity parameter, for which we expect

$$0 \lesssim \alpha \lesssim 1 \tag{3.33}$$

Models constructed using this prescription are called α-disks. Such models typically leave α as a free, constant parameter in the disk structure equations. It is important to realize that this α is only a measure of the viscosity, not the physics behind it. There is no cogent reason to believe α to be constant throughout the disk-structure. Even $\alpha \lesssim 1$ might be violated in regions where some physical phenomena feeds the supersonic turbulence (in contrast to our assumption that $\bar{v}_t \lesssim c_s$). It is however quite possible to some degree to calibrate α empirically from observations. So-called Cataclysmic Variables (CV), are X-Ray binary systems in which the compact component is a white dwarf. Comparisons between observations on such systems and α-disk models, puts α in the range $0.1 - 1$ [26]. Various models have, more or less successfully, been attempted to derive a physical

mechanism for the accretion disk viscosity ν from first principles, and most of these result basically in the same constraints on α as above, that is to say they reproduce the α-disk.

The source of viscosity is likely, as I have mentioned, to be small scale turbulence in the gas-dynamical flow. It is a generally accepted notion that all viscous accretion disks inhibit at least a weak *internal* magnetic field, and that this field is necessary for the generation and maintenance of this turbulence. This is the case for the mechanism suggested by J. F. Hawley and Steven A. Balbus [27], which has generated some interest in recent years. This is a mechanism where magnetohydrodynamic turbulence is driven by a magnetorotational instability (MRI). On the basis of this idea, some attempts to answer fundamental questions about accretion dynamics have been made [46][47].

3.3 Steady Thin Disks

I have mentioned that changes in radial structure in a thin disk occur on timescales $t_{visc} \sim r/v_r$. In accretion disk systems many different external conditions may change on timescales rather longer than t_{visc}. In these cases the disk will settle into a steady-state (or semi steady-state) structure. Within this steady-state, there may be temporal changes in the disk structure and evolution caused by violent or rapid phenomena (on a timescale shorter than t_{visc}), but for many of these cases the disk will return to a steady-state on the same timescale. The most prominent external change is variance in the mass flow rate $\dot{M}$, if this decreases sufficiently it can in fact turn off the disk all together.

3.3.1 Azimuthal Motion

We can examine this by setting $\partial/\partial t = 0$ in the conservation equations (3.18) and (3.20). From the first (mass conservation) we get that $r\Sigma v_r$ is a constant. This represents (as an integral of the mass conservation equation) the constant inflow of mass through each point in the disk. Since $v_r < 0$ we write

$$\dot{M} = -2\pi r \Sigma v_r \tag{3.34}$$

where $\dot{M}$ is the accretion rate. From the angular momentum conservation (3.20) we get (with $\partial/\partial t = 0$)

$$r\Sigma v_r r^2 \Omega = \frac{G}{2\pi} + \frac{C}{2\pi} \tag{3.35}$$

where C is a constant. If we use (3.7) for $G(r)$ we get

$$-\nu\Sigma\frac{d\Omega}{dr} = -\Sigma v_r \Omega + \frac{C}{2\pi r^3} \tag{3.36}$$

The constant C is related to the rate at which angular momentum flows into the compact object. Let us suppose that the disk extends down to the surface $r = R$ of the compact object. For material to accrete, the star must be rotating below break-up speed at its equator, that is we must have

$$\Omega_R < \Omega_K(R) \tag{3.37}$$

In this case the angular velocity of the disk material remains Keplerian and thus increases inwards, until it begins to decrease to the value Ω_R. This turnover takes place in a "boundary layer" of radial extent $\delta \ll R$. Hence there is a radius $r = R + \delta$ at which $\partial\Omega/\partial r = 0$, and we have (since $\delta \ll R$) that Ω is very close to its Keplerian value at the point where the turnover takes place:

$$\Omega(R+\delta) = \left(\frac{GM}{R^3}\right)^{1/2} [1 + \mathcal{O}(\delta/R)] \tag{3.38}$$

If δ is instead comparable to R, then the thin disk approximations all break down at $r = R+\delta$. It is then not any longer a boundary layer, but rather some kind of thick disk. This would happen if the compact object has sufficiently strong magnetic fields, so that it can control the flow of the disk material out to radii r such that $v_\phi = r\Omega_R > v_K = r\Omega_K(R)$. We leave however these considerations for later, and observe that at $r = R + \delta$ equation (3.36) becomes

$$C = 2\pi R^3 \Sigma v_r \Omega(R+\delta)_{|R+\delta} \tag{3.39}$$

If we insert (3.38) and $\dot{M} = -2\pi r \Sigma v_r$ into this, we get the constant C as

$$C = -\dot{M}(GMR)^{1/2} \tag{3.40}$$

to terms of the order δ/R. If we use this value for C in (3.36) and use the expression for $\Omega = \Omega_K$ we have for Keplerian thin disks

$$\nu\Sigma = \frac{\dot{M}}{3\pi}\left[1 - \left(\frac{R}{r}\right)^{1/2}\right] \tag{3.41}$$

This expression for $\nu\Sigma$ for a steady-state disk can be used further in combination with (3.13), to give (when we put $\Omega = \Omega_K$) for the viscous dissipation (viscous energy production) per unit disk area for each side of the disk

$$D(r) = \frac{3GM\dot{M}}{8\pi r^3}\left[1 - \left(\frac{R}{r}\right)^{1/2}\right] \tag{3.42}$$

Since all this energy from viscous dissipation is assumed to be lost through the surface, the energy flux through the faces of a steady thin disk is independent of viscosity. $D(r)$ is a quantity of prime observational significance, and (3.42) shows its dependence on $\dot{M}, R$ and other variables. The independence of $D(r)$ on ν has come about because we were able to use conservation laws to eliminate ν. Clearly the other disk properties such as Σ, v_r and others, do depend on ν. We can use (3.42) to find the luminosity produced by the disk between radii r_1 and r_2

$$L(r_1, r_2) = 2\int_{r_1}^{r_2} D(r)\, 2\pi r\, dr = \frac{3GM\dot{M}}{2}\int_{r_1}^{r_2}\left[1-\left(\frac{R}{r}\right)^{1/2}\right]\frac{dr}{r^2} \tag{3.43}$$

This can easily be evaluated in the limit $r_1 = R$ and $r_2 \to \infty$ and we get

$$L_{disk} = \frac{GM\dot{M}}{2R} = \frac{L_{acc}}{2} \tag{3.44}$$

which shows that matter at $r = R$ still retains half of the potential energy it has lost in spiraling inwards as as kinetic energy. This half of L_{acc} is therefore available to be radiated from the boundary layer itself, which is therefore just as important as the disk for the total emission.

3.3.2 Hydrostatic Vertical Balance

We now consider the structure of the disk in the vertical z-direction. Since there is no net motion of the gas in the vertical direction, momentum conservation reduces to a hydrostatic equilibrium condition. Here, and in the following, we neglect the self-gravity of the disk, so that equating the component of the gravitational force of the compact star along the z-direction to the vertical pressure gradient gives

$$\frac{1}{\rho}\frac{\partial p}{\partial z} = \frac{\partial}{\partial z}\left[\frac{GM}{(r^2+z^2)^{1/2}}\right] \tag{3.45}$$

In the limit $z \ll r$ this becomes

$$\frac{1}{\rho}\frac{\partial p}{\partial z} = -\frac{GMz}{r^3} \tag{3.46}$$

We now replace the differentials with finite differences. If H is the typical scale height of the disk, then under the one-zone approximation we put $\partial p/\partial z \sim p/H$ and $z \sim H$. Here $p = p\,(z = 0)$. We will now need

$$p/\rho = {c_s}^2 \tag{3.47}$$

where c_s is (as before) the sound speed in the gas.[4] Using this ideal gas expression [10] with (3.46) we have

$$H \simeq c_s r \left(\frac{r}{GM}\right)^{1/2} = r\left(\frac{c_s}{v_\phi}\right) = \frac{c_s}{\Omega_K} \tag{3.48}$$

A solution of the hydrostatic equation (3.46), whose validity is only limited by the thin disk assumption, is given by $\rho(r,z) = \rho_c(r)\, e^{-z^2/2H^2}$, with H from (3.48) and where $\rho_c(r)$ is the density in the central plane $z = 0$. This function will sink very rapidly to 0 for values of z larger than H (outside the disk) see Fig. 3.4. In accordance with this, and the one-zone approximation, we now define with good degree of accuracy, the disk density $\rho(r)$ to be the central disk density $\rho(r) = \rho_c(r) = \Sigma/2H$. Another possible (and common) solution to this problem is the introduction of a vertically polytropic model, in which $p = K\,\rho^{1+1/n}$ instead of (3.47), which would give a different vertical density profile [29]. Here n would be the polytropic index of the model.

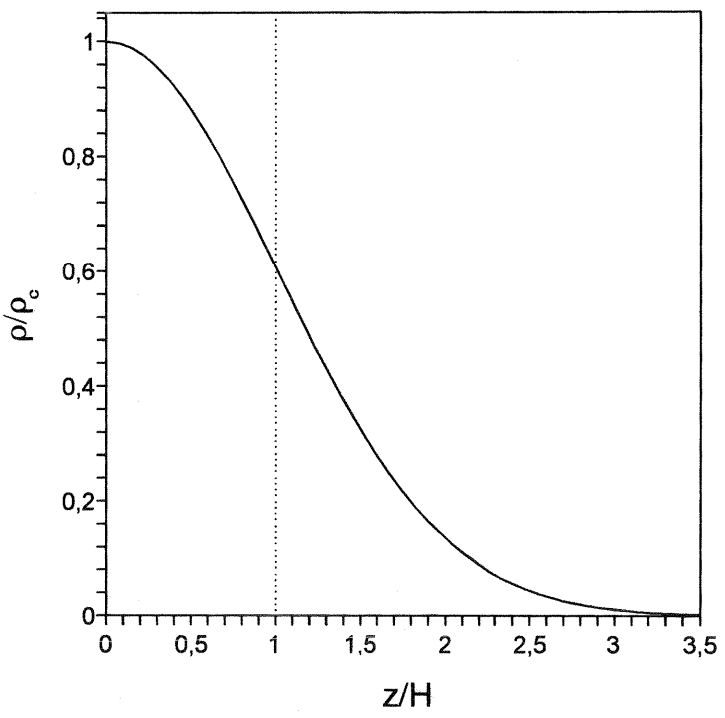

Fig. 3.4 *The density ρ/ρ_c for a fixed r plotted as function of $x = z/H$.*

[4]Formally this is the isothermal sound speed ${v_s}^{iso}$ which we do not distinguish from the adiabatic sound speed ${v_s}^{adi}$ in this model. Since the difference is a mere factor $\sqrt{5/3} \approx 1.29$, this is a very good approximation within our model.

3.3.3 Flow Velocities

The thin disk assumption becomes $H \ll r$ as we have seen earlier, and (3.48) then gives

$$c_s \ll \left(\frac{GM}{r}\right)^{1/2} = r\Omega_K = v_K \tag{3.49}$$

So we see that for a thin disk we require that that the local Kepler velocity should be highly supersonic. This is clearly a condition on the temperature of the disk and thus, ultimately, on the cooling mechanism. It need not hold throughout the disk however, so we must consider cases where the thin disk approximation breaks down. As I have mentioned earlier this tends to occur in the central hot regions of some disks. The radial component of the Navier-Stokes equation $\rho(\partial\mathbf{v}/\partial t + (\mathbf{v}\cdot\nabla)\mathbf{v}) + \nabla\tilde{\mathbf{t}} = 0$ is then

$$v_r\frac{\partial v_r}{\partial r} - \frac{{v_\phi}^2}{r} + \frac{1}{\rho}\frac{\partial p}{\partial r} + \frac{GM}{r^2} = 0 \tag{3.50}$$

We see that the pressure term $(1/\rho)\,(\partial p/\partial r) \sim {c_s}^2/R$, so by (3.49) we can neglect this term by comparison with the gravity term. We can then use $\dot{M} = -2\pi r\Sigma v_r$ and (3.41) to obtain

$$v_R = -\frac{3\nu}{2r}\left[1 - \left(\frac{R}{r}\right)^{1/2}\right]^{-1} \tag{3.51}$$

Adopting the α-parametrization (3.32) we have $v_r \sim \nu/r \sim \alpha c_s H/r \ll c_s$ for all reasonable viscosities (or value ranges of α). We see that v_r is clearly subsonic, and that the term $v_r(\partial v_r/\partial r)$ in (3.50) is even smaller than the pressure gradient term. If we define the *Mach number* as $\mathcal{M} = v_\phi/c_s$ we see that (3.50) implies

$$v_\phi = \left(\frac{GM}{r}\right)^{1/2}\left[1 + \mathcal{O}(\mathcal{M}^{-2})\right] \tag{3.52}$$

and we can also rewrite $H \sim r\mathcal{M}^{-1}$ and $v_r \sim \alpha c_s \mathcal{M}^{-1}$. From this it is clear that within the thin disk assumption the circular velocity v_ϕ is Keplerian and highly supersonic, while the radial drift v_r and vertical scale-height H are consistently small.

3.4 Shakura-Sunyaev Disks

In different accretion disk models the parameters that we have discussed above do not give rise to much enlightening variation, and are considered (with the usual inevitable exceptions) to be the same in most accretion disk models. Even though for example the vertical description of the disk may be made in a more laborious multi-zone approximation,

this increases the numerical accuracy of the model, but does not produce models that differ with any degree of interest to us. The many approaches to the problem of transport and balance of energy in the disk however, produce a plethora of interesting models, and an accompanying number of uncertainties of course. The scheme that I follow belongs largely to Shakura-Sunyaev models, a specific (but important) class of models, that are considered to be the standard models for thin steady accretion disks.

3.4.1 Equation of State

We need a prescription for the pressure $p(r)$. As the temperature is assumed to exceed $T \sim 10^4$ K, the disk plasmas will consist of pure ionized hydrogen. The total disk pressure $p(r)$ is essentially the sum of thermal gas and radiation pressure. For ionized hydrogen this yields

$$p = p_{gas} + p_{rad} = \frac{2k}{m_p}\rho T_c + \frac{4\sigma}{3c}{T_c}^4 \tag{3.53}$$

Here σ is the Stefan-Boltzmann constant. We have assumed that the temperature $T(r,z)$ of the portion of the gas that contributes dominantly to the pressure, is close to the central temperature $T(r,0) = T_c(r)$ in local thermal equilibrium. This does not mean that the temperature is assumed the same throughout the vertical z-structure, as we need a temperature gradient to account for energy transport.

Typically, gas pressure dominates radiation pressure throughout most of the disk, except in an inner region. Usually, depending upon parameters and boundary layers, there will exist a radius (or small region) where the dominant pressure changes from p_{gas} to p_{rad}, and this affects the structure and stability of the disk in a profound way.

3.4.2 Energy Balance- and Transport

As in stars, the vertical energy transport mechanism may be either radiative or convective, depending on whether or not the temperature gradient required for radiative transport is smaller or greater than the gradient given by the adiabatic assumption ($p\rho^\gamma$ is constant). The general assumption (in most standard accretion disk models) is that for typical parameters, the transport mechanism is by radiative transfer. Attempts have been made towards the possibility that energy transport by convection (dominantly turbulent) might be important in accretion disks, and perhaps even dominate, in so-called Convective Dominated Accretion Flow (CDAF). It is possible that convection is much less likely when gas pressure is dominant, this means that convective transfer is everywhere negligible except

perhaps in the inner regions of disks [28]. We shall under any circumstances neglect convective energy transfer in this model.

Energy Balance

As with the pressure $p(r)$ and density $\Sigma(r)$ the temperature and energy transport is also handled by using vertically integrated quantities. The mentioned temperature T_c must be given by an energy equation relating energy flux in the vertical direction to the rate of generation of energy by viscous dissipation $D(r)$. The potensial energy of accreting gas is first converted to thermal energy via viscous processes, and is then released out of the disk as radiation. So the energy balance demand becomes at each radius

$$Q^+_{visc} = Q^-_{rad} \tag{3.54}$$

where heating is due to the viscosity and is given by (3.42), and cooling is via the spatial diffusion of the blackbody radiation. For this to be efficient the thermal timescale t_{th} must be much shorter than the matter diffusion timescale $t_{th} \ll t_{visc}$. This means that there is no significant advective transport of thermal energy radially in the disk. In so-called ADAFs (Advection Dominated Accretion Flows), which many modern accretion disk models include, this condition is relaxed. This ADAF approach is generally mostly applicable or relevant to black hole accretion problems and/or systems in which the mass accretion rate $\dot{M}$ is almost Eddington. In these cases the inner disk in ADAF-models naturally becomes much hotter, and the outer (or middle) regions somewhat cooler, for a given $\dot{M}$.

Radiative Flux

Because of the thin disk assumption, the disk medium is essentially plane-parallel at each radius, so that the temperature gradient is dominantly in the z-direction. The other components of $\boldsymbol{\nabla F}$ are much smaller in a thin disk, because vertical derivatives of most quantities are much larger than horizontal derivatives, or

$$\frac{F_r}{F_z} \sim \frac{H}{r} \qquad \frac{\frac{1}{r}\frac{\partial}{\partial r}(rF_r)}{\frac{\partial F_z}{\partial z}} \sim \left(\frac{H}{r}\right)^2 \tag{3.55}$$

By using (A.15) we get the flux of radiant energy through a surface z = constant as

$$F(z) = -\frac{16\sigma T^3}{3\bar{\kappa}\rho}\frac{\partial T}{\partial z} \tag{3.56}$$

where $\bar{\kappa}$ is the Rosseland mean opacity (as I have defined it in Appendix A). In the way we use this theory, it is implicit in (3.56) that the disk is optically thick, or that the optical depth

$$\tau = \rho H \bar{\kappa}(\rho, T_c) = \frac{\Sigma \bar{\kappa}}{2} \gg 1 \tag{3.57}$$

so that the radiation field is close to the blackbody value. This optically thick assumption applies well to most accretion disks, excluding the inner parts of the hottest disks. Once this $\tau \lesssim 1$, the expression (3.56) breaks down as the gas is optically thin, and the radiation can escape freely. In this case the expression (3.56) must be replaced by

$$F(r) = H\Lambda(\rho, T) \tag{3.58}$$

where $\Lambda(\rho, T)$ is the average photon emissivity in the disk. Typically $\Lambda(\rho, T)$ is due to thermal bremsstrahlung (radiation produced when thermal electrons scatter off the ions in the disk plasma), and Comptonization.

For thermal equilibrium, the divergence of the total flux is equal to the rate of viscous dissipation *per unit volume* $\tilde{Q}^+_{visc}$, so we can write the energy balance as

$$\frac{\partial F}{\partial z} = \tilde{Q}^+_{visc} \tag{3.59}$$

If we integrate, we get

$$F(H) - F(0) = \int_0^H \tilde{Q}^+_{visc}\, dz = D(r) \tag{3.60}$$

From symmetry we realize that $F(0) = 0$, and this leads to $F(H) = D(r)$, which could be anticipated since the optical depth $\tau \gg 1$. Here we understand that $F(H)$ should be $F(H, r)$. The surface then radiates as a blackbody surface and

$$F(H) = D(r) = \sigma T_s^4 \tag{3.61}$$

where T_s characterizes matter at the surface where the blackbody spectrum is generated. This surface need not necessarily be the outer disk surface, but may be some distance below, but comparable to it ($T_s \gtrsim T(H)$). To get a usable energy balance equation we now need to express the cooling Q^-_{rad} in terms of the temperature T (in our model T_c). We take (3.56) and get by integration

$$\int_0^H \bar{\kappa}\rho F(z)\, dz = -\int_{T_c}^{T_H} \frac{16\sigma T^3}{3}\, dT \tag{3.62}$$

Now we approximate

$$\int_0^H \bar{\kappa}\rho F(z)\, dz \simeq \bar{\kappa}_c \rho_c H \left[\frac{F(H) - F(0)}{2}\right] = \frac{\tau F(H)}{2} \tag{3.63}$$

and

$$-\int_{T_c}^{T_H} \frac{16\sigma T^3}{3}\, dT = \frac{4\sigma}{3}(T_c^4 - T_s^4) \simeq \frac{4\sigma}{3}T_c^4 \tag{3.64}$$

The validity of these approximations depends of course on the steepness of the temperature and radiation flux gradients. If we assume a linear "one-zone" connection $\partial T/\partial z = -T/H$ in (3.56) we get $T(z) = T_c \cdot e^{-z/H}$, which would give $T_c = e\,T_s \Rightarrow T_c^4 \simeq 100 \cdot T_s^4$. Though this is probably a conservative estimate, other similar models [22] give the same order of magnitude. The approximation for $F(z)$ assumes a radiation flux gradient profile that is not to steep.

Putting these things together we get the energy balance equation $Q^+_{visc} = Q^-_{rad}$ as

$$F(H) = \frac{8\sigma}{3\tau}T_c^4 = D(r) \tag{3.65}$$

3.4.3 Opacity

There are in general several different regimes of radiative transport that may apply in different regions of the disk at different times, depending upon the accretion rate and other parameters that cause changes in the disk. For the thermodynamic parameters that govern the Shakura-Sunyaev model we assume that two different types of opacity will contribute, and which will be dominant in different regions of the disk. I refer to Appendix A again for a little bit more information. Our two (rivaling) opacity sources are:

- **Absorption by free electrons**
  In the presence of a proton, a photon may be absorbed by a free electron. This is so-called (non-relativistic) inverse bremsstrahlung, and gives rise to an opacity

$$\kappa_{ff} = \kappa_0 \rho T^{-7/2} \tag{3.66}$$

  where $\kappa_0 = 7.5 \cdot 10^{19}\,\mathrm{m^5\,kg^{-2}\,K^{7/2}}$.

- **Scattering by free electrons**
  Thompson scattering of photons on free electrons

$$\kappa_{es} = 0.038\,\mathrm{m^2\,kg^{-1}} \tag{3.67}$$

  and so is constant throughout the disk.

In the outer regions of the disk κ_{ff} will dominate the constant κ_{es}. Since κ_{ff} depends on ρ and T, it is clear that it will change (we assume that it will decrease monotonically) as we approach the compact object. There will then be some sort of radius or region, where the dominant term changes to κ_{es}.

3.4.4 Assumptions

We can now summarize and gather the assumptions that have been made in the construction of steady thin Shakura-Sunyaev disks. Some of these assumptions are general, and applicable to more general classes of disks. Some are however quite specific to Shakura-Sunyaev disks, and/or thin disks.

- The gravitational field is determined by the central compact object, and the *self-gravity of the disk is ignored.* We shall see later that the total mass of the disk is at all times minimal compared to that of the central compact object.

- The disk is *axisymmetric* (symmetric to the polar coordinate ϕ). This is a very general assumption, though there are suggested mechanisms that might perhaps lead to non-axisymmetric disk configurations. These ideas often include some source that influences the disk in a non-symmetric manner, usually involving some perturbation related to the donor star (radiation, tidal forces or others).

- We have constructed a *steady* disk. I have commented on this earlier, in section 3.3.

- The disk is *geometrically thin* in the sense that $H \ll r$. This defines a certain class of disks, as opposed to so-called slim or thick disks, which I shall briefly discuss later. As long as $H \ll r$ we have seen that the vertical and radial structure may be separated, that the vertical structure calculations can be made easier, and that the disk is always dominantly Keplerian ($|v_r| \ll v_\phi$).

- We have assumed that all energy transfer inside the disk structure is *radiative transfer in the vertical direction.* Convective and advective possibilities also exists.

- The disk is *optically thick* in the vertical direction, and we have chosen opacity sources κ_{ff} and κ_{es}. There are other choices for opacity, which make alternative schemes possible.

- In the *equation of state* we assume that gas pressure and radiation pressure are the only contributions. There are models which in addition use a magnetic pressure term generated by the disk's own dynamo magnetic field. Of course if the disk is in a strong *outer* magnetic field (such as from a pulsar) this will alter the disk structure

in a very profound way, and disrupt the Shakura-Sunyaev model.

- Finally, we assume the α-disk prescription, described earlier.

These assumptions, together with the appropriate simplifications, lead us to the set of equations that constitute the quantitative aspect of this model. We will use the solutions of these equations later, to verify and justify all of the above assumptions.

3.4.5 Disk Equations

We now seek solutions for important disk parameters such as the disk thickness (or semi-thickness) H, surface density Σ and temperature T_c. We also need information on the behavior of solutions for opacity $\bar{\kappa}$ and pressure sources p_{rad} and p_{gas}. The governing equations our disk model become:

$$\begin{aligned}
\dot{M} &= -2\pi r v_r \Sigma \\
\Omega_K &= \left(\frac{GM}{r^3}\right)^{1/2} \\
\nu\Sigma &= \frac{\dot{M}}{3\pi}\left[1-\left(\frac{R}{r}\right)^{1/2}\right] \\
H &= \frac{c_s}{\Omega_K} \\
\Sigma &= 2\rho H \\
\frac{8\sigma}{3\tau}T_c^4 &= \frac{3GM\dot{M}}{8\pi r^3}\left[1-\left(\frac{R}{r}\right)^{1/2}\right] \\
c_s &= \left(\frac{p}{\rho}\right)^{1/2} \\
p &= \frac{2k}{m_p}\rho T_c + \frac{4\sigma}{3c}T_c^4 \\
\bar{\kappa} &= \kappa_{es} + \kappa_0 \rho T_c^{-7/2} \\
\tau &= \frac{\bar{\kappa}\Sigma}{2} \\
\nu &= \alpha c_s H
\end{aligned} \tag{3.68}$$

Now we can obtain expressions for all of our relevant physical quantities, and they will be functions of the radius r, with a dependence on the parameters $M, \dot{M}$ and α, which may be considered as input parameters. $\dot{M}$ may to some degree be considered a dynamic system parameter, but that would mean involving a description of the mass flow in the binary system (between disk and donor star) as a whole. We therefore consider $\dot{M}$ as a free input parameter, and we try to give good estimates on the possible and probable values of $\dot{M}$.

3.4.6 Solutions

The good thing is that the equation system (3.68) may be solved analytically to give explicit solutions for the disk. To achieve this we introduce the following dimensionless quantities

$$m = \frac{M}{M_\odot} \qquad \dot{m} = \frac{\dot{M}}{\dot{M}_{crit}} \qquad \bar{r} = \frac{r}{R} \tag{3.69}$$

where $M_\odot$ is the mass of the sun, $\dot{M}_{crit}$ is the critical mass accretion rate defined by (2.14), and we shall follow standard practice and put $\dot{M}_{crit} = 10^{-8}\, M_\odot\, \mathrm{yr}^{-1} = 6.4 \cdot 10^{14}\, \mathrm{kg\,s}^{-1}$. The radius scale parameter R is put equal to about one neutron star radius, where we for most cases believe that $R = 10\,\mathrm{km}$ is a reasonably probable value. We also define the quantity $f = 1 - (1/\bar{r})^{1/2}$. The solutions will have the following form

$$X = X_0\, \alpha^{p_1}\, m^{p_2}\, \dot{m}^{p_3}\, \bar{r}^{p_4}\, f^{p_5} \tag{3.70}$$

where X is the physical parameter, X_0 is a numerical constant (which carries the dimension of X) and p_1, p_2, p_3, p_4, p_5 are constants.

We will seek three different sets of solutions for (3.68). The three different sets will differ by our choice of equation of state $p(\rho, T)$ and opacity $\bar{\kappa}$. As I have mentioned earlier, there will be a radius r_{im} where the temperature and pressure is so high that radiation pressure dominates the gas pressure for all $r < r_{im}$, and likewise the gas pressure will be dominant for $r > r_{im}$. We take the region where they are comparable to be small relative to the disk scale. Also the choice of opacity plays a significant role in determining the disk structure. Much as the case for p, we define a radius r_{mo} to be the radius where the dominant opacity changes from free-free absorption κ_{ff} to scattering κ_{es}. Thus for $r > r_{mo}$ we take $\bar{\kappa} \simeq \kappa_{ff}$, and for $r < r_{bc}$ we have $\bar{\kappa} \simeq \kappa_{es}$. If we assume that $r_{mo} > r_{im}$ (which we will see is a good assumption), then this defines three regions in the disk. The solution of the disk equations (3.68) for these three different regions is very tedious, but relatively straight forward, and leads to the following results:

- **Inner region** ($r < r_{im}$)
  The radius is $r < r_{im}$, and we have radiation as the dominant pressure term $p_{rad} \gg p_{gas}$. Also we assume that $\kappa_{es} \gg \kappa_{ff}$.

$$\begin{aligned} H &= 3.6 \cdot 10^4 \, m \dot{m} f \text{ m} \\ \Sigma &= 5.2 \cdot 10^3 \, \alpha^{-1} \dot{m}^{-1} \bar{r}^{3/2} f^{-1} \text{ kg m}^{-2} \\ |v_r| &= 1.4 \cdot 10^8 \, \alpha \dot{m}^2 \bar{r}^{-5/2} f \text{ m s}^{-1} \\ T_c &= 3.2 \cdot 10^8 \, \alpha^{-1/4} m^{-1/4} \bar{r}^{-3/8} \text{ K} \\ p_{gas} &= 1.1 \cdot 10^8 \, \alpha^{-5/4} m^{-5/4} \dot{m}^{-2} \bar{r}^{9/8} f^{-2} \text{ Pa} \\ p_{rad} &= 3.3 \cdot 10^{13} \, \alpha^{-1} m^{-1} \bar{r}^{-3/2} \text{ Pa} \\ c_s &= 3.5 \cdot 10^8 \, \dot{m} \bar{r}^{-3/2} f \text{ m s}^{-1} \end{aligned} \tag{3.71}$$

- **Middle region** ($r_{im} < r < r_{mo}$)
  Here $r_{im} < r < r_{mo}$, and the dominant pressure term is gas pressure p_{gas}, but we still retain $\bar{\kappa} \simeq \kappa_{es}$.

$$\begin{aligned} H &= 1.8 \cdot 10^2 \, \alpha^{-1/10} m^{9/10} \dot{m}^{1/5} \bar{r}^{21/20} f^{1/5} \text{ m} \\ \Sigma &= 5.0 \cdot 10^5 \, \alpha^{-4/5} m^{1/5} \dot{m}^{3/5} \bar{r}^{-3/5} f^{3/5} \text{ kg m}^{-2} \\ |v_r| &= 4.7 \cdot 10^3 \, \alpha^{4/5} m^{-1/5} \dot{m}^{2/5} \bar{r}^{-2/5} f^{-3/5} \text{ m s}^{-1} \\ T_c &= 2.5 \cdot 10^8 \, \alpha^{-1/5} m^{-1/5} \dot{m}^{2/5} \bar{r}^{-9/10} f^{2/5} \text{ K} \\ p_{gas} &= 5.9 \cdot 10^{15} \, \alpha^{-9/10} m^{-9/10} \dot{m}^{4/5} \bar{r}^{-51/20} f^{4/5} \text{ Pa} \\ p_{rad} &= 9.8 \cdot 10^{17} \, \alpha^{-4/5} m^{-4/5} \dot{m}^{8/5} \bar{r}^{-36/10} f^{8/5} \text{ Pa} \\ c_s &= 2.0 \cdot 10^6 \, \alpha^{-1/10} m^{-1/10} \dot{m}^{1/5} \bar{r}^{-9/20} f^{1/5} \text{ m s}^{-1} \end{aligned} \tag{3.72}$$

- **Outer region** ($r > r_{mo}$)
  For $r > r_{mo}$ we have $p_{gas} \gg p_{rad}$, but now the absorption term κ_{ff} dominates the opacity.

$$\begin{aligned} H &= 1.1 \cdot 10^2 \, \alpha^{-1/10} m^{9/10} \dot{m}^{3/20} \bar{r}^{9/8} f^{3/20} \text{ m} \\ \Sigma &= 9.6 \cdot 10^5 \, \alpha^{-4/5} m^{1/5} \dot{m}^{7/10} \bar{r}^{-3/4} f^{7/10} \text{ kg m}^{-2} \\ |v_r| &= 2.5 \cdot 10^3 \, \alpha^{4/5} m^{-1/5} \dot{m}^{3/10} \bar{r}^{-1/4} f^{-7/10} \text{ m s}^{-1} \\ T_c &= 7.0 \cdot 10^7 \, \alpha^{-1/5} m^{-1/5} \dot{m}^{3/10} \bar{r}^{-3/4} f^{3/10} \text{ K} \\ p_{gas} &= 1.1 \cdot 10^{16} \, \alpha^{-9/10} m^{-9/10} \dot{m}^{17/20} \bar{r}^{-21/8} f^{17/20} \text{ Pa} \\ p_{rad} &= 1.2 \cdot 10^{16} \, \alpha^{-4/5} m^{-4/5} \dot{m}^{6/5} \bar{r}^{-3} f^{6/5} \, [Pa \\ c_s &= 1.1 \cdot 10^6 \, \alpha^{-1/10} m^{-1/10} \dot{m}^{3/20} \bar{r}^{-3/8} f^{3/20} \text{ m s}^{-1} \end{aligned} \tag{3.73}$$

First, we note that the unknown parameter α does not enter any of the expressions for disk quantities with a high power. This means that the very reasonably looking orders

of magnitude of these quantities are not particularly sensitive to the actual value of α, which is good since our knowledge of α only limits its likely value to $0.1 \lesssim \alpha \lesssim 1$, and thus we can have some confidence in the general picture of the disk structure given by (3.71), (3.72) and (3.73). On the other hand, it also means that we cannot expect to discover the typical size of α by comparing theory with observations. Also m does not enter the solutions with high power, and if we take the compact object to be a neutron star then the expected value of m will be in the vicinity of the Chandrasekhar limit of $1.4\,M_\odot$ (though there have been reports of neutron star masses as high as $2\,M_\odot$). We can therefore take all powers of m to be ~ 1 here.

Some parameters are independent of choice of opacity and equation of state in the disk, and thus do not depend directly upon disk parameters such as T_c or ρ, therefore their expressions do not vary for the different regions in the disk:

$$\begin{aligned} D(r) &= 2.4 \cdot 10^{21}\, m^{-1}\, \dot{m}\, \bar{r}^{-3}\, f^{1/2}\ \mathrm{J\,m^{-2}\,s^{-1}} \\ v_\phi &= 1.2 \cdot 10^{8}\, m^{1/2}\, \bar{r}^{-1/2}\ \mathrm{m\,s^{-1}} \\ \Omega_K(r) &= 1.2 \cdot 10^{4}\, m^{1/2}\, \bar{r}^{-3/2}\ \mathrm{s^{-1}} \end{aligned} \tag{3.74}$$

We now calculate the radii r_{im} and r_{mo} by using (3.71), (3.72) and (3.73).

- ***r_{im} ($p_{rad} = p_{gas}$)***
  For r_{im} we get with $p_{rad} = p_{gas}$ from (3.72)

$$\bar{r}\, f^{-16/21} = 1.37 \cdot 10^{-19} \left(\frac{T_c^{\,3}}{\rho}\right)^{20/21} \alpha^{2/21}\, m^{2/21}\, \dot{m}^{16/21} \tag{3.75}$$

  If we set $f \simeq 1$ for radii concerned, and insert the expressions for T_c and ρ we get

$$\bar{r} = 135\ \alpha^{2/21}\, m^{2/21}\, \dot{m}^{16/21} \tag{3.76}$$

  An identical estimate is produced with (3.71). Now α is in the range $0.1 - 1 \Rightarrow \alpha^{2/21} \simeq 1$, and also $m \sim 1 \Rightarrow m^{2/21} \simeq 1$. We then see that at the critical mass flow rate $\dot{m} \sim 1$, the radius $\bar{r}_{im}$ that signifies the transfer from the inner to the middle region is $\bar{r}_{im} \simeq 135 \Rightarrow r_{im} = 1350\,\mathrm{km}$. We can deduce from (3.76) that there are values for $\dot{m}$ for which the radius r_{im} becomes too small for this inner region to exist at all. If we demand that $\bar{r}_{im} \gtrsim n$, where $n = 1$ would put $\bar{r}_{im}$ at the neutron star surface, we get a limit on $\dot{m}$ for the inner region to exist

$$\dot{m} \gtrsim \left(\frac{n}{135}\right)^{21/16} \alpha^{-1/8} m^{-1/8} \tag{3.77}$$

- $r_{mo}\,(\kappa_{es} = \kappa_{ff})$

  The radius r_{mo} is estimated in the same manner. We use (3.73) and put $\kappa_{es} = \kappa_{ff}$ to get

$$\bar{r}\, f^{-2/3} = \left(\frac{0.038}{\kappa_0}\right)^{4/3} \left(\frac{T_c^{7/2}}{\rho}\right)^{4/3} \dot{m}^{2/3} \tag{3.78}$$

  Based on (3.72) we get a practically identical estimate. If we again set $f \simeq 1$ for the radii concerned, and insert the expressions for T_c and ρ, and a value for κ_0, we get

$$\bar{r} = 2009\ \dot{m}^{2/3} \tag{3.79}$$

  For $\dot{m} \sim 1$ we get $\bar{r}_{mo} \simeq 2000 \Rightarrow r_{mo} = 2 \cdot 10^4\,\mathrm{km}$.

In Fig. 3.5 we see p_{rad} and p_{gas} as functions of $\bar{r}$, and the value of r_{im} can be read off. It is, as we can see, about the same order as given by (3.76).

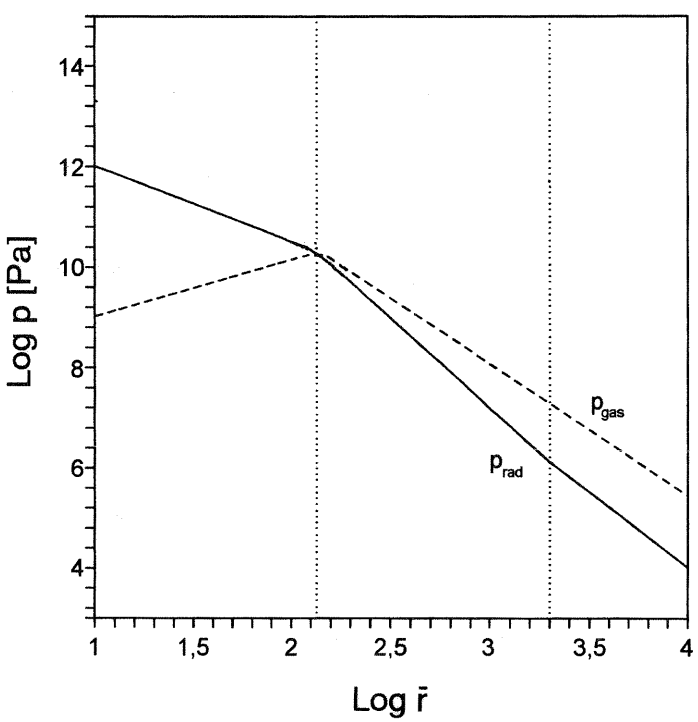

Fig. 3.5 *A graphical depiction of pressure terms p_{rad} and p_{gas} as functions of $\bar{r}$, for $\dot{m} = 1$. Both radii r_{im} and r_{mo} are marked with vertical lines.*

In Fig. 3.6 we see κ_{es} and κ_{ff} as functions of $\bar{r}$, where it is clear that $r_{mo} \simeq 2000$.

It should be emphasized that in the very outer regions of an accretion disk the gas may not be completely ionized, and that other opacity sources also may contribute in these regions. Bound-free absorption is such a source, it occurs when an atom with bound electrons absorbs photons of sufficient energy to ionize the atom. There may also be small contributions from bound-bound line transitions. In the inner region of the disk other opacity sources must be taken into consideration, such as for instance Comptonizarion. These matters will be dealt with later, during the discussion of disk spectra.

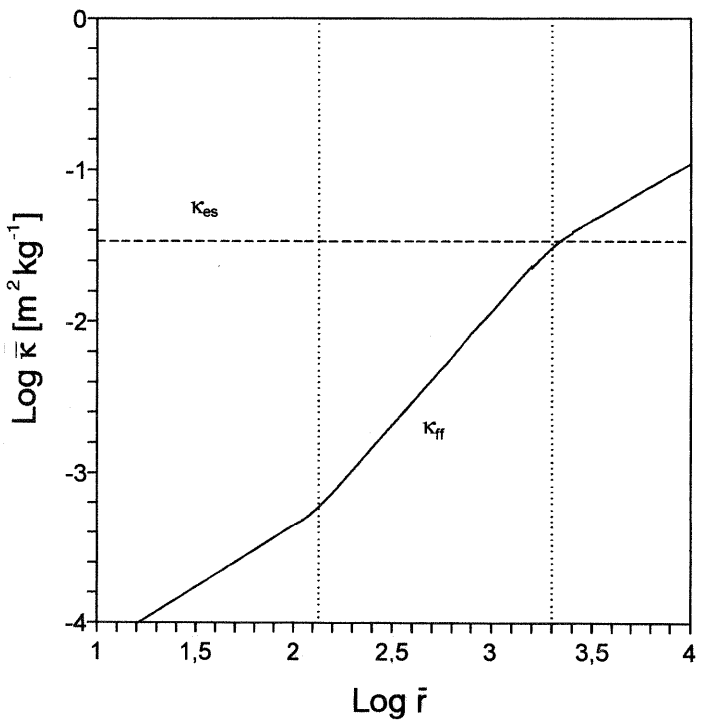

Fig. 3.6 *Opacities κ_{es} and κ_{ff} as functions of $\bar{r}$ for $\dot{m} = 1$. Both radii r_{im} and r_{mo} are marked with vertical lines.*

The radii r_{im} and r_{mo} and indeed many other parameters in the disk solutions do depend on the mass transfer rate $\dot{m}$. Though we have considered $\dot{m}$ to be an input parameter, it is a likely (and observed) feature that for most accretion disks (for a number of possible reasons) the mass transfer rate $\dot{m}$ will vary. This variation may cause the disk structure to change, and the parameters (for instance the disk temperature T_c) will change. This alteration can affect such things as energy balance and transport, and also the opacity environment. In Fig. 3.7 we see how the different physical regions of the disk change as a function of $\bar{r}$ and $\dot{m}$. For $\mathrm{Log}\,\dot{m} = 0 \rightarrow \dot{m} = 1$, we recover our earlier estimates for r_{im} and r_{mo}, and for $\mathrm{Log}\,\dot{m} = -3 \rightarrow \dot{m} = 10^{-3}\,\dot{M}_{crit}$ we also recover (3.77) for $n = 1$.

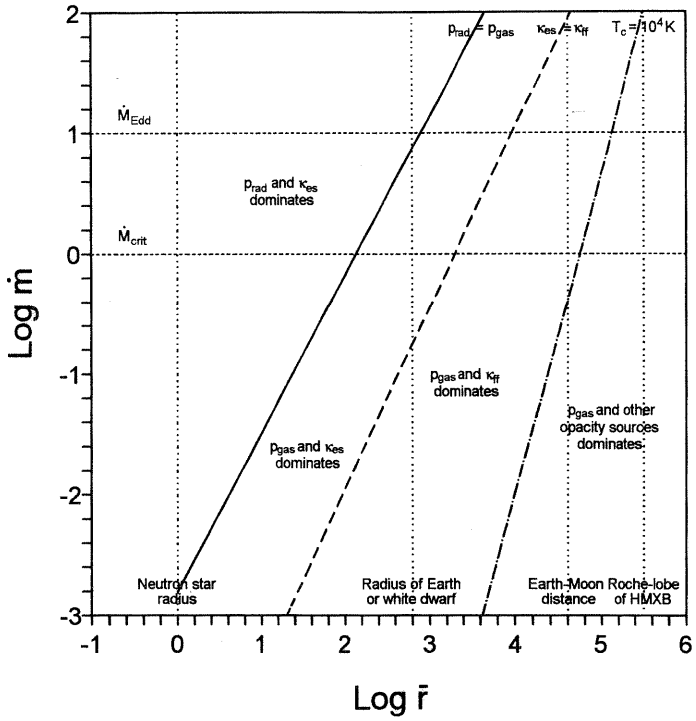

Fig. 3.7 *The different regimes in the disk plotted as functions of $\bar{r}$ and $\dot{m}$. Some important radii are marked with vertical lines.*

We see from the solutions (3.71), (3.72) and (3.73) that the height (or thickness) of the disk is constant for the radiation pressure dominated (inner) region. This results from the fact that the radiation pressure force is balancing the z-component of gravity. In Fig. 3.8a we see a slice of the disk from the side, and it is clear from this that the disk faces actually are concave. That disks actually are concave is shown in models of the observed reflection (caused by irradiation) from the disks in the Cataclysmic Variables *DQ Her* and *UX UMa* [43]. This concavity is necessary to obtain hydrostatic equilibrium in the thin accretion disk, because unlike for stars where the self-gravity secures this equilibrium, a disk can only rely on the gravity from the compact object. In the absence of self-gravity this concave shape is the only shape is which the gravity from the compact object has a z-component to ensure hydrostatic equilibrium.

In Fig. 3.8b we see the disk from another perspective, high above (or below) the disk plane. In Fig. 3.9 we see the disk structure in 3-dimensions. It should be stressed that while Fig. 3.8b is to scale (it portrays the disk on the scale it would appear), the other two Fig. 3.8a and Fig. 3.9 are not, as can be seen from the axes on the figure. If for instance Fig. 3.9 was shown to scale, the disk would appear somewhat thinner.

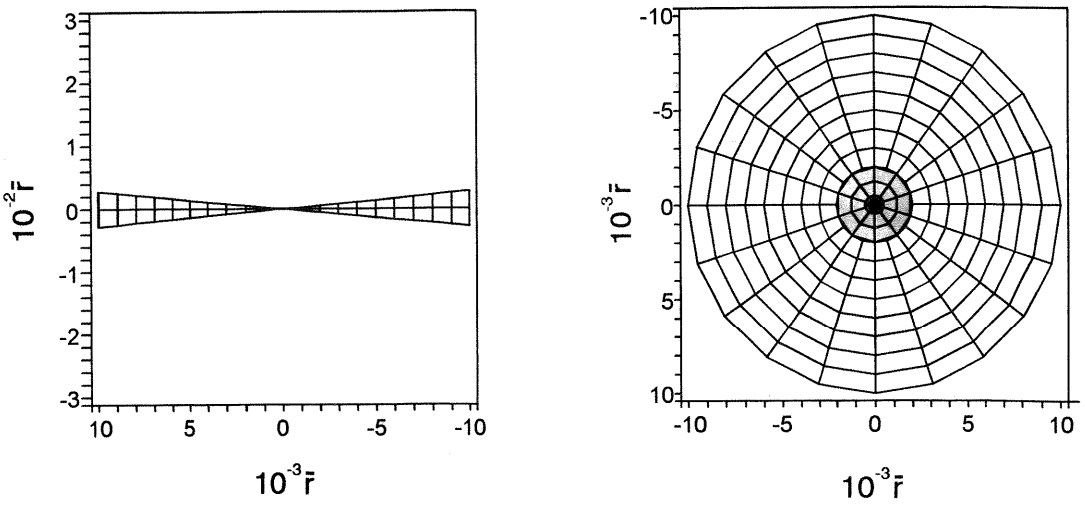

Fig. 3.8ab *Fig. 3.8a shows the vertical structure through the entire diameter, while Fig. 3.8b shows the disk from a vantage point high above the disk plane.*

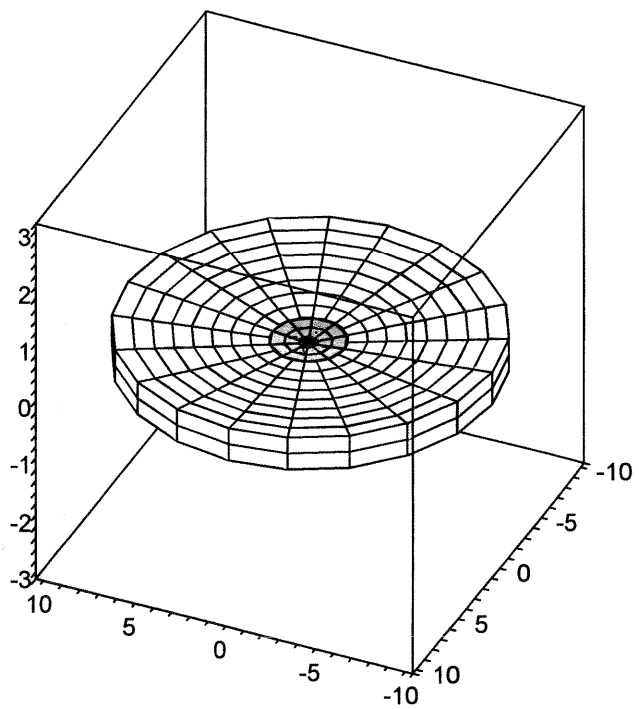

Fig. 3.9 *The disk structure in 3-dimensions. The disk is plotted with $m = \dot{m} = \alpha = 1$, and appears slightly thicker than it really is. The scale can be read off from Fig. 3.8ab.*

Several assumptions were made regarding the disk structure, and in the remains of this subchapter we will now verify and discuss these, using the disk solutions (3.71), (3.72) and (3.73).

Self Gravity

At the disk surface $z = H$ the z-component of the gravitational force from the compact object on an element of mass m at radius r is $GMmH/r^3$. If we assume that the disk is an infinite uniform plane with density ρ, then the gravitational force on a mass m at height H is $G\rho Hm$. Thus the condition for the neglect of self-gravitation (and therefore for stability against breaking up into self-gravitating clumps) is

$$\rho \ll \frac{M}{r^3} = 10^{18}\,\bar{r}^{-3}\ \mathrm{kg\,m^{-3}} \tag{3.80}$$

From the set (3.71), (3.72) and (3.73), we can see that this is clearly satisfied for all disk radii, and the neglect of self-gravity of the disk is fully justified.

Timescales and Velocities

There are several good reasons for studying the time dependent behavior of disks. As mentioned before, the observable properties of steady-state, optically thick disks are largely independent of viscosity, this means that observations of steady disks are unlikely to give much information about the viscosity. The time dependence of disk flow is on the other hand largely controlled by the viscosity. Hence observations of the time dependent aspects of disk behavior offer one of the few sources of quantitative information about the disk viscosity. We here define four different timescales

- **Viscous timescale**
  This is the typical timescale on which matter diffuses radially through the disk under the influence of viscous torques. We put as in (3.26)

$$t_{visc} = \frac{r}{v_r} \sim \frac{r^2\Sigma}{\dot{M}} \sim \frac{1}{\alpha\Omega_K}\left(\frac{r}{H}\right)^2 \tag{3.81}$$

- **Dynamical timescale**
  This is the timescale associated with the gas flow in the ϕ-direction, that is the gas flow orbiting the compact object.

$$t_{dyn} = \frac{r}{v_\phi} \sim \frac{1}{\Omega_K} \tag{3.82}$$

- **Hydrostatic timescale**
  This measures the time at which deviations from hydrostatic equilibrium in the z-direction is smoothed out (or communicated). We define

$$t_{hyd} = \frac{H}{c_s} = \frac{1}{\Omega_K} \sim t_{dyn} \tag{3.83}$$

- **Thermal timescale**
  We define this to be the timescale for re-adjustment to thermal equilibrium, if for instance the dissipation rate is altered. This can be found as the ratio of the heat content per unit disk area, to the viscous dissipation rate per unit disk area. Since the heat content per unit volume of the gas is $\sim \rho kT/m_p \sim \rho {c_s}^2$, we get

$$t_{th} \sim \frac{\Sigma {c_s}^2}{D(r)} \sim \frac{1}{\alpha \Omega_K} \tag{3.84}$$

From all of the above we may gather

$$t_{dyn} \sim t_{hyd} \sim \alpha\, t_{th} \sim \alpha \left(\frac{H}{r}\right)^2 t_{visc} \tag{3.85}$$

It is thus clear that our demand (3.26) of rapid rotation with slow inflow is satisfied if the thin disk assumption $H \ll r$ holds. The thin disk assumption again lends its support to the relation between the flow velocities. In Fig. 3.10 we see the three velocities v_ϕ, c_s and v_r associated with the flow as functions of $\bar{r}$. We take the non-relativistic limit to be $v_\phi \sim c/10$, which is marked in the figure.

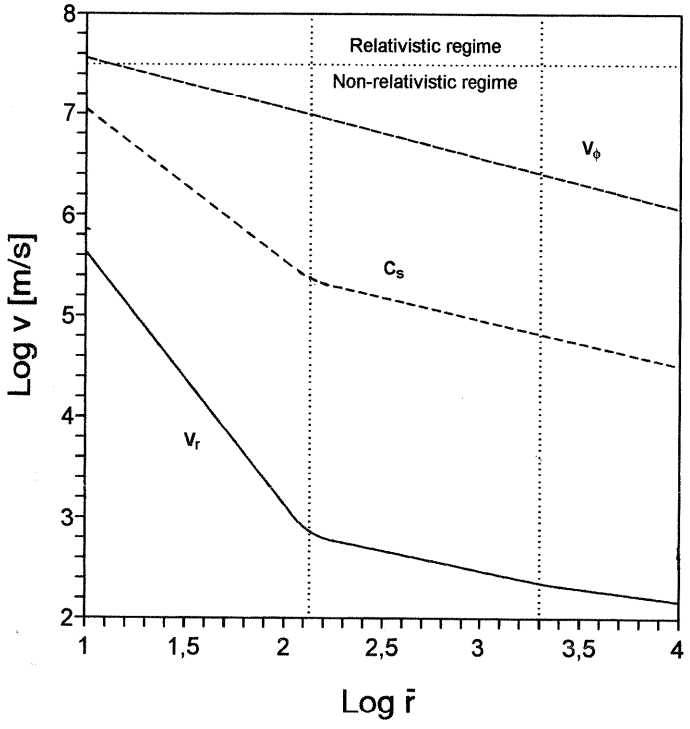

Fig. 3.10 *The velocities v_ϕ, c_s and v_r as functions of $\bar{r}$ for $\dot{m} = 1$.*
Both radii r_{im} and r_{mo} are marked with vertical lines.
The non-relativistic limit $v_\phi \sim c/10$ is marked with a horizontal line.

It is clearly seen that the Kepler-velocity $v_\phi \gg c_s$, except for the extreme inner parts of the disk. Many anomalities arise there, and some aspects of the solutions in that region are highly questionable. We also see that $v_r \ll c_s$ for the entire disk. The order of magnitudes are (with the exception of the extreme inner disk for which $\bar{r} \lesssim 10$): $v_\phi \sim 10^7\,\mathrm{m\,s^{-1}} \sim c/10$, $c_s \sim 10^5\,\mathrm{m\,s^{-1}}$ and $v_r \sim 10^3\,\mathrm{m\,s^{-1}}$. Generally we would have

$$|v_r| \sim \alpha c_s \frac{H}{r} \qquad v_\phi \sim c_s \frac{r}{H} \qquad v_z \sim 0 \tag{3.86}$$

and since $|v_r| \ll c_s \ll v_\phi$ we deduce that the thin disk assumption $H \ll r$ holds for all radii (except possibly for small $\bar{r}$). The fact that $v_r \sim 10^3\,\mathrm{m\,s^{-1}}$ means that the timescale t_{visc} is of the order days (or possibly weeks), which again means that even for very high mass transfer rates the total mass of the disk $M_{disk} \ll M$ at all times. From the fact that $H \ll r$ we also conclude that

$$t_{dyn} \sim t_{hyd} \lesssim t_{th} \ll t_{visc} \tag{3.87}$$

Thin Disk Assumption

We have seen signs that the thin disk assumption may break down in the inner region of the disk. This is a general feature of thin disks, and in order to quantify this we look at our equations (3.68). We can try to derive a useful expression for the scale height H of the region dominated by radiation pressure. If we use

$$c_s^2 = \frac{p}{\rho} \qquad p = p_{rad} = \frac{4\sigma}{3\tau} T_c^4 \qquad \frac{8\sigma}{3\tau} T_c^4 = D(r) \tag{3.88}$$

we get

$$c_s^2 = \frac{3GM\dot{M}\tau}{8\pi r^3 \rho c} \left[1 - \left(\frac{R}{r} \right)^{1/2} \right] \tag{3.89}$$

Since $\rho = \Sigma/H$ and $\tau = \Sigma \bar{\kappa}_R$ we get $\tau \simeq \rho H \sigma_T / m_p$, and with $H = c_s/\Omega_K$ we have

$$H \simeq \frac{3\sigma_T \dot{M}}{8\pi m_H c} \left[1 - \left(\frac{R}{r} \right)^{1/2} \right] \tag{3.90}$$

Hence in the inner regions of the disk H is essentially independent of r. This comes about as a result of the fact that the radiation pressure force is balancing the component of gravity that pulls the disk together in the vertical direction (i.e. the z-component). We have seen that the mass accretion rate corresponding to the Eddington-luminosity L_{Edd} is given by

$$\dot{M}_{crit} = \frac{L_{Edd}}{2\beta} \left(\frac{R}{GM} \right) = \frac{2\pi R m_p c}{\sigma_T} \tag{3.91}$$

where we have used (2.12) for L_{Edd}, and the efficiency $\beta \simeq 0.15$ for a neutron star. We then see that (3.123) can be expressed as

$$H \simeq \frac{3R}{4\beta}\dot{m}\left[1-\left(\frac{R}{r}\right)^{1/2}\right] \tag{3.92}$$

This equation shows that at accretion rates $\dot{m} = \dot{M}/\dot{M}_{crit} \simeq 1$, the thin disk approximation must break down in the inner region. This is plotted in Fig. 3.11 for $\dot{m} = 1$ and $\beta = 0.15$. I have used $r/H \lesssim 10 \Rightarrow H \gtrsim \bar{r}$ as condition for thin disk breakdown. We see that $H = \bar{r}$ occurs for $\bar{r} \simeq 60$ which is about in the middle of the inner region. For even greater $\dot{m}$ the thin disk breakdown extends to even larger radii in the disk.

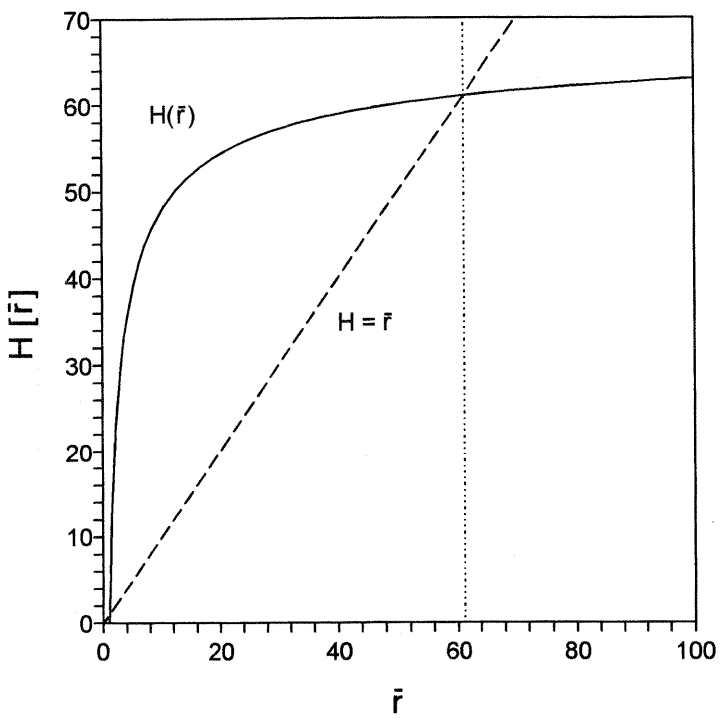

Fig. 3.11 *The scale height H for the radiation pressure dominated inner region of the disk plotted as function of $\bar{r}$. The thin disk breakdown criterium is $H \gtrsim \bar{r}$*

Hence for near-critical accretion rates, radiation pressure acts to make the inner parts of the disk quasi-spherical, or bloated. Other situations where this might happen is if the temperature T_c becomes very high, for example if the cooling mechanism is inefficient, so that the disk is heated and greatly exceeds the blackbody temperature.

Opacity

As for the opacity we have assumed that the disk is optically thick, i.e. that the optical depth $\tau \gg 1$. As long as free-free absorption dominates ($r > r_{mo}$) we take $\tau = \kappa_{ff}$, but

when electron scattering dominates ($r < r_{mo}$) we use the effective optical depth defined by $\tau^* \equiv \sqrt{\kappa_{es}\kappa_{ff}}\,\rho H$ [29]. We then have for the outer, middle and inner region

$$\begin{aligned} \tau_o &= 5.3 \cdot 10^1\ \alpha^{-4/5}\, m^{1/5}\, \dot{m}^{1/5}\, f^{17/10} \\ \tau_m^* &= 2.0 \cdot 10^1\ \alpha^{-4/5}\, m^{1/5}\, \dot{m}^{1/10}\, \bar{r}^{3/20}\, f^{17/10} \\ \tau_i^* &= 2.7 \cdot 10^{-5}\ \alpha^{-17/16}\, m^{-1/16}\, \dot{m}^{-2}\, \bar{r}^{93/32}\, f^{-2} \end{aligned} \tag{3.93}$$

In Fig. 3.12 we see the optical depth τ plotted as function of $\bar{r}$. We see that the optical thickness assumption is justified for the middle and outer region, since $\tau \gg 1 \Rightarrow \mathrm{Log}\,\tau \gtrsim 2$. In the inner region however the optical thickness assumption $\tau \gg 1$ seems to break down. This may be because the disk actually becomes optically thin, or that there are opacity sources (such as for instance Comptonization) that needs to be included.

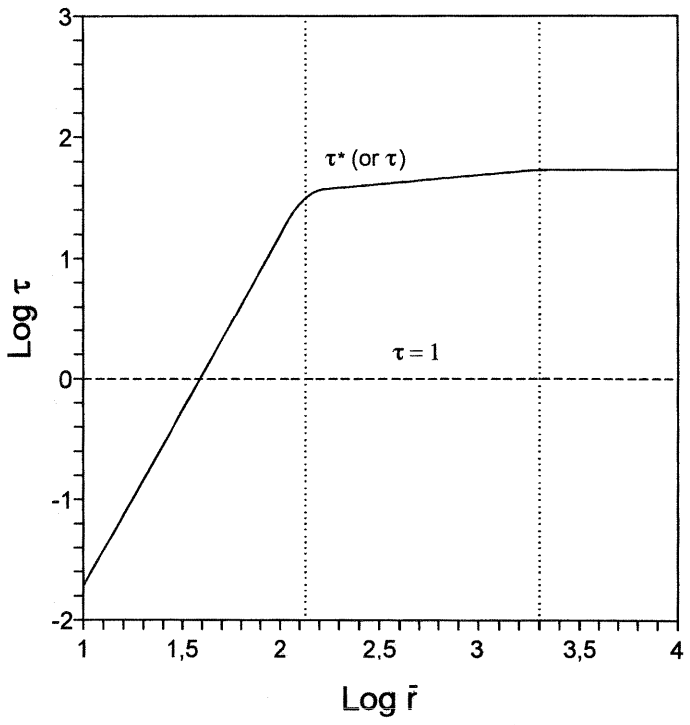

Fig. 3.12 *The optical depth τ (or τ^* for $r < r_{mo}$) as function of $\bar{r}$. The horizontal line represents $\mathrm{Log}\,\tau = 0 \Rightarrow \tau = 1$.*

Some of our assumptions and equations regarding the disk structure seems to lose their validity, or take on strange behavior, in the inner regions of the disk. As we see above, this is also the case for the optical depth τ. We do not take this to seriously however, since our following study will concern magnetized neutron stars (pulsars), in which most (or all) of the inner parts of the disk is probably disrupted or at least heavily perturbed

by the magnetic field of the pulsar. We shall return to these matters later, but for now we conclude that all of our solutions and assumptions for the middle and outer regions ($r > r_{im}$) of the disk returns good results.

3.5 Disk Spectra

It is important to be able to verify to what extent the accretion disk paradigm (and the plethora of different models) presented here, is supported by observations. The main tool in this undertaking is the observed radiation originating from such systems, that is the disk spectra and their many different modes of variation. Some of the variations and modulations that are caused by movement or changes in the binary system are mentioned in Chapter 1. It is important to realize that the spectrum of radiation which originate from the body of the disk itself, is sometimes not identical to the observed spectrum. The radiation may be modified for a number of reasons. Clearly, the radiation from any source in the Universe as it is observed by an observer on Earth, is affected by such things as interstellar gas and dust, the Earth's atmosphere etc., but we here limit our list to sources within the X-ray system itself.

- In the vicinity of accretion disks there are several luminous radiation sources, which are often powered by the accretion disk itself. If the intensity of these sources become high enough, their radiation may influence the disk. This gives rise to so-called *irradiated disks* which are discussed to some degree later.

- Around a black hole and a neutron star, the relativistic effects, such as *gravitational focusing* (the gravitational bending of light), *gravitational redshift* and *Doppler effects* connected with the disk rotation, may significantly modify the spectra.

- In some disk systems the existence of a *disk corona* is possible. It appears that the mass of this corona is very small compared to the disk mass, and that the corona therefore has very little impact on the disk structure or dynamics. It can however have a sizable influence on the disk spectra, since radiation will be absorbed and scattered in this corona. It is assumed that the temperature of this corona (much like the solar corona) is substantial ($T \sim 10^7\,\mathrm{K}$), and that the corona therefore in fact is an X-ray source on its own. This is clearly seen in the before mentioned system *Her X-1*, where the X-ray producing central parts of the disk is in an off-state when it is shielded from us, but where about $\sim 5\%$ of the intensity remains. This can be explained as reflection of X-rays by a hot ($T \sim 10^7\,\mathrm{K}$) medium above the disk plane [41]. Some of the aspects concerning disk coronae are still dubious, especially the heating mechanisms.

To study actual accretion flow in X-ray binaries we require binary systems in which the radiation is dominated by the disk contribution. High luminosity systems containing neutron stars or black holes largely fail to satisfy this criterium, because the accretion luminosity in these systems is radiated for the most part as hard X-rays, where it gives some information about the accretion process very close to the compact object, but very little about any possible disk flow. In addition to this, most of these systems have companions that are O or B giant or supergiant stars. These stars produce luminosities that are at least comparable to the non-inner disk luminosity, and often radiate in the same frequency area (UV, optical) as the non-inner disk, thereby completely swamping the non-inner disk contribution, and leaving only the X-rays (from the inner disk) to be observed.

Cataclysmic Variables

We clearly need systems where the donor star is lower main sequence ($0.1\,M_\odot \lesssim M_d \lesssim 1\,M_\odot$). This leaves us with two candidates: The LMXB (discussed in Chapter 2) and Cataclysmic Variables. Positively identified and well established LMXB that are not to distant, are very few, and suffer to a certain degree from much of the same shortcomings as their cousins, the HMXB discussed above. The Cataclysmic Variables (CVs) or dwarf novae are accretion disk systems containing white dwarfs as compact objects, and donor stars that are small and faint lower main sequence stars (the name Cataclysmic springs from the fact that many of them exhibit dramatic outbursts). Many such systems are observed in the stellar neighbourhood ($\lesssim 1000$ ly). These systems are extremely useful for calibrating accretion disk models, and for gaining knowledge of actual accretion flow. They radiate with lower luminosities than the X-ray binaries containing neutron stars and black holes, but the CVs radiate basically with the same spectrum (UV, optical) as the non-inner parts of more luminous disks, and are therefore very good systems for checking general basic accretion flow models. Since the outer regions of disks in CVs are not necessarily completely ionized, these disks may even radiate in the infrared spectrum. In Chapter 1, facts and observations were mentioned as direct support of the accretion disk model, most of these come from observations in CVs.

3.5.1 Blackbody Spectra

The temperature T appearing in the disk structure equations (3.68) refers to the interior temperature at $z = 0$. In general $T > T_s$, where T_s is the temperature of the surface at which the emergent photon spectrum is formed. Due to (3.56) we need a temperature gradient in order to drive the photon flux. T and T_s becomes comparable whenever the disk becomes optically thin to absorption.

When the disk is optically thick and absorption dominates scattering, the local emission

will be blackbody. In such regions the spectrum will be described by a Planck function at a temperature T_s, using (3.65)

$$T_s(r) = \left[\frac{F(r)}{a}\right]^{1/4} = 5 \cdot 10^7 \; m^{-1/2} \dot{m}^{1/4} \bar{r}^{-3/4} f^{1/4} \; \mathrm{K} \tag{3.94}$$

This temperature characterizes the matter at optical depth $\tau_{ff} \simeq 1$ below the actual surface. It is at this depth that a typical escaping photon is created before emerging from the surface. Escaping photons of a particular frequency ν are created at $\tau_{ff,\nu}$. We defined the (differential) optical depth in Appendix A to be $d\tau_\nu \equiv \kappa_\nu \rho \, ds$, and we therefore put $\tau_{ff,\nu} = \kappa_{ff,\nu} \rho \Delta z$. Photons created at larger values of $\tau_{ff,\nu}$ are absorbed prior to escaping from the outer surface. Accordingly, the intensity of the emerging radiation is given by adding up the emission in the layers from $z = 0$ to $z = H - \Delta z$. Again if we assume homogeneous and isothermal conditions we get

$$I_\nu \simeq j_{ff,\nu} \, \Delta z \sim \frac{j_{ff,\nu}}{\kappa_{ff,\nu} \, \rho} = B_\nu(T_s) \tag{3.95}$$

where $j_{ff,\nu}$ is the free-free emissivity of the plasma (defined in Appendix 1), and B_ν is the Planck-function

$$I_\nu = B_\nu = \frac{2h\nu^3}{c^2} \frac{1}{e^{h\nu/kT_s(r)} - 1} \tag{3.96}$$

and where Kirchoff's law (A.5) is applied. The flux crossing outward through the surface is then related to the intensity I_ν by

$$\begin{aligned} F_{\nu,outer} &= \int_0^{\pi/2} I_\nu \cos\theta \, d\Omega \simeq 2\pi B_\nu(T_s) \\ &= 8.3 \cdot 10^{-19} T_s^3 \frac{x^3}{e^x - 1} \end{aligned} \tag{3.97}$$

If we integrate we then get the familiar blackbody result

$$F_{outer} = \int_0^\infty F_\nu \, d\nu \simeq a T_s^4 \tag{3.98}$$

which is valid for $\kappa_{ff} \gg \kappa_{es}$. Thus for radii $r > r_{mo}$ where absorption dominates scattering, we see that according to (3.94) the disk will radiate a blackbody spectrum with a temperature in the order $\sim 10^4$ K for the outer parts, rising to $\sim 10^5$ K towards the transition at $r = r_{mo}$. This is a *multi color* blackbody spectrum since the temperature is a function of radius $T_s = T_s(r)$, and all of the above equations should therefore be taken per radius.

If we want the total observed spectrum S_ν from the disk, we must take (3.97) to be integrated across the face of the disk for the radii it applies. We can thus put

$$S_{\nu,outer} = A \int_{r_{mo}}^{R_d} F_{\nu,outer}[T_s(r)]\, 2\pi r\, dr \tag{3.99}$$

where $A = (\cos i)/D^2$ is a constant, and R_d is the maximum disk radius. D is the distance to the observer and i is the inclination angle of the disk. Since we are mainly interested in the ν-dependence of S_ν we simply put $i = 0$ (we observe the disk from directly above) and $D = 1$ (we assume that D is measured on a scale such that the observer is located at this point). In order to evaluate the integral we need a function that describes the temperature T_s as a function of radius, and this can be gathered from (3.73). If we take $T \propto r^{-p}$ as a parametrization for the temperature we can compute the integral (3.99), if we do (it is practical to turn it into an integral over $x = h\nu/kT$ rather than r), we get

$$S_\nu \propto \nu^{3-(2/p)} \int_{x_{mo}}^{x_d} \frac{x^{(2/p)-1}}{e^x - 1}\, dx \propto \nu^{0.33} \tag{3.100}$$

with

$$x_{mo} = \frac{h\nu}{kT_{mo}} \qquad x_d = \frac{h\nu}{kT_d}\left(\frac{R_d}{r_{mo}}\right)^p \tag{3.101}$$

and where the value $p = 3/4$ is gathered from (3.72). It is thus clear that an upper limit for the frequency where this blackbody spectrum contributes is $\nu_{mo} = kT_{mo}/h$. For T_{mo} in the order of $\sim 10^5 - 10^6$ K (3.72) we get $\nu_{bb}^{upper} \simeq 5 \cdot 10^{15}\,\mathrm{s}^{-1}$. We see that the frequency range for this blackbody spectrum is quite limited since $(R_d/r_{mo}) \simeq 5$ we get that the lower frequency is $\nu_{bb}^{lower} \simeq 10^{15}\,\mathrm{s}^{-1}$.

It is clear that the total luminosity from this part of the disk L_{outer} is

$$L_{outer} = \int_0^\infty S_{\nu,outer}\, d\nu = \int_{r_{mo}}^{R_d} aT_s^4(r)\, 2\pi r\, dr \tag{3.102}$$

where (3.98) is used.

3.5.2 Modified Blackbody Spectra

We will now consider the region $r_{im} < r < r_{mo}$ where electron scattering dominates absorption for typical photons. Following emission, photons may undergo many (nearly) elastic scatterings before escaping from the surface. These random scatterings will cause a typical photon to diffuse through the disk to the outer surface. Let $\Delta\hat{z}$ be the vertical

depth below the surface at which an escaping photon of frequency ν was created by free-free emission. Let Δs be the total path length traversed by the photon in its random walk prior to escape. Accordingly,

$$\tau_{ff,\nu} \simeq 1 \simeq \kappa_{ff,\nu}\rho\,\Delta s \tag{3.103}$$

Adding up the emission from the region $0 \leq z \leq \Delta\hat{z}$ again gives the emergent intensity

$$I_\nu \simeq j_\nu \Delta\hat{z} \tag{3.104}$$

This quantity $\Delta\hat{z}$ is less than Δz found in the subsection above, where we ignored scattering. This random wandering of the photon enhances the probability for absorption prior to escape and thus reduces the depth at which the emission contributes to the emergent flux. If $N_{\nu s}$ is the total number of scatterings prior to escape, then

$$N_{\nu s} = \frac{\Delta s}{\lambda_{es}} \qquad \lambda_{es} \simeq \frac{1}{\kappa_{es}\rho} \tag{3.105}$$

where λ_{es} is the mean free path for scattering. Since scattering induces a random-walk photon motion, the net distance traversed in the vertical direction is then $\sqrt{N_{\nu s}}\,\lambda_{es}$. We then have

$$\Delta\hat{z} = N_{\nu s}^{1/2}\lambda_{es} \tag{3.106}$$

And by combining these equations we have $N_{\nu s} \simeq \kappa_{es}/\kappa_{ff,\nu}$, and therefore

$$\Delta\hat{z} \simeq \frac{1}{(\kappa_{es}\kappa_{ff,\nu})^{1/2}\rho} \simeq \Delta z \left(\frac{\kappa_{ff,\nu}}{\kappa_{es}}\right)^{1/2} \tag{3.107}$$

since $\Delta z \simeq 1/\kappa_{ff,\nu}\rho$. Putting this into (3.104) gives the intensity

$$I_\nu \simeq \frac{j_{ff,\nu}}{\kappa_{ff,\nu}\rho}\left(\frac{\kappa_{ff,\nu}}{\kappa_{es}}\right)^{1/2} \simeq B_\nu(T_s)\left(\frac{\kappa_{ff,\nu}}{\kappa_{es}}\right)^{1/2} \tag{3.108}$$

where we have used (3.95). So far we have used a gray approximation when it comes to opacity, in that $\kappa_{ff,\nu}$ have been replaced with a ν-averaged κ_{ff}. We shall now need the full opacity coefficient for free-free absorption in ionized hydrogen [38]

$$\kappa_{ff,\nu} = 1.5 \cdot 10^{24}\,\rho T^{-7/2} g_{ff} \frac{1-e^{-x}}{x^3} \tag{3.109}$$

where g_{ff} is a slowly varying Gaunt factor of unit order, and where $x = h\nu/kT$. We see that with $B_\nu = 2hc^{-2}\nu^3/(e^x - 1)$, and keeping $x = h\nu/kT$, we get

$$F_{\nu,middle} \simeq 2\pi \left(\frac{2h}{c^2}\frac{\nu^3}{e^x-1}\right)\left[(1.5\cdot 10^{24})^{1/2}\,\kappa_{es}^{-1/2}\rho^{1/2}\,T^{-7/4}\,\frac{(1-e^{-x})^{1/2}}{x^{3/2}}\right]$$
$$= 5.1\cdot 10^{-6}\,\rho^{1/2}\,T^{5/4}\left(\frac{x^3\,e^{-x}}{e^x-1}\right)^{1/2} \tag{3.110}$$

which is a modified blackbody spectral distribution. If we integrate this expression over all ν by converting it to an integral over x, we get the total flux at radius r

$$F_{middle} \simeq 1.6\cdot 10^5\,\rho^{1/2}\,T^{9/4} \tag{3.111}$$

where it is assumed that scattering dominates absorption also for low ν ($x \ll 1$), and where a numerical integration yields $\int_0^\infty \sqrt{\frac{x^3e^{-x}}{e^x-1}}\,dx \simeq 1.5$. In much the same way as for the absorption dominated case, we can calculate the accompanying temperature $T_s(r)$ as

$$T = T_s = 1.7\cdot 10^{10}\;\alpha^{2/9}\,m^{-10/9}\,\dot{m}^{8/9}\,\bar{r}^{\,-17/9}\,f^{8/9}\;\mathrm{K} \tag{3.112}$$

Which gives temperatures $T_s \sim 10^5 - 10^6\,\mathrm{K}$ for regions that are close to $r = r_{mo}$, and rising towards $T_s \sim 10^6 - 10^7\,\mathrm{K}$ for radii close to the inner region $r = r_{im}$. The modified blackbody temperature is thus higher than the corresponding blackbody temperature. Consequently, the photons emitted from this region have higher energy than if the disk radiated the same spectrum as a blackbody. This is reasonable since if the opacity is dominated by true absorption processes, then the emergent photons originate near and above the layer at which $\tau \simeq 1$. Thus the characteristic photon spectral color temperature will be comparable to the blackbody temperature. If the opacity is dominated by scattering the emerging photons will originate deeper, at say $\tau \equiv \tau_s \gg 1$. Following emission far below the surface at large optical depth τ_s, photons undergo many scatterings prior to emerging. If the scattering is elastic then the photons will emerge with a color temperature comparable to the matter temperature at the point of generation. Thus elastic scattering tends to increase the characteristic energy of emerging photons, and we have a harder spectrum than in the outer absorption dominated region.

In the same way as for the outer region we can estimate the total radius-integrated observed spectrum as

$$S_{\nu,middle} = A\int_{r_{im}}^{r_{mo}} F_{\nu,middle}[T_s(r)]\,2\pi r\,dr \tag{3.113}$$

If we want to evaluate the integral we will need both ρ and T_s as functions of r, and this can be taken from (3.72). We can put $T \propto r^{-p}$ and $\rho \propto r^{-q}$. If we do this and perform the calculation of (3.113) we get

$$S_\nu \propto \nu^{(q-6)/4p+5/4} \int_{x_{im}}^{x_{mo}} \left(\frac{e^{-x}}{e^x - 1}\right)^{1/2} x^{(2-2p-qp)/2p^2+1/4}\, dx \tag{3.114}$$

where $x_{im} = h\nu/kT_{im}$ and $x_{mo} = h\nu/kT_{mo}$. Again, from (3.71) we get $p = 9/10$ and $q = 33/20$, and we see that

$$S_{\nu,middle} \propto \nu^{0.05} \tag{3.115}$$

Rounding up, we can put the total luminosity from this part of the disk L_{middle} as

$$L_{middle} = \int_0^\infty S_{\nu,middle}\, d\nu \tag{3.116}$$

3.5.3 Inner Region

In the inner part of the disk, where radiation pressure dominates gas pressure and we assume that there are no outer magnetic fields to disrupt the disk structure, the electron temperature becomes sufficiently high that the process of Comptonization and free-free emission strongly affects the shape of the emitted spectrum. Comptonization is the mechanism by which photons can exchange energy with electrons, I refer to Appendix A again. The realm of Comptonization is given by the y-parameter

$$y = \frac{4kT}{m_e c^2} \mathrm{Max}\,(\tau_{es}, \tau_{es}^2) \tag{3.117}$$

for the non-relativistic case [39]. When $y > 1$, Comptonization becomes important, and we get a Wien spectrum

$$I_\nu = \frac{2h\nu^3}{c^2}\, {}^{-h\nu/kT} \tag{3.118}$$

The frequency ν_{Com} above which Comptonization becomes important is found by putting $y = 1$

$$\frac{h\nu_{Com}}{kT} = 2.4 \cdot 10^{17}\, \rho^{1/2}\, T^{-9/4} \tag{3.119}$$

which for the parameters expected at these radii $\rho \sim 10^3\,\mathrm{kg\,m^{-3}}$ and $T_c \sim 10^8 - 10^9\,\mathrm{K}$ (from (3.71)) yield $\nu_{Com} \simeq 5 \cdot 10^{17} s^{-1}$. We see from the results earlier in this chapter that the disk shows tendencies to become optically thin in the inner regions. This will generally harden the X-ray spectrum from the inner parts, but not sufficiently to produce the observed spectrum in some of the luminous X-ray binaries observed. To fix this, and some of the stability problems that are encountered in the inner parts of standard disk models, alternative disk models have been constructed.

In order to see what the total spectrum for the disk looks like, we can plot the results from the last sections. We gather that in the range $\nu < \nu_{bb}^{lower}$ we get a spectrum characterized by Rayleigh-Jeans law $S_\nu = (2kT/c^2)\,\nu^2 \propto \nu^2$. We have seen that for the blackbody spectrum (3.100) we can put $p = 3/4$. And we therefore have $S_\nu \propto \nu^{1/3}$ for $\nu_{bb}^{lower} < \nu < \nu_{bb}^{upper}$. For the modified spectrum (3.114) we can put $p = 9/10$ and $q = 33/20$, so that we have $S_\nu \propto \nu^{0.05} \sim \nu^0$ for $\nu_{bb}^{upper} < \nu < \nu_{Com}$. Finally for $\nu > \nu_{Com}$ we have the Wien cut-off spectrum (3.118). In Fig. 3.13 we see this spectrum plotted.

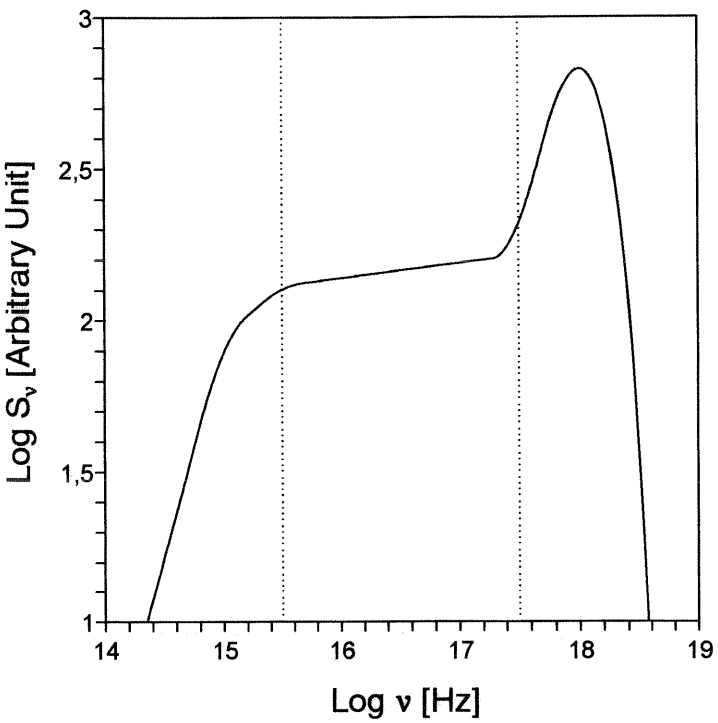

Fig. 3.13 *The spectrum of a standard thin disk, consisting of a Rayleigh-Jeans law for low frequencies, a blackbody and modified blackbody for intermediate frequencies and a Wien cut-off spectrum for the highest frequencies. This plot is for* $\alpha = m = \dot{m} = 1$.

From the spectrum we can see how little fraction of the total luminosity that actually originates from the outer parts $\nu < 10^{16} - 10^{17}\,\mathrm{s}^{-1}$. To evaluate the contribution to the luminosity from the different regions, we can either integrate the expressions (3.98), (3.111) and (3.118), or make a numerical estimate based on Fig. 3.13. It is clear from earlier discussions (in Chapter 2) that in the case of a neutron star or white dwarf we have

$$\frac{L_{acc}}{2} = \frac{L_{disk} + L_{surface}}{2} = L_{disk} = L_{surface} \tag{3.120}$$

where $L_{surface}$ is the luminosity generated by the interaction with the accretion gas flow with the surface or boundary layers (including magnetic fields), and L_{disk} is the lumi-

nosity from the disk itself. From a numerical estimate we get for the disk luminosity approximately

$$\begin{aligned} L_{inner} &= 93.5\%\, L_{disk} \\ L_{middle} &= 6.45\%\, L_{disk} \\ L_{outer} &= 0.05\%\, L_{disk} \end{aligned} \tag{3.121}$$

3.5.4 Irradiated Disks

As we have seen earlier, the shape of a thin standard disk is concave (saucer-shaped). It is therefore possible for radiation emitted in the central parts of the disk (or from the compact object itself) to hit the outer or middle parts, even if it moves in a straight line. When relativistic gravitational effects are taken into consideration it is even possible for the radiation to be bent in the gravitational field, and to be reabsorbed by the disk in this way. This reprocessing effect is usually called *irradiation* of accretion disks. The irradiation of the accretion disk by the compact object, boundary layer, donor star or the disk itself, has been extensively studied. Generally, irradiation becomes important in the outer regions of accretion disks, where it may even in some cases dominate the viscous heating [40]. If the donor star is a late spectral type O or B, the radiation (and to some degree also the stellar wind) from such stars may be substantial, and can therefore be of relevance to the energetics of the outer region of an accretion disk.

X-ray Bursts

In the case that the compact object is a neutron star, there may be very powerful high energy phenomena taking place on the surface or boundary layers (including magnetic fields) of this object. I will not go into all of these now, but only mention one interesting phenomena called *X-ray bursts*. A subset of the so-called galactic bulge X-ray sources show periodic and dramatic increases in their X-ray intensity, lasting some tens of seconds and recurring at intervals of some hours or days. With some exceptions the X-ray bursts are believed to be flashes of energy liberated in runaway thermonuclear explosions in material accreted onto the surface of neutron stars. It is (at least for me) a novel and startling concept to interpret these bursts as a sequence of nuclear explosions. The evidence, both observational and theoretical, is nevertheless very strong. The observed spectrum fits well into a thermonuclear explosion scenario, and the total energy together with the temperature obtained from the spectrum, gives a measure of the area of the source, which is found to have a dimension of $\sim 5\,\mathrm{km}$. If we assume that it is relatively evenly spread (which is a good assumption given the enormous gravitational forces at hand), the accreted material is probably no more than $\sim 1\,\mathrm{m}$ thick. Several models exist, but if one adopts information from thermonuclear weapons models, it appears that since

there are restraints on thermonuclear burning of hydrogen, the main origin to these X-ray bursts is therefore probably fusion in helium (or deuterium). The observed energetics gives $\sim 10^{18}$ kg accreted for each flash, which means that $\sim 10^{32}$ J is released $= 10^{15}$ Castle-Bravo detonations.

3.6 Stability

Instability in this sense means a substantial continuous and growing deviation from a steady disk structure. Any temporary change in the disk parameters that eventually (after some time) causes the disk to again settle down into a steady state (not necessarily the same) are not considered as instabilities. The list of phenomena that can cause instabilities in plasmas is (in many ways sadly) very voluminous.

Suppose that a small perturbation is made to an equilibrium solution, and that this perturbation for some reason continues to grow, rather than at one point being damped. Then this *steady* solution is said to be unstable and cannot exist indefinitely in nature. In for instance a protoplanetary disk, instabilities in the dust-disk probably cause the formation of planets. But if this clumping of matter were to continue, another star would be formed instead of a planet system, even though both might to some degree be considered steady endpoints.

Viscous & Thermal Instabilities

There are different types of instabilities in accretion disks, and they may be categorized according to the timescales under which they operate. If for example the energy balance is disturbed, any instability will grow on a timescale of the order $\sim t_{th}$, which we have shown is much smaller then t_{visc}. Since t_{visc} is the timescale for significant changes in the surface density Σ, we can assume that Σ is fixed during the growth time t_{th}. We have also developed that $t_{th} > t_\phi > t_z$ so the vertical structure of the disk can respond rapidly, on a timescale t_z, to changes due to the thermal instability, and keep the vertical structure close to hydrostatic equilibrium. We can thus assume that during thermal instabilities we have Σ and H constant, and that the thermal balance is achieved instantly during viscous instabilities.

Miscellaneous Instabilities

In addition to these two well established instabilities (which are relevant to most disk models), there are also other miscellaneous mechanisms that may be considered. We have up to this point assumed that we have an axisymmetric potensial well, and therefore postulated an axisymmetric disk structure. This assumption is reasonable for most parts of the disk. However, the assumption can break down in the outermost parts of the disk,

where the tidal effects of the companion donor star might be substantial. These forces lead to tidal torques, much like the tidal forces in the Earth-Moon system cause tidal bulges on the two bodies. On basis of this, disks that are eccentric and exhibit precession movement, can be constructed. This tidal torque may however cause instabilities in the disk structure, called *tidal instabilities*. I shall not dwell into these (for us somewhat peripheral subjects), other than to say that these tidal instabilities are usually invoked (successfully, it appears) as explanation for outburst-phenomena (superhumps) that seems to be observed in certain classes of dwarf novae [30]. It is also believed that these tidal forces play an essential role in the removal of disk matter from the outer rim of accretion disks, and for feeding it back into the binary.

Magnetic Instabilities

Many instabilities in the accretion flow have been identified positively to be *magnetic instabilities*. These include most prominently the magnetic buoyancy-driven interchange and Parker instabilities, but also the before mentioned magneto-rotational instability. As is the case with instabilities, there are also a plethora of oscillations and waves that can occur in a plasma, and many of these are of an acoustic or magnetic nature (or both). Some of these oscillations can cause instabilities in the disk flow. In stars, this extensive field of study is called helioseismology, and in the case of accretion disks *diskoseismology*.

3.6.1 Viscous Instabilities

Suppose that the surface density in a steady disk is perturbed axisymmetrically at each r, so that

$$\Sigma = \Sigma_0 + \Delta\Sigma \tag{3.122}$$

where Σ_0 is the steady-state distribution. Putting $\mu = \nu\Sigma$ there will be a corresponding perturbation $\Delta\mu$. We also have $\mu = \mu(r, \Sigma)$, so that $\Delta\mu = (\partial\mu/\partial\Sigma)\Delta\Sigma$. We remember that $\Delta\Sigma$ and $\Delta\mu$ are related from (3.23), and eliminating $\Delta\Sigma$ we get for the growth of the perturbation

$$\frac{\partial}{\partial t}(\Delta\mu) = \frac{\partial\mu}{\partial\Sigma}\frac{3}{r}\frac{\partial}{\partial r}\left[r^{1/2}\frac{\partial}{\partial r}\left(r^{1/2}\Delta\mu\right)\right] \tag{3.123}$$

Not surprisingly, $\Delta\mu$ obeys a diffusion equation, but the interesting thing is that the diffusion coefficient is proportional to $\partial\mu/\partial\Sigma$ and in principle can be either positive or negative. If $\partial\mu/\partial\Sigma > 0$ you get a behavior where the perturbation decays on a viscous timescale, and therefore a stable disk. If however $\partial\mu/\partial\Sigma < 0$, more material will be fed into those regions of the disk that are denser than their surroundings and material will be removed from those regions that are less dense, so that the disk will tend to break up

into rings. This breakup on a timescale t_{visc} constitutes a viscous instability, and shows that steady disk flow is possible only when $\partial\mu/\partial\Sigma > 0$.

Since $\mu = \nu\Sigma \propto \dot{M}$ we may write the stability requirement as

$$\left(\frac{\partial \dot{M}}{\partial \Sigma}\right)_{Q^-_{rad}=Q^+_{visc}} > 0 \tag{3.124}$$

An increase in $\dot{M}$ must be followed by an increase in Σ, or there is an instability. In the middle region, where the opacity comes from electron scattering, and the gas pressure dominates, the diffusion coefficient in the diffusion equation (3.123) is positive, which is not the case for $p_{rad} \gg p_{gas}$. This means that the middle region (and the outer) is viscously stable, while the inner radiation pressure dominated region is not.

A very useful tool in the stability analysis of disks are $\dot{M}\Sigma$-plots (or $T\Sigma$-plots for thermal instabilities). If an equilibrium disk (or rather a sequence of equilibrium disks) are plotted in the $\dot{M}\Sigma$-plane, we can study which of these equilibrium states are stable and which are not. By equilibrium plots, this would mean plots along which $Q^-_{rad} = Q^+_{visc}$ in this case. All disk curves in the $\dot{M}\Sigma$-plane that are decreasing are unstable, while increasing curves for which $\partial\dot{M}/\partial\Sigma > 0$ are stable.

3.6.2 Thermal Instabilities

Such instabilities arise when the local volume cooling rate Q^-_{rad} within the disk can no longer cope with volume heating rate Q^+_{visc} due to viscous dissipation, since we must have $Q^-_{rad} = Q^+_{visc}$ in equilibrium. If the temperature T_c is raised by a small value ΔT_c, both the cooling rate and the heating rate will increase. If however the Q^+_{visc} increases faster than Q^-_{rad}, then T_c will rise further because the cooling rate is inadequate, and we have a runaway temperature increase (or thermal instability). In other words, a steady state is impossible in a parameter regime where the instability would grow in such a fashion, despite the fact that a formal equilibrium solution can be found. Though the nature of the thermal instability is basically the same, several mechanisms may cause such a deviation. Several models that include alternative energy transfer modes, such as convection or conduction, seem to give rise to thermal instabilities in certain parts of the disk.

Since Σ is constant, we can take $p \propto H$. Let us first consider the inner region where $p \simeq p_{rad}$ and $\bar{\kappa} \sim \kappa_{es}$. The heating per unit surface Q^+_{visc} is proportional to ρH, and thus $Q^+_{visc} \propto H^2$. The cooling rate per unit surface Q^-_{rad} however is proportional to H, or $Q^-_{rad} \propto H$. In the unperturbed state, Q^+_{visc} and Q^-_{rad} are balanced. However, if for

example the disk temperature increases slightly over that of the equilibrium state, the disk will expand in the vertical direction (much like a star would expand radially if it's temperature increased), since $H \propto p \propto T^4$. Then both, Q^+_{visc} and Q^-_{rad} increase, but the increase of heating overcomes that of cooling. This means that the specific entropy of the gas increases, which leads to an increase of H, since the entropy s is $8\sigma T^3/3\rho c$ and increases with H as $s \propto H^{7/4}$. In this way, the increase of H is fed back positively to the increase of H, and the disk is unstable. It is possible that this thermal instability leads to inner regions where the thin disk approximation breaks down, and the central disk region may therefore very well resemble a bloated or thick disk.

We look at the middle region where the gas pressure dominates over the radiation pressure, and we have $\bar{\kappa} \sim \kappa_{es}$ and $p \sim p_{gas}$. In this case, the rate of viscous heating is the same as before: $Q^+_{visc} \propto H^2$. The rate of radiative cooling is however changed since $p_{rad} \propto T^4 \propto (p/\rho)^4 \propto (pH)^4 \propto H^8$. This means that in the gas-pressure dominated region the disk is thermally stable. A generalization to the case where both the cooling rate Q^-_{rad} and heating rate Q^+_{visc} are arbitrary functions of ρ and T, is also straightforward [37]

Based on the above, a general criterion concerning the thermal instability of disks can be expressed as [36]

$$\left[\frac{\partial}{\partial H}(Q^+_{visc} - Q^-_{rad})\right]_\Sigma > 0 \tag{3.125}$$

The thermal instability is examined under the condition that Σ is constant, and $p \sim H$. Hence we can easily see that increases (or decreases) in H and T are in the same direction (either both negative or both positive), and thus an alternative thermal stability condition would be

$$\left(\frac{\partial Q^+_{visc}}{\partial T}\right)_\Sigma < \left(\frac{\partial Q^-_{rad}}{\partial T}\right)_\Sigma \tag{3.126}$$

In the before mentioned ADAF disks this thermal instability analysis becomes somewhat different. Because viscously generated energy is transported inwards with the gas flow (and is not radiated right away) this leads to a relaxation in the energy equilibrium corresponding to the term Q^-_{adv}. The radial advection of energy thus leads to a more efficient cooling of the gas per radius, since some of the energy which would be stored in the gas and therefore lead to runaway heating, is advected into smaller radii. We thus have instead the equilibrium condition

$$Q^+_{visc} = Q^-_{rad} + Q^-_{adv} \tag{3.127}$$

This will inevitably lead to a much hotter inner region since this energy has to end up somewhere. Due to this, most ADAF disks have much hotter inner regions than the traditional Shakura-Sunyaev disks, and the ADAF disks are therefore better suited to reproducing the hard radiation produced and observed from systems with such inner regions.

In Fig. 3.14 we see a plot of the heating function Q^+_{visc} and the cooling function Q^-_{rad} as functions of temperature T for our thin disk model

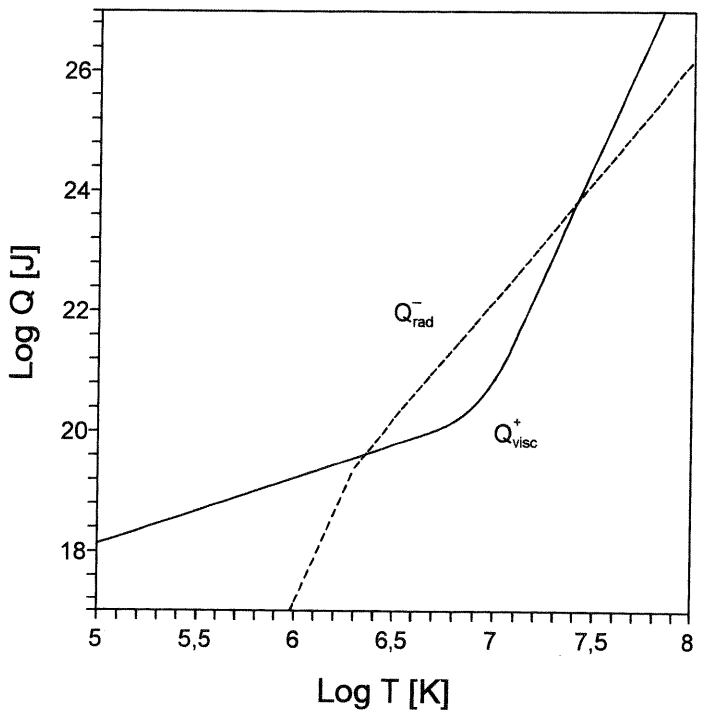

Fig. 3.14 *The heating function Q^+_{visc} and cooling function Q^-_{rad} as functions of temperature T for a fixed $\Sigma = 1.3 \cdot 10^5\, kg\, m^{-2}$, and $\bar{r} = 10$, $m = \dot{m} = \alpha = 1$.*

We see these functions for the parameters $\bar{r} = 10$, $m = \dot{m} = \alpha = 1$, and $\Sigma = 1.3 \cdot 10^5\,\mathrm{kg\,m^{-2}}$. For the low temperature region where $p = p_{gas}$ and $\bar{\kappa} = \kappa_{ff}$ we have

$$Q^+_{visc} = \frac{9}{4}\nu\Sigma\Omega_K^2 \sim T\Sigma \qquad Q^-_{rad} = \frac{8\sigma T^4}{3\tau} \sim \frac{T^8}{\Sigma^2} \tag{3.128}$$

while for the high temperature ($p = p_{rad}$ and $\bar{\kappa} = \kappa_{es}$) we get

$$Q^+_{visc} \sim \frac{T^8}{\Sigma} \qquad Q^-_{rad} \sim \frac{T^4}{\Sigma} \tag{3.129}$$

We can see that there are two possible equilibrium solutions. In the low temperature region we have a stable disk solution, because (3.126) is fulfilled in the vicinity. The other

equilibrium solution in the high temperature regime is clearly non-stable, as the heating function Q^+_{visc} is rising more steeply than the cooling function Q^-_{rad} for those T.

3.7 Alternative Disk Models

As I said earlier there are problems with the standard model of accretion disks. These problems are connected to the inner radiation pressure dominated region. It has been demonstrated that this inner region is viscously unstable, and we have seen that the hard X/γ-ray spectrum ($\sim 100\,\mathrm{keV}$) is not easily reproduced due to the fact that most of the disk (also most parts of the inner region) is optically thick.

Optically Thin Disks

It was originally suggested, that if the inner region of an accretion disk is optically thin and at high temperature ($\gtrsim 10^9\,\mathrm{K}$), instead of optically thick and low temperature ($\lesssim 10^8\,\mathrm{K}$), then the observed X-ray spectrum of the most luminous sources can be explained. Such an optically thin, hot model was constructed by Shapiro, Lightman and Eardley in 1976 [42]. In this and many other optically thin models, the thin disk assumption is relaxed to the condition

$$H \lesssim r \tag{3.130}$$

so that height-averaged basic equations can still be employed. Disks that employ this relaxed thin disk formulation are sometimes referred to as *slim disks*. The gas is optically thin to absorption ($\tau_* \ll 1$), hence the dominant pressure source is gas pressure ($p_{rad} \ll p_{gas}$) even for the inner region. Another feature that is invoked in this model is that due to inefficient coupling (only through Coulomb-forces) between ions and electrons, the ion and electron temperature may differ from each other ($T_i \neq T_e$). This *two temperature model* is carried on in many later models. In many such models the ion temperature and the electron temperature may differ by many orders of magnitude, due to much more efficient cooling processes for the electrons at these temperatures. Typically one may obtain for the very inner regions of luminous disks $T_i \sim 10^{11}\,\mathrm{K}$ and $T_e \sim 10^9\,\mathrm{K}$. These ion temperatures are probably the highest temperatures of any macroscopic gas known today, it is perhaps only equalled by matter temperatures at the centers of neutron stars, or by conditions inside a supernova.

Relativistic Disks

Several relativistic disk models have been attempted. A full relativistic consistent model (involving both gravity and dynamics) has however yet to be constructed, and given the complexity in many aspects of non-relativistic models, this is not surprising. A common

approach to this problem is the use of psuedo-Newtonian potentials and approximations, which seems to work well in most cases. The relativistic models are however mostly applicable to black hole accretion systems, where the Keplerian speeds v_ϕ can reach magnitudes comparable to c when the gas approaches the Schwarzschild-radius r_S. For most neutron star systems (and certainly for magnetized neutron stars, or pulsars) the gas never reaches the domain where such speeds are attainable, see Fig. 3.10 where v_ϕ is plotted as a function of $\bar{r}$. However, as we have discussed earlier, relativity is highly relevant when we consider the observed spectra from accretion disks, where the spectra may become modified when relativistic effects are taken into consideration. The very high speeds near r_S for black hole accretion causes another problem concerning the transonic nature of the gas flow there. Since the relativistic sound speed of the gas cannot exceed $c/\sqrt{3}$ [29], this means that at some point very close to the black hole the gas must cross from subsonic to transonic flow. The dynamics and topology at this radius must be dealt with in order to understand the accretion flow around r_S. This problem never arises in the disk around a neutron star, but must probably be taken into consideration when the gas falls onto the surface of the star and a shock front might develop (accretion columns).

ADAF

Another very central accretion disk model that has been developed in the 1990s is the so-called Advection Dominated Accretion Flows (ADAF). I have mentioned this approach several times earlier, but I will nevertheless give a short summary of the qualitative features of this model. Many of the essential assumptions that we made in our model is still with us in the ADAF-models, and both optically thin and optically thick ADAF-models can be constructed. These are the significant differences:

- Keplerian rotation is not assumed (the rotation is in fact usually sub-Keplerian). This means that the pressure force could become substantial in the radial force balance.
- Slow rotation in the sense of $v_r \ll v_\phi$ is not necessarily satisfied. It is only if the radial velocity is high enough that advective cooling is relevant, otherwise it is not. ADAF disk models therefore rely on higher v_r than standard disk models.
- As I have mentioned before, local energy balance $Q^+_{visc} = Q^-_{rad}$ is no longer valid.
- Like many other non-ADAF models the thin disk assumption is relaxed into a slim disk $H \lesssim r$.

The most important effect of advection on disk structures is advective heat transport, which is neglected in standard models. In the standard disks it is assumed that the heat generated by viscous processes is radiated out at the same place where it is generated. In

a sense one might say that this advective heat transport has a cooling effect for a given radius compared with radiatively cooled standard disks, because heat Q^-_{adv} is transported away and $Q^+_{vis} \sim Q^-_{adv} \gg Q^-_{rad}$. A large portion of this heat is then dumped across the Schwarzschild-radius of the black hole and leaves the system permanently. It can be shown [44] that in these radiation pressure-dominated slim disk models, the advective cooling rate per unit surface Q_{adv} satisfies

$$Q_{adv} \geq \left(\frac{H}{r}\right)^2 Q^+_{visc} \tag{3.131}$$

where Q_{visc} is the usual viscous heating rate per unit area. This shows that advective cooling (at least in the radiation pressure-dominated regions) depends on a large value of H/r, i.e. a slim disk.

We should also mention that the disks in which the effects of advection are non-negligible have stability properties that are rather distinct and more satisfying than that from standard disks, which was a part of the reason why ADAF-models were constructed to begin with.

The Ambiguousness of Accretion Disk Modeling

Various disk models have been constructed and published that contain different assumptions regarding almost all aspects of accretion disks. These models include differing viscosity prescriptions, equations of state where a magnetic pressure-term is added, and a whole variety of models with differing energy transport and opacity schemes. Some have said that accretion disk modeling is, or has become, almost like an artform, where only the creativity sets the limit. This is of course an exaggeration, because all models must be based on underlying physical principles and have to be (at least to some degree) consistent, in that they do not contain any serious contradictions. In addition the models must fulfill several demands that make them physically feasible, such as for instance stability criteria. The underlying reasons for this plethora of accretion disk models, is that there isn't one correct way to construct accretion disks, there are many different prescriptions (for opacity, viscosity or others) that produce physically feasible accretion disks. When it comes to observations, one should realize that there is a zoo of various X-ray binary sources, with different characteristics, and an accretion disk model (with everything that goes into it) should therefore be tailor-made for each system, or at least for each class of system. I should add that sometimes our knowledge of the detailed physics involved are limited, or at least contain uncertainties that make the present ambiguousness in the accretion disk models possible.

Chapter 4

Disk Accretion Onto a Pulsar

4.1 Pulsars

As we have seen in Chapter 1, pulsars are considered to be very strongly magnetized neutron stars. A large volume of models and literature exists on the subject, so I will consider only the aspects of pulsar physics that we need here.

4.1.1 Spin Periods, Diameters and Masses

The masses of neutron stars in many binary systems can be determined remarkably well. Although current theory puts the maximum mass of neutron stars to $\sim 3\,M_\odot$, most of the determined masses appear to lie in a small range around $1.35\,M_\odot$ [48]. The currently favored equation of states leads us to expect a radius R very close to (but slightly above) 10 km, and the very large rotation speeds of some pulsars also limits the radius $R \lesssim 20\,\mathrm{km}$ (because the pulsar has to rotate below break-up speed). Until recently there have been no direct confirmed geometrical/optical way of measuring neutron star stellar radii, but it appears that precise observations made with NASA's Hubble telescope have uncovered (optically) the closest known neutron star known so far, RX J185635-3754 at a distance of ~ 200 ly in the southern constellation Corona Australis [49]. The star appears to move with a very high velocity $\sim 4 \cdot 10^5\,\mathrm{km\,s^{-1}}$ through space, and the estimated radius agrees with the above numbers.

Pulsars acquire their rapid rotation from angular momentum conservation during the stellar collapse in which they are created. Regular pulsars emit radio pulses at very precise intervals, the duration of the pulse itself is very short ($\sim 10^{-6}\,\mathrm{s}$). The interval between these pulses is interpreted as the spin period. The spin periods of the great body of pulsars range from a few milliseconds (the before mentioned millisecond pulsars) to several seconds. It is established that this spin period for an isolated pulsar generally increases with time, so the pulsar will spin down as it grows older. It is however, yet

uncertain as to what extent the magnetic field of an isolated radio pulsar decays as time progresses.

4.1.2 Magnetospheres

Their magnetic field strengths are consistent with the collapse of a normal star with a polar field $\sim 100\,\mathrm{G}$, the flux being conserved in the collapsing stellar material. A number of methods (more or less indirect) are used to estimate the strength of pulsar magnetic fields, such as synchrotron radiation, pulse period changes and several surface phenomena. Polar field strengths reaching $\sim 10^{12}\,\mathrm{G}$ occur in what is assumed to be young pulsars, while it may be as low as $\sim 10^{8}\,\mathrm{G}$ in others. Exotic neutron star objects called *magnetars* are assumed to have polar magnetic fields $\sim 10^{15}\,\mathrm{G}$, and are today generally and widely accepted.

Magnetic Dipole Model

In the *magnetic dipole* model for pulsar magnetic fields it is assumed that the neutron star rotates uniformly at a frequency $\Omega_\star$, and possesses a magnetic dipole moment $\boldsymbol{m}$ oriented at an angle α to the rotation axis. In the case of $\alpha \simeq 0$ this model is called an *aligned rotator*, as opposed to the *oblique rotators* where $\alpha \neq 0$.

Though the actual spin down I mentioned earlier is regarded as a fact, the mechanism by which pulsars convert their rotational energy into the observed radiation is still relatively poorly understood today. It is clear that there is a link between the electromagnetic radiation emitted by the pulsar (largely in the radio spectrum), the magnetic fields of the pulsar, and this loss of angular momentum. Most current theories for magnetospheric emission can be grouped into polar cap, outer gap or nebular models. These models, at least in some cases, need not be mutually exclusive, the Crab pulsar (and others) for example, shows clear evidence for pulsed emission from the magnetosphere and unpulsed emission from the surrounding nebula. The common thread between all magnetospheric models is that the radiated energy is derived from the spin-down of the neutron star. In almost all models, the radio emission is concentrated in a conical beam that corotates with the pulsar. In some of the models this radiation cone is aligned with the star's dipole magnetic field and the emission originates from the polar caps, this means that for pulses to appear we would need $\alpha \neq 0$. In other, so called magnetic dipole radiation models, the cone axis is perpendicular to the rotation axis of the star, and therefore pulses will be observed even for an aligned rotator.

We now, and in the following, concentrate our efforts on the aligned rotator ($\alpha \simeq 0$). We can put the magnetic moment $\mu = |\boldsymbol{m}| = B_0 R^3$, where B_0 is the polar surface magnetic

field strength (the point where the field has it's maximum intensity), and R is the neutron star radius. Most authors put the magnitude of μ for each pulsar to be

$$|\boldsymbol{B}| = B \simeq \frac{\mu}{r^3} = (10^{12}\,\mathrm{G})\,\mu_{30}\left(\frac{R}{r}\right)^3 \tag{4.1}$$

where $R \simeq 10$ km is assumed, and μ_{30} is in units of 10^{30} G cm^3.

This approximation is good in the equatorial plane (where the disk will be) and for sufficiently small r, but the deviation will be larger as the more complex polar field region is approached. The magnetic field $\boldsymbol{B} = \boldsymbol{B_p} + \boldsymbol{B_\phi}$ of such a neutron star will (in it's unperturbed state) be dominantly poloidal for most relevant radii. From the expression $B = \mu r^{-3}\sqrt{4 - 3\sin^2\theta}$ [52], this poloidal field $\boldsymbol{B_p}$ may be taken to have the dipole moments

$$B_r = \frac{3}{2}B_0R^3\frac{rz}{(r^2+z^2)^{5/2}} \tag{4.2}$$

$$B_z = -\frac{1}{2}B_0R^3\frac{r^2-2z^2}{(r^2+z^2)^{5/2}} \tag{4.3}$$

which gives (4.1) for $z = 0$. This field will interact with the disk in the equatorial plane, and by this interaction a toroidal field $B_\phi = |\boldsymbol{B_\phi}|$ will be generated, causing a magnetic torque.

It is generally assumed that the magnetic field of the pulsar is anchored to the star, and the rotation of the star will therefore sweep the magnetic field around with it. There will necessarily be a distance where the corotation velocity attains the speed of light. The speed at which the magnetic field energy travels in space cannot exceed the speed of light, and therefore there will be an imaginary cylinder with an axis along the pulsar rotation axis and with a radius $r = c/\Omega_\star$ called the *light cylinder* where the magnetic dipole model is valid. Magnetic field lines that pass through this cylinder are open and also form toroidal components, thus invalidating (4.2) and (4.3). For most pulsar spin rates $\Omega_\star$ the light cylinder will be well outside the disk/magnetosphere interaction region, and the dipole field (4.1) is applicable. For very fast spinning pulsars (in the millisecond region) the light cylinder might however start at quite small radii (close to the pulsar) and therefore complicate the assumed relevant unperturbed magnetic field considerably.

Magnetosphere

The standard theory of the electrodynamics of pulsar magnetospheres is still largely according to a monumental paper by Goldreich and Julian in 1969 [50]. The rotation of a neutron star possessing a magnetic field induces powerful electric fields satisfying

$$\boldsymbol{E} + \frac{(\boldsymbol{\Omega}_\star \times \boldsymbol{r})}{c} \times \boldsymbol{B} = \boldsymbol{0} \qquad \boldsymbol{E} \cdot \boldsymbol{B} = \boldsymbol{0} \tag{4.4}$$

in the space surrounding the star. Because of these electric fields, the surrounding region cannot be empty but must contain a charge density, consequently the pulsar will possess a dense magnetosphere. The electric field will impart a force on both electrons and ions that exceeds the gravitational force by $\sim 1 : 10^9$ for protons, and even higher for electrons [10]. Thus particles will be torn off the surface and create a region of rotating plasma around the pulsar. It is estimated that these electric fields give rise to electric potential differences of the order $\sim 10^{13}$ V [55]. It is clear though that this current generated at the pulsar surface (Goldreich-Julian current), will modify the electric field driving the current, and thereby also the magnetic field which in turn generated the electric field [51]. The general problem concerning the electrodynamics of the pulsar magnetosphere is complicated and as yet unresolved.

In the Goldreich-Julian theory the magnetosphere is in a so-called *force-free* state. The currents in this force-free state is not zero, but the magnetic force is zero because the current density is everywhere parallel to the magnetic field. Thus $\boldsymbol{J} \times \boldsymbol{B}$ vanishes even though $\boldsymbol{J}$ and $\boldsymbol{B}$ are finite, and the magnetosphere is highly conducting along, but not perpendicular to the magnetic field lines [50]. Inside the light cylinder, the plasma will corotate with the star because of the strong magnetic field, and matter will be able to flow freely along magnetic field lines. In the region where the field lines are open, flowing particles are permanently lost to the pulsar.

This theory is proper for the magnetosphere of an isolated pulsar with a rotating magnetic field, but with no accretion disk. An accretion disk plasma with an azimuthal velocity inside this rotating magnetic field will introduce additional fields and phenomena, including a radial electric field.

4.2 Disk-Magnetosphere Interaction

As mentioned before, in the absence of a disk the magnetic field lines are poloidal, and near the equator plane dominated by the B_z component. When a disk is introduced, the central assumption in many models is that the magnetic field becomes threaded to the disk, or that the magnetic field lines are frozen to the orbiting plasma (I refer to Appendix C for details). Since the field is forced to follow the fluid elements it is sheared in the ϕ-direction. This shearing generates a sizable toroidal B_ϕ component in the disk. As long as the field lines remain continuous across the disk, B_ϕ must be equal in magnitude, but opposite in direction above and below the disk plane. As a result, the magnetic field in

the disk will vary much more rapidly with z than with r, it goes from $+B_\phi$ to $-B_\phi$ as z goes from $-H$ to H (and $H \ll r$). In Fig. 4.1 we see this clearly demonstrated, and we also observe that

$$B_\phi^+ = B_\phi(r, H) = -B_\phi^- = B_\phi(r, -H) \tag{4.5}$$

and that $B_\phi(r, 0) = 0$. Thus there is a torque from the upper half (or surface area) of the disk, and since B_ϕ changes sign in the lower half, there is also an equal contribution from this part.

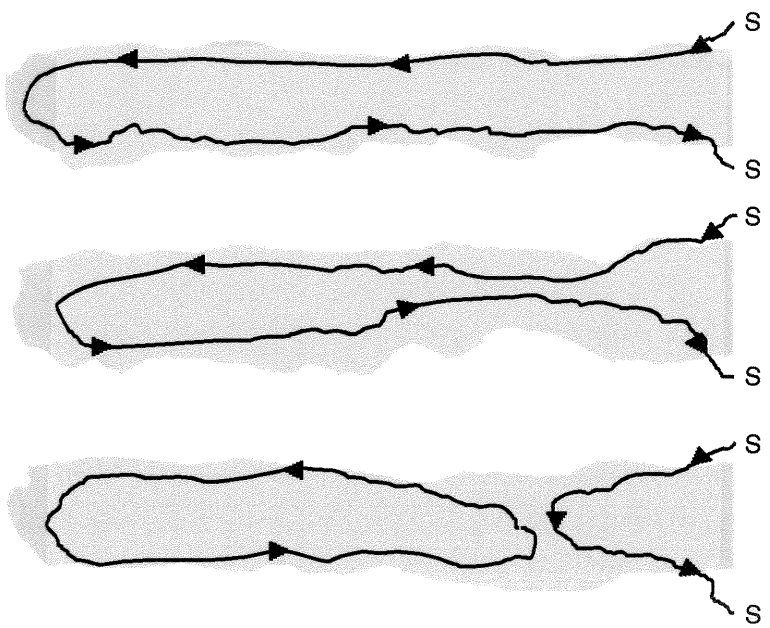

Fig. 4.1 *The shearing of magnetic field lines by threading onto the disk. In the bottom image, a typical example of magnetic reconnection is visualized, and the S signifies that the field line is connected to the stellar surface.*

The matter in the neutron star and the disk has a relatively high electrical conductivity. Therefore as matter moves in directions perpendicular to the magnetic field, it creates a $\boldsymbol{v} \times \boldsymbol{B}$ polarization electric field. If there is sufficient plasma between the star an the disk, the electric potential difference can drive appreciable magnetospheric electrical currents around the system. The resulting $\boldsymbol{J} \times \boldsymbol{B}$ forces act on the matter in the star, the magnetosphere and the disk to reduce their relative motion. The character of this electrodynamic interaction depends on the distribution of electrical resistance along the current paths. Most investigations indicate that the conductivity is likely to be high along field lines, at least in the magnetosphere [52][55]. One therefore arrives at a system

of field-aligned currents that is not unlike the polar-cap ionospheric current system that is thought to operate around Jupiter. Charged particles are then magnetically trapped and begin to corotate with Jupiter, producing ovals of auroral light centered on Jupiters magnetic poles.

The inward radial velocity v_r of the disk also generates important effects. The radial inward motion of the plasma across the poloidal component of the magnetic field within the disk, generates a toroidal electric field that drives toroidal currents J_ϕ. These currents set up a magnetic field that screens the disk from the stellar poloidal magnetic field (they are sometimes called screening-currents). Another effect produced by these currents is that they pinch the stellar magnetic field inwards, thus creating a inward radial component B_r even in the equatorial plane.

4.2.1 Magnetic Coupling

There are a variety of processes that causes the magnetic field to invade and mix with the disk plasma in a time which is short compared to the radial drift time.

- **Turbulent diffusion**
  The disk and the star will also be coupled by turbulent diffusion of the magnetospheric field into the disk. This is shown in the two upper images of Fig. 4.1. This process is important in the region where the kinetic energy density of convective of turbulent motions in the disk exceeds the energy density of the magnetospheric magnetic field just outside the disk. In this region one expects the magnetospheric field to be entrained by the convective motions, and carried into the disk. The turbulent diffusion timescale have been estimated to $\sim 10^{-3}$ the radial drift time [57].

- **Kelvin-Helmholtz instabilities**
  Kelvin-Helmholtz instability can occur when there is sufficient velocity difference across the interface between two fluids. The velocity discontinuity between the low density magnetic field region and the disk drives a Kelvin-Helmholtz instability. Penetration of the Keplerian flow by the magnetospheric magnetic field is assured if unstable modes grow to an amplitude comparable to the semi-thickness H of the disk. The growth times of the Kelvin-Helmholtz modes can be estimated analytically in the linear regime, and estimates show that they are of the order $\sim 10^{-5}$ times the radial drift time [53]. Thus there appears to be enough time for these modes to grow to sufficiently large amplitudes to greatly disturb the disk surface, and allow the magnetospheric magnetic field to mix with the disk before the plasma drifts significantly inward.

- **Magnetic reconnection**
  A third process that couples the disk and the star is reconnection of the magnetospheric magnetic field to magnetic fields in the disk. This is shown in the bottom image of Fig. 4.1. This process also creates magnetic flux loops, called magnetic islands inside the disk. The timescale here is of the order $\sim 10^{-4}$ times the radial drift time [58].

As a result of these mechanisms the field will thread the disk well beyond the inner edge.

4.2.2 Diffusion of B_ϕ

It is clear that if the magnetic shearing, twisting and stretching of a magnetic field line is allowed to continue indefinitely without any decay of the B_ϕ-field, a steady equilibrium disk flow is impossible. It is therefore essential to this model that there are ways for the azimuthal field to diffuse. We have seen (Appendix C) that for a magnetic field to be perfectly threaded onto a plasma we need the electrical conductivity $\sigma = 1/\mu_0\eta$ to be infinite, and conversely the magnetic diffusion $\eta = 0$. In a real disk the electrical conductivity must (and will) be large, but not infinite, and therefore we will always have a resistivity, or a finite magnetic diffusion η. One can introduce an effective electrical conductivity σ_{eff} for the plasma, and deduce the value it must have, based on the condition of steady flow. Then one might say that the sum of dissipative processes that leads to steady flow must give this effective conductivity σ_{eff}. For a steady disk flow there must be a balance between the amplification and dissipation of the azimuthal B_ϕ-field. If $(\partial B_\phi/\partial t)_+$ is assumed to be the generation rate of B_ϕ and $(\partial B_\phi/\partial t)_-$ is the diffusion rate, then

$$\left(\frac{\partial B_\phi}{\partial t}\right)_+ + \left(\frac{\partial B_\phi}{\partial t}\right)_- = 0 \tag{4.6}$$

There are basically three processes which contribute to the diffusion of B_ϕ. Two of them have already been mentioned above, namely turbulent diffusion and magnetic reconnection. While these two mechanisms contribute to the coupling of the field with the plasma, they also lead to diffusion of the magnetic field. Another process that contribute to η in such a disk is *magnetic buoyancy* (also known as Parker instability). The presence of a magnetic field can make a portion (a horizontal flux tube) of a compressible fluid less dense than its surroundings. If an approximately isothermal medium is assumed, then the thermal pressure inside the flux tube will differ from that outside. If horizontal force balance is assumed across $\boldsymbol{B}$, then the tube will experience a buoyancy force, and so it will drift under the influence of a vertical gravity, thus leading to a diffusion of the field.

In a manner analogous to the stretching of field lines in the azimuthal direction, the inward radial drift of the disk plasma pinches the stellar field inward in the disk plane, thereby generating a radial magnetic field component B_r from the z-component B_z. Again the actual value of B_r is determined by a balance between amplification and dissipative processes.

4.2.3 The Poloidal Fields B_r and B_z

We have now looked at the generation and diffusion of the B_ϕ-field in the disk. The poloidal stellar field in the equatorial plane will also be perturbed and modified by the disk motion. We now need the the poloidal components of the induction equation (C.6), this is

$$v_r B_z - v_z B_r + \mu_0 \eta J_\phi = 0 \tag{4.7}$$

This equation shows that the inflow $\boldsymbol{v}_p$ across $\boldsymbol{B}_p$ generates the toroidal current density J_ϕ. If $\boldsymbol{v}_p$ were effectively vanishingly small then (for finite η) it follows that $J_\phi = 0$, and the stellar poloidal field would penetrate the disk unmodified. The finite inflow through the disk perturbs $\boldsymbol{B}_p$, giving from (4.7)

$$v_r B_z - v_z B_r + v_r B_z' - v_z B_r' = -\mu_0 \eta J_\phi' \tag{4.8}$$

where B_r and B_z are given by (4.2) and (4.3), and primes denote perturbations. Since $\boldsymbol{\nabla} \boldsymbol{B}_p' = 0$ for an axisymmetric field, it follows that the components of $\boldsymbol{B}_p'$ can be expressed in terms of an azimuthal vector potential $A' \hat{\boldsymbol{\phi}}$ as

$$B_r' = \frac{\partial A'}{\partial z} \qquad B_z' = \frac{1}{r}\frac{\partial}{\partial r}(rA') \tag{4.9}$$

The corresponding toroidal current density is

$$J_\phi' = \frac{1}{\mu_0}\left(\frac{\partial B_r'}{\partial z} - \frac{\partial B_z'}{\partial r}\right) \tag{4.10}$$

and hence is related to A' by

$$\nabla^2 A' - \frac{A'}{r^2} = -\mu_0 J_\phi' \tag{4.11}$$

Large distortions of $\boldsymbol{B}_p$ require poloidal flows having a kinetic energy density at least comparable to the poloidal magnetic energy density, that is $\rho v_p^2 \gtrsim B_p^2/\mu_0$. In the inner regions, where the stellar magnetic field is strongest, poloidal flows in the low density magnetosphere will not have sufficient ρv_p^2 to cause large $\boldsymbol{B}_p'$. Hence, in these regions, any

large distortion of $\boldsymbol{B}_p$ would have to be caused by the disk inflow. For small poloidal flows in the magnetosphere above and below an undisrupted disk, the toroidal current density J'_ϕ will be concentrated in the disk. $|\boldsymbol{B}'_p|$ in the disk can be investigated using (4.8). Since the unperturbed stellar field is largely vertical for $|z| \leq H$, the relevant quantity here is $|B'_z|/|B_z|$. It follows from (4.9) and (4.11) that $\boldsymbol{B}'_p$ has the vertical length scale of A' and J'_ϕ, which is H, and hence in the disk (4.10) becomes

$$J'_\phi = \frac{1}{\mu_0}\frac{\partial B'_r}{\partial z} \tag{4.12}$$

since $H/r \ll 1$. If we consider terms on the left hand side of (4.8), then the continuity equation $\boldsymbol{\nabla}(\rho \boldsymbol{v}) = 0$, or

$$\frac{1}{r}\frac{\partial}{\partial r}(r\rho v_r) + \frac{\partial}{\partial z}(\rho v_z) = 0 \tag{4.13}$$

gives

$$|v_z| \sim (H/r)\,|v_r| \tag{4.14}$$

We observe that (4.2) and (4.3) yield (in the disk, or equatorial plane)

$$|B_r| \sim (H/r)\,|B_z|\,. \tag{4.15}$$

Hence

$$|v_r B_z| \sim (r/H)^2\,|v_z B_r| \tag{4.16}$$

so $v_z B_r$ is negligible. (4.9) and (4.14) show that $v_r B'_z$ and $v_z B'_r$ are comparable, so (4.8) becomes

$$v_r B_z + v_r B'_z - v_z B'_r = -\mu_0 \eta J'_\phi \tag{4.17}$$

For $|B'_z| \lesssim |B_z|$, equations (4.9), (4.12) and (4.17) give

$$\frac{|B'_z|}{|B_z|} \sim \frac{|v_r|}{(\eta/r)}\left(\frac{H}{r}\right)^2 \tag{4.18}$$

In the absence of a magnetic field viscosity causes the inflow, and we put the radial velocity due to viscosity $|v_{vr}| \sim \nu/r$, and so from (4.18) the condition $|B'_z| \ll |B_z|$ can be written

$$|v_r| \ll \frac{\eta}{\nu}\left(\frac{r}{H}\right)^2 |v_{vr}| \tag{4.19}$$

For $\eta \gtrsim \nu$, very large magnetically driven inflow speeds are needed to violate this condition. So the conclusion from all of this is that $|B'_z|$ will be a small perturbation, and can

be neglected compared to B_z. This is important, because it means that we can use the dipolar and unmodified field B_p in all calculations of torques etc.

4.3 Radii and Torques

As I said, we will continue to look at aligned rotators. For oblique rotators the rotation of the star causes the magnetic field to vary explicitly with time, which imposes an explicit time dependence on the interaction between the star and the disk. Since the magnetic field has a spatial symmetry, the interaction with the disk has no symmetry, and hence is three-dimensional, and therefore becomes very complex.

4.3.1 System Radii

The description of the standard paradigm concerning the accretion onto a magnetized neutron star (and the associated torques) is closely related to the relative sizes and attributes of certain radii in the system. The three most prominent are

- **Corotation radius**
  This radius is defined as the radius r_{co} where the accretion disk angular velocity Ω_K (usually assumed Keplerian) has the same value as the angular velocity $\Omega_\star$ of the star. $\Omega_\star = \Omega_K$ gives

$$r_{co} = \left(\frac{GM}{{\Omega_\star}^2}\right)^{1/3} \tag{4.20}$$

  It is clear from Fig. 4.2 that for $r > r_{co}$ the disk will be rotating slower than the magnetic field (which is swept along with the rotating pulsar), and for $r < r_{co}$ the disk will in fact rotate faster than the magnetic field lines. In most models of the disk-magnetosphere interaction this means that for $r > r_{co}$ the disk will gain angular momentum from the magnetic field (since its rotation is slower), and this will lead to a spin-down of the star. For $r < r_{co}$ the disk will lose angular momentum to the field, and a spin-up of the star will occur. This is related to the magnetic shear that occurs inside the disk, and we will return to this later.

- **Disruption radius**
  This is the radius r_0 at which the magnetic field is strong enough to control the disk flow. This radius is formally defined in various ways by different authors, which gives rise to many different values and expressions for r_0. As we shall see below, it is also unclear whether r_0 is the *actual* disruption radius of the disk, or just the radius where disruption *starts*. It is clear that at r_0 the magnetic torques exerted on the disk becomes larger than the viscous torques (which govern the unperturbed

disk), and that therefore the adding or removing of angular momentum to or from the disk is now dominantly magnetic. A crude estimate of this disruption radius is the *Alfvén radius* r_A. This is not defined by torques, but usually as the radius where the magnetic energy density becomes comparable to the total kinetic energy density of the accreting gas, or

$$\frac{B^2(r_A)}{8\pi} \simeq \frac{1}{2}\rho(r_A)v^2(r_A) \tag{4.21}$$

If we assume steady transonic radial equatorial flow at nearly free-fall velocity we may write

$$v(r) \approx v_{ff} = \left(\frac{2GM}{r}\right)^{1/2} \qquad \rho(r) \approx \rho_{ff} = \frac{\dot{M}}{4\pi v_{ff} r^2} \tag{4.22}$$

where the latter expression is derived from mass conservation. If we use (4.1), which holds in the equatorial plane, we get

$$r_A = \left(\frac{\mu^4}{2GM\dot{M}^2}\right)^{1/7} = 1.89 \cdot 10^6 \dot{m}^{-2/7} {\mu_{30}}^{4/7} m^{-1/7} \text{ m} \tag{4.23}$$

More sophisticated estimates of r_0 (based on torques) are surprisingly close to r_A [53] and in fact $r_0 \simeq 0.5 r_A$ is probably a very good estimate. We see that for a nominal pulsar with $m = \dot{m} = \mu_{30} = 1$ we get $r_A \sim 2 \cdot 10^4$ km, or $\bar{r} = r/R = 200$. We can therefore say that the magnetospheric radius can be approximately placed in the middle region of the standard Keplerian disk from Chapter 3, and that the disk thus will be electron scattering and gas pressure dominated for the radii mentioned here.

- **Inner disk radius**

  We have assumed that for $r < r_{co}$ the disk loses angular momentum to the field by magnetic torques, due to the different angular momentum of the disk and field (star). As long as this magnetic torque is dominated by the viscous torque the disk will remain approximately Keplerian. But for a certain value r_0 (defined above) the magnetic torque will dominate. If $r < r_{co}$ the magnetic torque will now remove angular momentum from the disk at a much faster rate than viscous torques does, and the disk will become Sub-Keplerian. The azimuthal velocity v_ϕ will decrease, while the radial infall velocity v_r will increase. At the inner disk radius $r = r_i$ the flow will no longer be in the form of a disk. Because the flow will be along the magnetic field lines, vertical equilibrium will break down, and a gradual vertical loss of disk material (into the magnetosphere) will take place in the transition region. The size of this transition zone is put equal to $\delta = r_0 - r_i$ (Fig. 4.2).

It is here assumed that the binary separation and the accretion disk radius R_d are much larger than the above mentioned radii. This is true for all relevant parameters in pulsar X-ray binaries. One also assumes that the stellar radius R is much smaller than the magnetospheric radius (and other radii), so that the interaction of the flow with the magnetosphere boundary r_0 can be treated, to a good approximation, separately from the interaction of the flow with the stellar surface. This is also usually true for most pulsars, but may not hold for pulsars that are both very fast spinning ($P \sim 1$ ms) and low magnetic ($B \sim 10^8$ G), where both r_0 and r_{co} may be only a few times R.

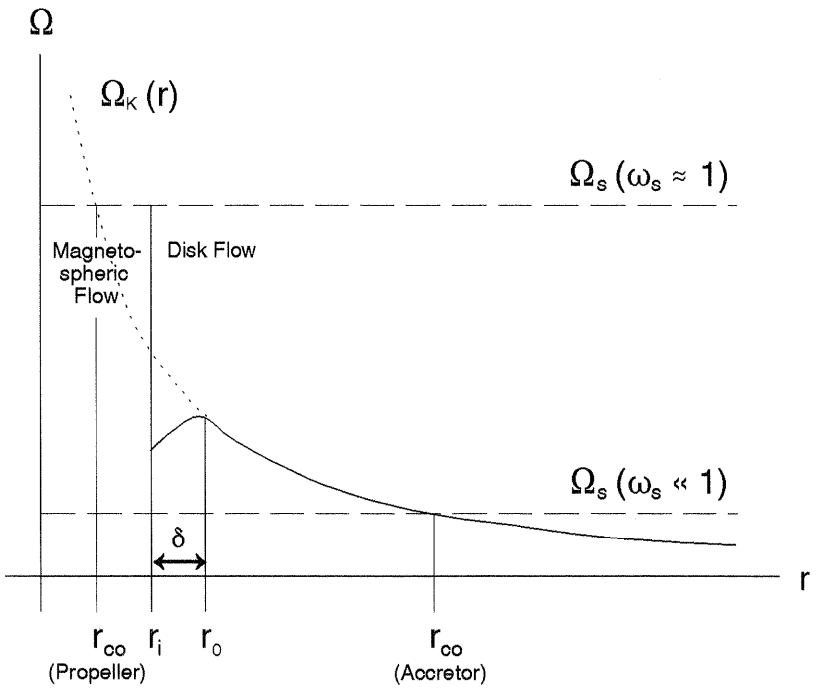

Fig. 4.2 *The essential and characteristic radii for accretion onto a pulsar. Two different corotation radii r_{co} are shown, giving rise to two very different systems.*

4.3.2 Magnetospheric Flow

As discussed above, the disk will disrupt at a radius r_0 (or r_i) and the disk material will merge with the magnetosphere of the star.

The set of field lines threading the boundary layer (the area where the disk dissolves) define the *accretion bundle*, namely those field lines along which matter accretes onto the star. The plasma in the accretion bundle at the disk plane, and just above and below it, still has significant cross field motion. Thus the field lines in this region are only approximate streamlines of the flow. As matter falls closer to the star, its cross field

motion is decelerated by the increasing strength of the stellar magnetic field, while its field aligned motion is accelerated by the gravitational force of the star, and approaches free fall.

There will then be a *flow alignment radius* r_f on every field line of the accretion bundle, inside which the cross field motion of the accreting gas becomes negligible compared with its field aligned motion. The matter will then stream along the field lines and generally end up without significant angular momentum in an area near the polar caps of the star, where a so-called accretion column is generated.

4.3.3 Accretion Torques

With reference to Fig. 4.2 we now look at our four different radial regimes, and we will see that these regimes give rise to quite different torques on the pulsar and the disk. Positive torques spin up the star, while negative spin it down.

- $r > r_{co}$
  In this region the disk will rotate slower than the magnetic field, and there will be a removal of angular momentum from the field (star) onto the disk by a torque $N_4 < 0$. So this is definitely a spin-down region. It is unclear as to exactly how the disk removes the gained angular momentum, but in this part of the disk the viscosity is usually dominant, so the disk will probably remove most of the momentum outwards by the usual viscous mechanism.

- $r_0 < r < r_{co}$
  This is an area in which the disk rotates faster than the magnetic field, and we have a spin-up region because angular momentum in general will be transmitted from the disk to the field (star) by a torque $N_3 > 0$. In most parts of this region the viscous torques are still the dominant ones, and thus in spite of the additional loss of angular momentum through the magnetic torque, the disk will still be approximately Keplerian.

- $r_i < r < r_0$
  We have discussed this area above, and I will now only say that unless δ is considered very small, this region might be both a spin-up or spin-down region, depending on the value for the pulsar spin $\Omega_\star$. We see from Fig. 4.2 that if $\Omega(r_i) < \Omega_\star < \Omega_K(r_0)$ we will in fact have another corotation point inside the δ-region. Otherwise this region will be purely spin-up (if $\Omega_\star < \Omega(r_i)$). We can call the total torque exerted in this region N_2. Most models assume that the value of δ is so small $0.01 < \delta/r_0 < 0.1$ that its contribution can be neglected.

- $r < r_i$

  Here we will only experience spin-up, so that the torque $N_1 > 0$. The material that enters the magnetosphere will deliver *all* of its angular momentum to the star, under the assumption that none (or a very small fraction) of the mass that enters the magnetosphere is expelled. Multidimensional calculations indicate that most of the angular momentum carried by the accreting material in the magnetosphere will be transferred onto the magnetic field [59]. This assumption is open to debate however, as various mechanisms have been suggested that will cause mass ejection or jets from the magnetospheric boundary, and thereby remove angular momentum from the system. Such as for instance so-called Mass Accretion Ejection Structures (or MAES) [60]. Some suggestions have even been made toward the conclusion that most of the angular momentum in the funnel flow has to be propagated back to the accretion disk [61]. This seems unlikely however, as the viscous torques are to small to carry it away.

If we assume that the matter that falls into the polar regions have little angular momentum left, then the transfer of angular momentum onto the star by *direct* material interaction is very small, and the angular momentum is transferred in its entirety through the stressed magnetic field and electrical currents flowing in the magnetosphere. Flow models have been constructed for weakly magnetized pulsars however, where some of the disk matter penetrates the magnetic field (through interchange instabilities), and falls onto the equator (instead of the polar area), and thereby transfers the angular momentum directly through a complicated collisionless shock [56]. Either way, the total angular momentum transferred is the same.

We now put the *total* torque N on the star as follows

$$N = \underbrace{N_1 + N_2}_{N_{in}} + \underbrace{N_3 + N_4}_{N_{out}} \tag{4.24}$$

N_{in} refers to the torque produced inside r_0, while N_{out} is the torque produced outside the radius r_0. Since only a negligible part of the angular momentum carried by the disk at r_0 is sent back by viscous forces (and therefore lost to the magnetic field and star), we will assume that all of this is transferred onto the star and

$$N_{in} = \dot{M} r_0^2 \, \Omega(r_0) \tag{4.25}$$

This is sometimes referred to as the matter torque, since it refers to the angular momentum held by the disk matter at radius r_0, but as we understand this is not really a good

description, since magnetic fields and electric currents are involved at all points in the angular momentum transfer. However, it may be regarded as always positive ($N_{in} > 0$), but with exceptions that I shall mention later. The torque N_{out} is however more complicated, as it may be both positive and negative depending on the value of r_{co} and r_0. In the same fashion as for N_{in} this part of the torque is referred to as the magnetic torque. To find an expression for N_{out} we turn to the use of the vector torque $\boldsymbol{T}_{out} = \boldsymbol{T}_m$, since this (though more unpractical) gives a clearer interpretation of the physics than the use of the scalar torque $N_{out} = \boldsymbol{T_m}/\hat{\boldsymbol{z}}$. Since the magnetic torque on the neutron star is equal and opposite the one on the disk, we get for the torque on the star, using (C.18)

$$\boldsymbol{T}_m = -\frac{1}{\mu_0}\int_{V_d}(\boldsymbol{r}\times\boldsymbol{F}_m)\,dV = -\frac{1}{\mu_0}\int_{V_d}\boldsymbol{r}\times[(\boldsymbol{\nabla}\times\boldsymbol{B})\times\boldsymbol{B}]\,dV \tag{4.26}$$

Where V_d is a volume that encloses the disk. It is straightforward to show that this can be expressed in terms of surface integrals over a surface S_d that encloses V_d

$$\boldsymbol{T}_m = -\frac{1}{\mu_0}\int_{S_d}(\boldsymbol{r}\times\boldsymbol{B})\boldsymbol{B}\,d\boldsymbol{S} + \frac{1}{\mu_0}\int_{S_d}B^2\,(\boldsymbol{r}\times d\boldsymbol{S}) \tag{4.27}$$

From the symmetry of B^2 about $z = 0$, it follows that the second surface integral vanishes. A thin disk has $dH/dr \ll 1$, so $d\boldsymbol{S}$ is nearly parallel to $\hat{\boldsymbol{z}}$ on the upper and lower surfaces, and so the magnetic torque becomes with $d\boldsymbol{S} = 2\pi r^2\,dr\,\hat{\boldsymbol{z}}$ and multiplication with a factor 2 (since both sides of the disk must be included)

$$\boldsymbol{T}_m = -\frac{4\pi}{\mu_0}\left[\int_{r_0}^{\infty}r^2B_\phi^+B_z\,dr - \frac{r_0^2}{2}\int_z B_rB_\phi^+\,dz\right]\hat{\boldsymbol{z}} \tag{4.28}$$

We take from (4.14) that the last integral does not contribute since $|B_r| \ll |B_z|$, and omitting the direction $\hat{\boldsymbol{z}}$, we therefore put the scalar torque N_{out}

$$N_{out} = -\frac{4\pi}{\mu_0}\int_{r_0}^{\infty}r^2B_\phi^+B_z\,dr \tag{4.29}$$

Since the outer limit where the magnetic threading begins is rather undefined, but definitely smaller than R_d, we simply integrate to the infinite.

In electromagnetism there are usually two unit systems that are commonly used, the cgs (or Gaussian) system and the standard SI system. So far in this Chapter and in Appendix C, the SI system have been used. However, many expressions (including the scalar torque) becomes easier to deal with in the cgs-system, and this will be used for calculations from now on. Importantly, in SI units we have for instance $\eta = 1/\mu_0\sigma$, which in cgs units becomes $\eta = c^2/4\pi\sigma$. But we also get, by a look at Maxwell's equation in the two systems

$\mu_0 = 4\pi/c$, and since the Lorentz-force in the cgs-version carries a c^{-1} (compared to in SI units), the $4\pi/\mu_0$ factor in front of (4.29) is reduced to unity, and we have

$$N_{out} = -\int_{r_0}^{\infty} r^2 B_\phi^+ B_z \, dr \tag{4.30}$$

which is more practical to handle. And we then have

$$N = N_{in} + N_{out} = \dot{M} r_0^2 \, \Omega(r_0) - \int_{r_0}^{\infty} r^2 B_\phi^+ B_z \, dr \tag{4.31}$$

Introducing the magnetic pitch parameter γ_ϕ as

$$\gamma_\phi = \left(\frac{B_\phi}{B_z}\right)_{z=H} = -\left(\frac{B_\phi}{B_z}\right)_{z=-H} \tag{4.32}$$

so that (4.30) becomes

$$N_{out} = -\int_{r_0}^{\infty} r^2 \gamma_\phi B_z^2 \, dr \tag{4.33}$$

4.4 The Fastness Parameter

We now look at a parameter which is of profound analytical importance in describing these systems, namely the so-called *fastness parameter*. It was introduced by Elsner and Lamb in 1977 [72], and is defined as

$$\omega_s = \frac{\Omega_\star}{\Omega_K(r_0)} = \left(\frac{r_0}{r_{co}}\right)^{3/2} \tag{4.34}$$

where $\Omega_K(r_0)$ is the Keplerian angular velocity in the point r_0, that is the maximum Keplerian velocity for the disk. I refer again to Fig. 4.2, where this is illustrated. In this way ω_s becomes a measure of the relative positions of the magnetospheric disk disruption radius, and the corotation radius. Using (4.23) and $r_0 \simeq 0.5 r_A$, we can put

$$\begin{aligned} \omega_s &= \left(\frac{r_0}{r_{co}}\right)^{3/2} = \frac{9.45 \cdot 10^5 \dot{m}^{-2/7} {\mu_{30}}^{4/7} m^{-1/7}}{G^{1/3} M^{1/3} \Omega_\star^{-2/3}} \\ &\simeq 0.5 P^{-1} \dot{m}^{-3/7} {\mu_{30}}^{6/7} m^{-5/7} \end{aligned} \tag{4.35}$$

where P is in seconds. It must be made clear that one should use a value of μ_{30} slightly larger than the unscreened dipole moment of the neutron star, since the screening currents flowing in the boundary layer tend to enhance the magnetic field within the magnetosphere (and weaken it on the outside). We will return to this screening later however, and now concentrate on the fastness parameter.

4.4.1 Analysis of ω_s

For slow rotators $\omega_s \ll 1$ or $r_0 \ll r_{co}$, and the negative torque contribution N_4 from outside r_{co} is small compared to the positive from N_3 inside r_{co}. As a result the total torque N is always positive, and we have a spin-up. As ω_s increases, the corotation radius r_{co} is pushed inward towards r_0, and since the area which produces negative torques increases, and the area that produces positive decreases, the total torque gets smaller and eventually $N_3 + N_4 = N_{out} < 0$. The total torque N may still be positive though, since N_{in} always contributes positively. But at one point the ratio r_0/r_{co} (a certain value of ω_s) takes a value such that the positive and negative torques balance $N_{out} = -N_{in}$, and the total torque N vanishes. This gives a *critical fastness parameter* ω_c which defines an equilibrium state for the pulsar, where there is neither spin-up nor spin-down. It is held that this critical fastness parameter ω_c is not a parameter that varies between different pulsars (like ω_s will do), but instead is a universal constant (within the applicability of this model of course). Most estimates of ω_c places it in the range $0.6 < \omega_c < 0.95$ [62][63].

Propeller Regime

We clearly see that if $r_{co} < r_0$ then $\omega_s > 1$, and from this we gather that the disk matter never reaches the corotation radius r_{co} before the disk is disrupted. Thus the only interaction taking place between disk and magnetic field results in a spin-down torque $N_4 < 0$. In this case the pulsar is what we call a *propeller* or is in a so-called propeller regime. The traditional view is that in the propeller regime accretion is almost entirely prohibited due to centrifugal forces. Because the magnetic field rotates faster than the Keplerian disk, gravity cannot keep the matter trying to flow along the field lines in place, and it is therefore propelled away from the pulsar, depriving it of angular momentum.

What seems clear for these cases is that as long as $\omega_s > 1$ the pulsar will not be accreting matter from the disk, at least not in a one-dimensional treatment. Unless matter is expelled from the disk and star, or can accrete past the disruption point in some way, it will necessarily build up outside r_0, and a steady accretion does not seem to be possible. It is conceivable however, that the stellar field lines may thread only the surface layers of the disk, which would then be subject to propeller action, while the diamagnetic plasma near the midplane of the disk continues to flow toward the star.

Since matter probably must reach inside the magnetosphere to create the X-ray pulses and other characteristics seen from such pulsars, no such emission will be observable from such systems. The pulsar will still act as an X-ray source though, since the disk itself probably will emit an intense radiation, and even if the mass transfer should stop altogether, the pulsar would still be observable as an ordinary radio pulsar. The dynamics related to the propeller regime are rather unclear, and is a field of rigorous investigation.

Change of Fastness

The value of ω_s (and therefore many important characteristics of the system) will depend the three essential parameters

- **The mass transfer rate $\dot{M}$**

  As we have seen, this is a parameter that may change on the order of days or weeks in most standard accretion systems (or perhaps in some systems even faster), thus causing changes that are readily observable. We can see from (4.23), and this applies generally, that the radius r_0 (or in this case r_A) scales as $\sim \dot{M}^{-2/7}$. If other parameters remain fixed while $\dot{M}$ (or equivalently the luminosity L) varies, ω_s will change. As the luminosity (or $\dot{M}$) increases, ω_s ($\sim \dot{M}^{-3/7}$) and r_0 will decrease and the torque will increase. Thus changes in spin-up (or spin-down) rates that are not on too fast a timescale ($\lesssim 1$ day) can be explained by changes in mass transfer rate $\dot{M}$ if they are accompanied by a rise in luminosity. If $\dot{M}$ increases sufficiently, a system may even pass from a propeller state to a spin-up state relatively fast. For most systems the mass transfer rate is quite steady, or at least passes through long lived quasi steady states, so that the system will have a constant ω_s.

- **The spin period $\Omega_\star$**

  Unlike $\dot{M}$, the spin rate $\Omega_\star$ cannot vary sufficiently fast as to change the characteristics of the system in the order of days. The spin period P and period change $\dot{P}$ for pulsars can however be measured very accurately for many systems. Significant changes in P are slow and gradual, and will affect the system on very long timescales $\gtrsim 10^6$ yr. The corotation radius r_{co} is only affected by $\Omega_\star$, and not by other parameters. Since $\omega_s \sim P^{-1}$, it becomes clear that fast rotators are much more difficult to spin up than the slow rotating ones. So as a star gradually spins up (on a long timescale) it will slowly increase its ω_s so that is approaches ω_c, and the spin-up will be halted. Alternatively if the star spins down, it will also approach ω_c from the other side, that is for gradually decreasing ω_s. In other words: given enough time, an equilibrium spin period P_{eq} will be reached for the system. Once the period P_{eq} is reached, the spin will fluctuate around this equilibrium with periodic spin up and spin down variations. Most estimated results give that

$$P_{eq} \sim \dot{M}^{-a} \tag{4.36}$$

  where $a > 0$ is a constant of order unity that differs from model to model. Thus the minimum P_{eq}, or fastest possible equilibrium rotation rate occurs when $\dot{M}$ is at Eddington-rates. Any other mass transfer rates $\dot{M}$ will instill the system onto a larger P_{eq}.

- **The magnetic field strength B_0**
  We see, again from (4.23), that $r_0 \sim {\mu_{30}}^{4/7}$, and that therefore r_0 will decrease if the magnetic field of the pulsar (over a very long timescale) dissipates. This causes ω_s to decrease as well, and therefore facilitates spin up of the star. The effect is balanced by the fact that a spin-up, as mentioned above, also decreases the corotation radius r_{co} and thereby brakes further spin-up. We are for this reason lead to believe that accreting highly magnetized neutron stars ($P \gtrsim 10^{12}$ G) with fast rotation ($P \lesssim 1$ s) always are either propellers (spin-down profile) or close to the propeller regime ($\omega_s \gtrsim 1$). At the other end of the scale we find the slowly rotating and weekly magnetized neutron stars (very low ω_s) that show a clear spin-up profile.

The relations between these parameters and the spin evolution of the star will be given a more quantitative treatment later on.

Of course, since such systems tend to exhibit a variation of complex and differing behavior (many of which are far from being well understood), a complete description will also include many other parameters as well. But many essential characteristics can be explained from the three outlined above.

4.4.2 The Dimensionless Fastness Function

We now define the dimensionless function

$$n = \frac{N}{N_{in}} = 1 - \frac{N_{out}}{N_{in}} = 1 - \frac{\int_{r_0}^{\infty} r^2 B_\phi^+ B_z \, dr}{\dot{M}(GMr_0)^{1/2}} \tag{4.37}$$

What is special about this function n is that generally it depends only on ω_s, so that it is possible to write [53]

$$N \approx n(\omega_s) N_{in} \tag{4.38}$$

In practical terms however, in order to calculate $n(\omega_s)$ we need to estimate r_0, and thereafter calculate the B_ϕ-field. There are many approaches to this, and they usually give differing expressions or results for $n(\omega_s)$, and therefore also different values for ω_c given by the condition $n(\omega_s) = 0$ [62]. An expression for $n(\omega_s)$ that to some degree fits numerical results over a wide range of $\omega_s < 1$ [55] is

$$n(\omega_s) \approx 1.4 \left(\frac{1 - \omega_s/\omega_c}{1 - \omega_s} \right) \tag{4.39}$$

We see that as $\omega_s \to \omega_c$ we get $n(\omega_s) \to 0$ as we should. When $\omega_s \to 0$ we have $n(\omega_s) \to 1.4 N_{in}$ and therefore $N_{out} = 0.4 N_{in}$. So this means that the maximum torque

is $N_{max} = 1.4N_{in}$, and is associated with very slow rotators. If $\omega_c < \omega_s < 1$ we get a negative torque, also as expected. We see these relations as a plot in Fig. 4.3, for three different values of ω_c.

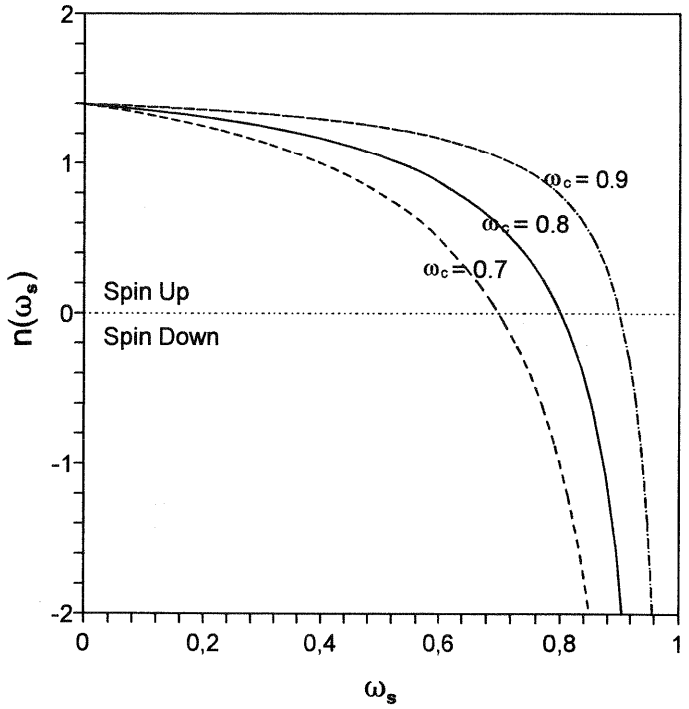

Fig. 4.3 *An expression for the dimensionless function $n(\omega_s)$ plotted for three values of the critical fastness parameter $\omega_c = 0.7, 0.8$ and 0.9.*

4.4.3 Comparison with Pulsar Data

The model we have described so far can be used to give a simple relation between the spin-up rate $\dot{P}$ and the quantity $PL^{3/7}$, provided the inertial moment of the neutron star is constant. We recollect that from (4.38) we have $N = n(\omega_s)N_{in}$, and if we look at the equation for change in the stellar angular velocity $\Omega_\star$ produced by the torque N we can put

$$\dot{\Omega}_\star = -\frac{2\pi}{P^2}\dot{P} = \frac{N}{I_\star} = \frac{n(\omega_s)\,\dot{M}(GMr_0)^{1/2}}{I_\star} \tag{4.40}$$

where $\Omega_\star = 2\pi/P$ and $N_{in} = \dot{M}(GMr_0)^{1/2}$. This gives

$$-\dot{P} = \frac{P^2}{2\pi}\frac{\dot{M}(GMr_0)^{1/2}}{I_\star}n(\omega_s) \tag{4.41}$$

If we use the expression for $r_0 = 0.5r_A$ in the form

$$r_0 = 9.45 \cdot 10^5 \dot{m}^{-2/7} {\mu_{30}}^{4/7} m^{-1/7} \tag{4.42}$$

we get

$$-\dot{P} = 5 \cdot 10^{-5} f_{\mu_1}(\mu_{30}) f_{m_1}(m) \left[P L_{30}^{3/7}\right]^2 n(\omega_s) \tag{4.43}$$

in units of seconds per year. Equation (2.9) has been used for the luminosity, and L_{30} is the luminosity in units of $10^{30}\mathrm{J\,s^{-1}}$. The two functions f_{μ_1} and f_{m_1} are functions of respectively μ_{30} and the mass m (or M) only, and

$$f_{\mu_1}(\mu_{30}) = {\mu_{30}}^{2/7} \tag{4.44}$$

and

$$f_{m_1}(m) = m^{-3/7} I_{38} = 0.8\, m^{4/7} \tag{4.45}$$

where we have put $R = 10$ km, and I_{38} is the moment of inertia in units of $10^{38}\,\mathrm{kg\,m^2}$. If we assume that the moment of inertia is roughly that given by a sphere $I = 2MR^2/5$, we get $I_{38} = 0.8\,m$, and thereby (4.45) follows. From (4.35) we get

$$\omega_s = 1.35\, f_{\mu_2}(\mu_{30})\, f_{m_2}(m) \left[P L_{30}^{3/7}\right]^{-1} \tag{4.46}$$

where we have

$$f_{\mu_2}(\mu_{30}) = {\mu_{30}}^{6/7} \qquad f_{m_2}(m) = m^{-2/7} \tag{4.47}$$

Since ω_s is a function of the variable $PL_{30}^{3/7}$ then

$$n(\omega_s) = 1.4 \left(\frac{1 - \omega_s/\omega_c}{1 - \omega_s}\right) = n\left[\omega_s\left(P L_{30}^{3/7}\right)\right] \tag{4.48}$$

is also a variable of $PL_{30}^{3/7}$ (for a given ω_c), and this means that the value of $-\dot{P}$ for a pulsar of given mass and magnetic moment is a function only of $PL_{30}^{3/7}$. Therefore, measurements of $P, \dot{P}$ and L for pulsars that have different spin periods and/or different luminosities but are otherwise identical, or measurements of $P, \dot{P}$ and L of a given pulsar made at different times (assuming that its spin and luminosity has changed during the time interval), will fall on a single curve in a plot of $(-\dot{P})$ vs. $PL^{3/7}$.

The character of the relation between $-\dot{P}$ and $PL_{30}^{3/7}$ is shown in Fig. 4.4, where a plot have been done for three values of the magnetic moment μ_{30} for $\omega_c = 0.8$ and $m = 1.4$. The variation in mass between different pulsars is much smaller than the variation in

magnetic field strength, and therefore the most interesting is a plot where μ is allowed to vary. Also the magnetic field of many pulsars are known, while their mass is much harder to determine.

For large values of $PL_{30}^{3/7}$ the pulsar is a slow rotator ($\omega_s \ll 1$). ω_s is therefore approximately constant (see Fig. 4.3), and $-\dot{P}$ scales as $(PL_{30}^{3/7})^2$. Thus we see from (4.43) that the curve should describe a straight line of slope 2 in a Log $(-\dot{P})$ vs. Log $PL_{30}^{3/7}$ plot, for the region of slow rotation. As $PL_{30}^{3/7}$ decreases, the fastness parameter ω_s becomes larger (n decreases) and Log $(-\dot{P})$ falls below the extrapolation of this line. Finally at the value of $PL_{30}^{3/7}$ for which $\omega_s = \omega_c$, $\dot{P}$ vanishes and Log $(-\dot{P})$ diverges. We can also observe that along any vertical line, all pulsars will have the same fastness since $\omega_s \sim PL_{30}^{-3/7}$, and that therefore fast and slow rotators are separated in a systematic way, with fast rotators to the left and slow rotators to the right.

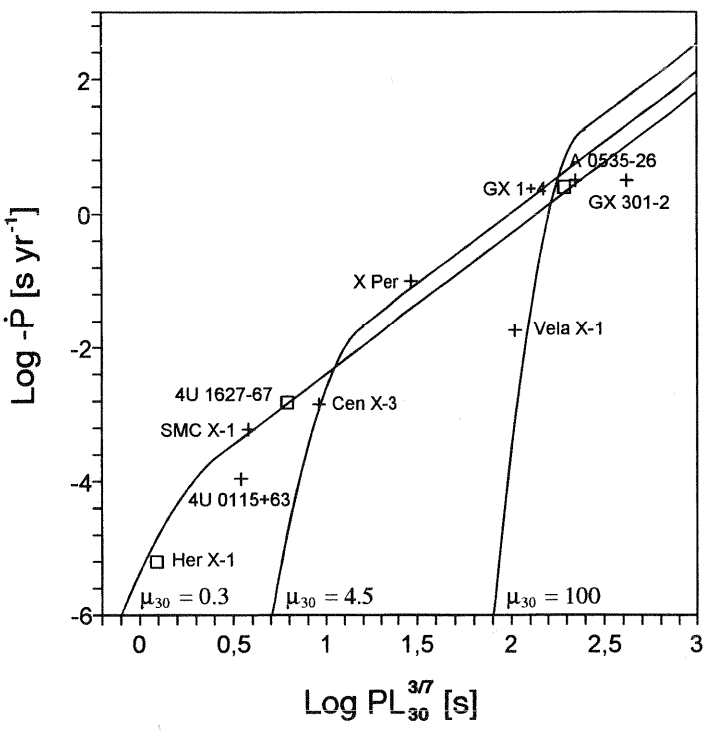

Fig. 4.4 *The theoretical relation between $-\dot{P}$ and $PL_{30}^{3/7}$ superimposed on data for 10 X-ray binary pulsars (Table 2.2). The three curves correspond to three different values of μ_{30}. This plot is for $m = 1.4$ and $\omega_c = 0.8$. HMXB are crosses, while LMXB are boxes.*

If we consider a collection of accreting X-ray pulsars, they would all lie on the same curve $-\dot{P} = f(PL_{30}^{3/7})$ if they had the same magnetic moment. Although all these pulsars are not expected to have identical magnetic moments, there should still be a correlation between $-\dot{P}$ and $PL_{30}^{3/7}$ if the spread in masses is not too large. Note that the curves

for different values of μ_{30} cross one another. This crossing of the curves occurs because the higher moment gives the larger torque and hence the larger spin-up rate in the slow rotator region (large values of $PL_{30}^{3/7}$), so that the spin-up rate in the fast rotator region falls more rapidly for the higher moment than for the lower ones.

For the pulsars lying in the upper right part of the plot (along the line with slope +2), it is difficult to establish the magnetic field strength, since the curves are very close. We see however that the Vela-pulsar seems to trace the curve for which $\mu_{30} = 100$, and this would indicate a magnetic field in the magnetar range $\sim 10^{14} - 10^{15}$ G.

4.5 Calculation of the Stellar Torques

There are many uncertainties in the estimation of the total torque on an accreting X-ray pulsar. Within the model however, the major uncertainty lies in the nature and value of the toroidal magnetic field B_ϕ.

4.5.1 Screening Factor

To calculate the effective torque N one must estimate the toroidal magnetic field B_ϕ. It is shown in (4.15) that the B_z component of the field is unchanged to good approximation if the thin disk assumption is made. So we may freely use the dipole magnetic field for B_z in the disk plane. We will introduce a screening factor S to make up for the screening effect of the induced magnetic field, since the disk will lie in the region *outside* the boundary layer where this screening currents flow, the magnetic field will be weakened by a factor s. In a self-consistent treatment, the radial dependence of S must be found from a detailed analysis of the magnetospheric current system in the corona. A conclusive analysis has not yet been made, so we rather assume that the vertical component of the magnetic field threading the disk can be represented by

$$B_z \simeq -S_{eff} \frac{\mu}{r^3} \tag{4.49}$$

where S_{eff} is an effective screening coefficient taken to be a constant over a wide range of relevant radii. As to the value of S_{eff}, differing values exist in literature, but we will adopt the value $S_{eff} = 0.2$ [70], which seems to be widely recognized.

4.5.2 The Toroidal Field

This can be done in a number of ways, but we will use the induction equation (C.6) in the Gaussian system, for a plasma having an effective conductivity σ_{eff}

$$\frac{\partial \boldsymbol{B}}{\partial t} = \boldsymbol{\nabla} \times \left[\boldsymbol{v} \times \boldsymbol{B} - \frac{c^2}{4\pi\sigma_{eff}} \boldsymbol{\nabla} \times \boldsymbol{B} \right] \tag{4.50}$$

Near the disk plane, where as we have seen that B_r and v_r are small, the dominant contribution to the ϕ-component of this equation is

$$\frac{\partial B_\phi}{\partial t} \simeq B_z \frac{\partial v_\phi}{\partial z} - \frac{\partial}{\partial z}(v_z B_\phi) + \frac{c^2}{4\pi} \frac{\partial}{\partial z} \left(\frac{1}{\sigma_{eff}} \frac{\partial B_\phi}{\partial z} \right) \tag{4.51}$$

This equation then describes the balance between the diffusion of the toroidal magnetic field B_ϕ and its creation due to the vertical shearing of the poloidal field B_z. The three terms on the right hand side represent, respectively, the winding of the poloidal field by the differential rotation, the convection of the wound flux by the plasma, and its dissipation.

The highly conducting magnetosphere will be essentially corotating with the neutron star, and therefore the angular velocity of the disk material will change its value near the surfaces $z = \pm H(r)$. Consequently, there is a large vertical shear in the disk. A linear estimate for the vertical shear velocity gradient through the disk would be

$$\frac{\partial v_\phi}{\partial z} \simeq \pm\gamma(\Omega_\star - \Omega_K) \tag{4.52}$$

where γ gives the rate of change, and is assumed to be of order unity. This will give a rather gradual change in the velocity profile, in such a way that the change of v_ϕ continues into the magnetosphere. The assumption $\partial v_\phi/\partial z \sim \pm(\Omega_\star - \Omega_K)r/H$ would produce a much steeper profile, where the whole change took place for $z < |H|$.

From (4.51) we then get the toroidal flux generation rate

$$\left(\frac{\partial B_\phi}{\partial t} \right)_+ \simeq \pm\gamma(\Omega_\star - \Omega_K) B_z \tag{4.53}$$

Since $v_z \simeq 0$ within the disk (where $\boldsymbol{v}$ would refer to the mean flow) this growth must be balanced by diffusive losses, represented by the last term of (4.51). We here follow [53] and assume that this, with τ_d being the diffusion time scale, can be expressed in the form

$$\left(\frac{\partial B_\phi}{\partial t} \right)_- \simeq -\frac{B_\phi}{\tau_d} \simeq -\frac{\xi |v_{A\phi}| B_\phi}{H} \tag{4.54}$$

where ξ is a factor that inhibits the diffusion of the B_ϕ field for large z, and the speed $v_{A\phi} = B_\phi/\sqrt{4\pi\rho}$ is the *Alfvén speed* connected to the field B_ϕ. The Alfvén speed is the maximum rate at which changes in the field can propagate through the plasma. Likewise we define the Alfvén speed for B_z as $v_{Az} = B_z/\sqrt{4\pi\rho}$. Because the annihilation of the B_ϕ field is assumed to take place for all z, the order of ξ is assumed to be close to unity. This

is assured by the magnetic buoyancy mechanism mentioned earlier, in which magnetic tubes will rise in the disk.

Putting (4.53) equal to (4.54), and changing from $v_{A\phi}$ to v_{Az} we get

$$\gamma_\phi = \frac{B_\phi}{B_z} \simeq \pm \left| \frac{\gamma(\Omega_\star - \Omega_K)H}{\xi v_{Az}} \right|^{1/2} \tag{4.55}$$

for the azimuthal pitch of the magnetic field lines threading the disk.

4.5.3 Magnetic Torques N_3 and N_4

As we have seen, the torque $N_{out} = N_3 + N_4$ is called the magnetic torque on the star. In addition we have of course, the term N_{in}.

The Spin Down Torque N_4

The term $N_4 < 0$ is a spin-down torque, because the lines of force that intersect the disk in the domain where $\Omega_\star > \Omega_K$ are swept backwards, and exert a corresponding drag on the star. This negative contribution N_4 to the net torque is determined by integrating the magnetic stresses from the corotation radius r_{co} outward to infinity. We put

$$N_4 = -\int_{r_{co}}^{\infty} dr\, r^2 \left[B_\phi(r) B_z(r) \right]_{z=H} \tag{4.56}$$

Using (4.55) for the magnetic fields we get

$$N_4 \simeq -\int_{r_{co}}^{\infty} \left| \frac{\gamma}{\xi} \left\{ \left(\frac{r}{r_{co}} \right)^{3/2} - 1 \right\} \left(\frac{\Omega_K H}{v_{Az}} \right) B_z^4 r^4 \right|^{1/2} dr \tag{4.57}$$

We now assume that B_z has the dipolar form (4.49), and we collect expressions for H, ρ and c_s from Chapter 3. I have mentioned earlier that the relevant radii here are assumed to lie in the middle region of the unperturbed α-disk, so we use (3.72) for the gas pressure and electron scattering dominated region. We can rewrite these as

$$c_s \simeq 106.35\, \dot{M}^{1/5}\, \Omega_K^{3/10}\, \alpha^{-1/10} \tag{4.58}$$

$$\rho \simeq 8 \cdot 10^{-2}\, \dot{M}\, \Omega_K^2\, \alpha^{-1}\, c_s^{-3} \tag{4.59}$$

and where $H = c_s/\Omega_K$ will be useful as well. If we use the variable $y = (r/r_{co})^{3/2}$ we can write this integral as

$$N_4 \simeq -\frac{2}{3} N_{co} \int_1^{\infty} (y-1)^{1/2}\, y^{-291/120}\, dy \tag{4.60}$$

where we have put

$$N_{co} \equiv \left(\frac{\gamma}{\xi}\right)^{1/2} \left[\frac{c_s(r_{co})}{v_{Az}(r_{co})}\right]^{1/2} B_z^2(r_{co})\, r_{co}^3 \tag{4.61}$$

and since the minus sign disappears altogether inside the integral we put the dipole magnetic field at the corotation radius as

$$B_z(r_{co}) = S_{eff} \frac{\mu}{r_{co}^3} \tag{4.62}$$

and also

$$c_s(r_{co}) = 106.35\, \dot{M}^{1/5}\, \Omega_\star^{3/10}\, \alpha^{-1/10} \tag{4.63}$$

$$\rho(r_{co}) \simeq 8 \cdot 10^{-2}\, \dot{M}\, \Omega_\star^2\, \alpha^{-1}\, c_s^{-3}(r_{co}) \tag{4.64}$$

and for the Alfvén speed we have

$$v_{Az}(r_{co}) = \frac{B_z(r_{co})}{[4\pi\rho(r_{co})]^{1/2}} \tag{4.65}$$

We can approximate $291/120 = 2.425$ with $5/2 = 2.5$ in the integrand, so that

$$\int (y-1)^{1/2}\, y^{-5/2}\, dy = \frac{2}{3}\left(1 - \frac{1}{y}\right)^{3/2} \tag{4.66}$$

and this gives

$$N_4 \simeq -\frac{4}{9} N_{co} \tag{4.67}$$

The Spin Up Torque N_3

The angular momentum that the rotating magnetosphere imparts to the disk in the region $r > r_{co}$ is transferred outward by viscous shear stresses within the disk. There may be other forms of angular momentum loss from the disk in this area [71], but the viscosity mechanism is assumed to be dominant. Because the strength of the magnetic field rises steeply toward the pulsar however, there will be some radius r_0 inside which the magnetic stresses rapidly become dominant, and the viscous transport may be neglected. As we have seen, when $r_0 < r_{co}$, the orbital angular momentum convected across this point by the bulk flow is eventually transferred to the pulsar, contributing the amount

$$N_{in} \simeq \dot{M}\, (GMr_0)^{1/2} \tag{4.68}$$

to the net torque.

We have seen that r_0 does not necessarily represent the true inner edge of the disk. A more sophisticated estimate for r_0 than $r_0 \simeq 0.5 r_A$ is found by setting the magnetic stress equal to the rate at which the angular momentum is removed (by internal viscous forces) in a steady-state Keplerian disk. Using (3.7) we can put

$$-r^2 \left[B_\phi(r) B_z(r)\right]_{z=H} = \dot{M} \frac{d}{dr} \left[\Omega_K(r)\, r^2\right] \tag{4.69}$$

Again, with B_z given by (4.49), using (4.55) for B_ϕ and with use of the same expressions (4.61) through (4.65) we get

$$\frac{r_0}{r_{co}} \simeq \left\{ \frac{2N_{co}}{\dot{M}(GMr_{co})^{1/2}} \left[1 - \left(\frac{r_0}{r_{co}}\right)^{3/2}\right]^{1/2} \right\}^{80/211} \tag{4.70}$$

which do not give r_0 explicitly, but as the ratio r_0/r_{co}. A puzzling thing about this expression is that it indicates that the value of r_0 could depend on r_c (and therefore on $\Omega_\star$), while it is expected that it should depend on $\dot{M}$ and μ only. Clearly, there are no solutions for $r_0/r_{co} > 1$, since the pulsar then would have entered the propeller regime. The contribution to the magnetic stresses from the domain $r_0 < r < r_{co}$ may however be calculated since we may put $y = (r/r_{co})^{3/2}$ as above, and then the value of r_0 only enters through the ratio r_0/r_{co}. This is as it should be, since the total torque on the star, according to earlier results, should depend only on the fastness parameter $\omega_s = (r_0/r_{co})^{3/2}$.

Now, following the notation and approximations from the case for N_4 (the integrals are basically almost the same) we may put.

$$-\int_{r_0}^{r_{co}} dr\, r^2 \left[B_\phi(r) B_z(r)\right]_{z=H} = \frac{2}{3} N_{co} \int_{\omega_s}^{1} (1-y)^{1/2}\, y^{-291/120}\, dy \tag{4.71}$$

where the lower integral limit is in fact $y_0 = \omega_s$. So we get

$$N_3 \simeq \frac{4}{9} N_{co} \left[\left(\frac{r_{co}}{r_0}\right)^{3/2} - 1\right]^{3/2} \tag{4.72}$$

for the spin-down torque on the pulsar.

The Total Torque $N = N_{in} + N_3 + N_4$

Summing up the torques we get for the total torque acting on the star $N = N_{in} + N_3 + N_4$ as

$$N \simeq (GMr_{co})^{1/2} + \frac{4}{9} N_{co} \left\{ \left[\left(\frac{r_{co}}{r_0}\right)^{3/2} - 1\right]^{3/2} - 1 \right\} \tag{4.73}$$

If use is made of (4.70) to eliminate N_{co} this result may be rewritten as

$$N \simeq N_{in}\left\{1+\frac{2}{9}x_0^{-9/80}\left[1-x_0^{3/2}-\frac{x_0^{9/4}}{\left(1-x_0^{3/2}\right)^{1/2}}\right]\right\} = N_{in}\, n(\omega_s) \tag{4.74}$$

where $N_{in} = \dot{M}(GMr_{co})^{1/2}x_0^{1/2}$ and $x_0 = r_0/r_{co} < 1$. Solving $N_{in} = 0$ numerically gives a value $x_0 \simeq 0.971$. So that at this equilibrium point

$$x_{eq} = \frac{r_{eq}}{r_{co}} \simeq 0.971 \rightarrow \omega_s = x_{eq}^{3/2} \simeq 0.957 \tag{4.75}$$

a rather high value for the critical fastness parameter. If $x_0 < x_{eq}$ then $N > 0$ and the neutron star spins up, and conversely it spins down if $x_0 > x_{eq}$.

We define the function

$$f(x_0) = x_0^{1/2} + \frac{2}{9}x_0^{31/80}\left[1-x_0^{3/2}-\frac{x_0^{9/4}}{\left(1-x_0^{3/2}\right)^{1/2}}\right] \tag{4.76}$$

which, then means that $N = \dot{M}(GMr_{co})^{1/2} f(x_0)$. In Fig. 4.5d we see a plot of $f(x_0) = N/\dot{M}(GMr_{co})^{1/2}$ as a function of $x_0 = r_0/r_c$. With the use of the expressions (4.63) and (4.64), the factor $2N_{co}/\dot{M}(GMr_{co})^{1/2}$ may be written as a function $g(\dot{M}, P, \mu)$. By noting that (4.70) then becomes

$$g(\dot{M}, P, \mu) = \frac{x_0^{211/80}}{\left(1-x_0^{3/2}\right)^{1/2}} \tag{4.77}$$

(4.70) may be solved numerically. By keeping two of the variables constant, we are then able to plot the dependence of x_0 on the third. We take the constants γ, ξ and α to be of order unity and these are therefore put equal to one. The neutron star mass $M = 1.4\, M_\odot$, and we use the screened magnetic field $\chi_{30} = S_{eff}\,\mu_{30} \simeq 0.2\,\mu_{30}$. In Fig. 4.5a we see the dependence of $x_0 = r_0/r_{co}$ upon variation in the pulsar spin P, here we have put $\dot{M} = M_{crit} \rightarrow \dot{m} = 1$ and $\chi_{30} = 1$. Likewise in Fig. 4.5b for variation of the screened magnetic field χ, we put $\dot{m} = 1$ and $P = 1$ s. We can see that these two have an opposite and quite equal effect of x_0. In Fig. 4.5c we see the same plot, but this time for the mass accretion rate $\dot{M}$, and with the above values for P and χ_{30} taken. It appears clear that x_0 is rather less sensitive to variations in $\dot{M}$ than to changes in the other two parameters.

Again, from (4.70) we can find (with $\gamma \simeq \xi \simeq \alpha \simeq 1$) that

$$P = 12.43\,\chi_{30}^{180/211}\, L_{30}^{-96/211}\, \frac{\left(1-x_0^{3/2}\right)^{1/3}}{x_0^{211/120}} \tag{4.78}$$

measured in seconds, and where we again have put $M = 1,4\,M_\odot$ and $R = 10$ km. Also, $\dot{M}$ has been replaced with the equivivalent L. We know that the equilibrium period P_{eq} is determined by the condition $x_0 = x_{eq} = 0.971$. From that we get

$$P_{eq} = P(x_0 = x_{eq}) = 4.60\,\chi_{30}^{180/211}\,L_{30}^{-96/211} \tag{4.79}$$

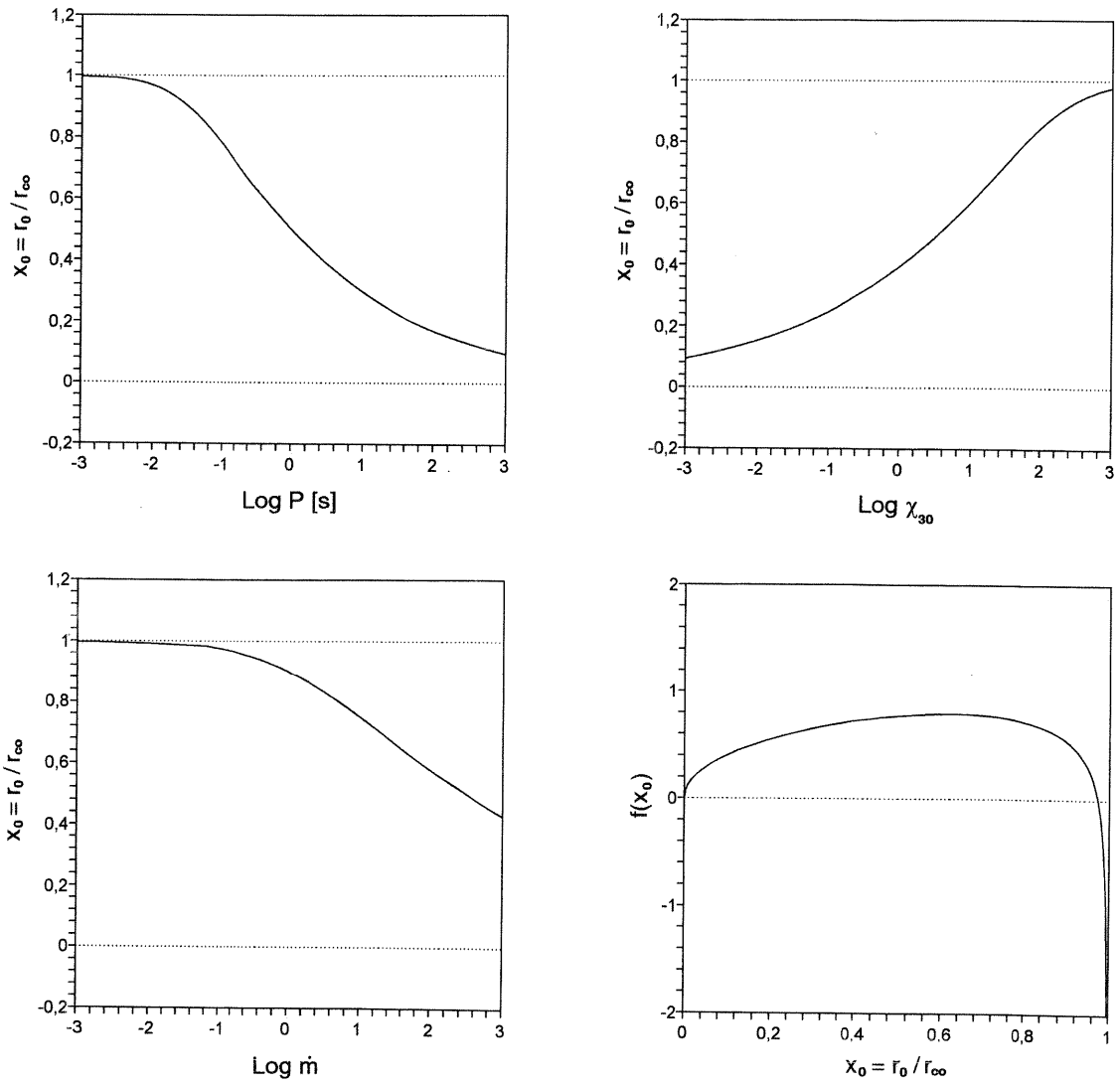

Fig. 4.5abcd *We see the dependence of the fastness related parameter* $x_0 = r_0/r_{co}$ *on the important system parameters* $\dot{M}$,P *and* μ *(or* χ*). In the last Fig. 4.5d, we see the torque function* $f(x_0)$ *plotted as a function of* x_0

4.5.4 The Spin-Up Line

The important thing for the spin evolution (the value of ω_s) of the pulsar in the long term ($\gtrsim 10^6$ yr), is the balance between the assumed weakening of the magnetic field

(which will decrease r_0 and support spin-up) and the shortening of the period P (which will decrease r_{co} and halt the spin-up). Since there is as yet no convincing models for the mechanism by which the magnetic field of an accreting pulsar dissipates, the dissipation is only an empirical fact. In this (and many other) models for the spin evolution of pulsars, the decrease of the magnetic field strength is paramount since a strong magnetic field effectively stops spin-up and could also stop accretion altogether. This accretion induced field decay scheme is supported by the fact that no pulsars known today with fast spin ($P \lesssim 0.1$ s), has a strong magnetic field.

If we use (4.35) for the fastness parameter, and put $m = 1.4$, $\dot{m} = 1$ and replace μ_{30} with the enhanced field $\approx 5 \cdot \mu_{30}$ we get

$$\frac{0.68}{P}\,\mu_{30}^{6/7} = \omega_s \tag{4.80}$$

If we demand $w_s < w_c$, which is the spin-up condition, then

$$\frac{0.68}{P}\,\mu_{30}^{6/7} < \omega_c \tag{4.81}$$

defines the two regions in the BP-plane where spin-up and spin-down would occur. If these regions are depicted in a Log B vs. Log P-plot, their boundary would be a straight line, called the *spin-up line*

$$\mathrm{Log}\,\mu_0 = \frac{7}{6}\,(0.17 + \mathrm{Log}\,\omega_c) + \frac{7}{6}\,\mathrm{Log}\,P \tag{4.82}$$

Pulsars that lie above this line will be spin-down cases, while those below it should be spin-up. In Fig. 5.1 of Chapter 5, this spin-up line is plotted along with the pulsar data.

All this is of course based on the naive expression for r_A, derived for the case of spherical accretion, but the estimate $r_0 = a \cdot r_A$ (where a is of the order unity) has proved to be astonishingly accurate by most standards, and is close to the result returned from many other calculations of r_0.

4.5.5 Dramatic Torque Reversals

Observations made by the Caltech BATSE group, using the Compton Gamma Ray Observatory over the last years, have revealed certain dramatic and unexpected behaviour in some of the X-ray binary pulsar systems. The most dramatic of these observations is the torque reversal of the pulsar GX 1+4, but similiar measurements have been made on other pulsars as well. The characteristics of the torque reversals are

- The observed torque appears to switch rapidly between two states of opposite sign. That is, the spin-up rate changes very fast to a spin-down rate of *exactly* the same magnitude. In the standard models this requires very dramatic step-function like changes in the accretion rate $\dot{M}$.

- For GX 1+4, which is a slow rotator with ($P \sim 120$ s), the assumption that this change was due to some very fast change in the mass accretion rate, means that the torque reversal should be accompanied with a decrease in the luminosity. However, the luminosity is observed to be persistent in the GX 1+4 system, even through the torque reversals.

- Since GX 1+4 is a very slow rotator, it would need a large magnetic field $\gtrsim 10^{14}$ G in order to be an equilibrium period pulsar. Such a field does not seem plausible for the GX 1+4 system, and it still could not explain all features of the torque reversals.

The fact that the spin-down rate following these torque reversals is symmetric to the spin-up rate before the reversal, has lead to speculations of a disk flip. The disk flip would involve the change from a disk rotating in the same direction as the neutron star, to a disk with retrograde movement. If the conditions for the disk and flow are the same, then the retrograde disk would cause a spin-down with the exact same magnitude as the spin-up caused by the old disk. There are however, no known mechanisms or processes in these systems that can be invoked to explain such a disk flip.

Another possible explanation is that the observed torque alternation is the result of a *magnetic reconfiguration*, and that this can be triggered by mechanisms other than the accretion rate $\dot{M}$. In this picture, the observations may be interpreted by having two states of the magnetosphere, resulting in two different torque states. Such alterations in the magnetospheric structure can occur on a much faster timescale than any accretion mass flow. Whether the magnetospheric change is a disk induced magnetospheric instability, or not triggered by the disk at all, is unclear.

The validness of many of the features of the theory for accreting binary X-ray pulsars are clearly open to discussion. However, the main characteristics of these systems fits well into the assumptions of the standardized views. These new observations may demand explanations that probably will operate alongside the standard views, and not a completely new theory.

Chapter 5

Millisecond Pulsars

It is assumed that the origin of the observed population of millisecond pulsars somehow is related to accretion processes in X-ray binary pulsars. We now look at the validity of this idea.

5.1 Spin-Up Phase

Apart from their short spin periods, the other distinguishing character of the millisecond pulsars is their weak magnetic fields. One may use the dipole model for pulsars to derive an expression for the dipole field strength of the pulsar as

$$B \sim (P\dot{P})^{1/2} \tag{5.1}$$

This is not valid for accreting X-ray pulsars, where $\dot{P}$ is substantially different from that of radio pulsars. The inferred magnetic field strengths is of the order $\sim 10^8 - 10^9$ G.

In addition to this, an overwhelmingly large fraction of the millisecond pulsars are members of binary systems. Among millisecond pulsars the fraction that are established as components in a binary system is as high as $\gtrsim 50\%$, while for regular radio pulsars the fraction is $\sim 5\%$. In the galactic disk this fraction tends to be higher than in the globular clusters. This clearly suggests an intimate link between the evolution of binary systems and the origin of millisecond pulsars. Another important characteristic is that the compantion stars of millisecond pulsars are almost consistently of low mass, with the most probable mass being $\lesssim 0.3 M_\odot$.

Pulsar ages are usually estimated by using $\dot{P}$. A simple spin down relation is assumed: $\dot{\nu} = K\nu^n$, where ν is the rotation frequency and n is the braking index. If the energy loss is due to radiation from a dipolar magnetic field, we can put $n = 3$, and we get for the so-called spin down age of the pulsar [9]

$$\tau = -\frac{P}{2\dot{P}} \tag{5.2}$$

The typical values of the spin-down age for a radio pulsar is $\sim 10^7$ yr, while the corresponding value for millisecond pulsars exceeds 10^9 yr. This gives an indication that the millisecond pulsars are indeed very old objects. The abundant occurrence of millisecond pulsars in globular clusters is in itself one such indication, since the massive stars capable of producing neutron star remnants existed only in the early phase of evolution of globular clusters.

We have seen that given enough time, the pulsar spin rate in an accretion X-ray pulsar will achieve an equilibrium period given by (4.79) along the spin-up line. We can rewrite this, approximating $96/211 \sim 3/7$ and $180/211 \sim 5/7$ we get

$$P_{eq} = 1.9\, B_9^{6/7}\, \dot{m}^{-3/7}\, \mathrm{ms} \tag{5.3}$$

where B_9 is the surface dipole field in units of 10^9 G. If $\dot{m}$ generally stays near unity (Eddington accretion rate), then for a neutron star to be spun-up to periods as short as milliseconds, its surface magnetic field must necessarily be low $\lesssim 10^9$ G. In all observed millisecond pulsars this is the case.

If we look at the definition of the corotarion radius r_{co}, we can put (with $M = 1.4 M_\odot$)

$$r_{co} \simeq 1.66 \cdot 10^6\, P^{2/3}\mathrm{m} \tag{5.4}$$

This gives $r_{co}(P = 10^{-3}\mathrm{s}) \simeq 10^4$ m, which is very close to the neutron star radius R. The corotation radius r_{co} will therefore be very close to the neutron star surface for such high spin frequencies. Thus the validity of (5.3) becomes highly questionable, since we have assumed that effects related to the surface of the neutron star can be neglected in the description of the disk/magnetosphere interaction.

5.1.1 Log B vs. Log P-plot

In Fig. 5.1 we can see data for a number of radio pulsars in a Log B vs. Log $\dot{P}$ plot. The magnetic fields are all estimated according to (5.1). The spin-up line (4.82) is the upper line in the figure. As we have seen, it represents the minimum period to which a neutron star can be spun up in an Eddington-limited accretion. The lower line show the so-called death line for pulsars. It corresponds to a polar cap voltage below which the pulsar activity is likely to switch off, and the neutron star will not be readily observable.

The essence here is how the pulsars are aligned along (but below) the spin-up line, stretching from the large volume of regular pulsars (called the pulsar island) towards the millisecond region in the bottom left corner. We see two somewhat anomalous pulsars in the chart, the one plotted as a square is actually the Crab pulsar. It represents the small body of very young pulsars ($\tau \lesssim 10^4$ yr), that have both a high spin and a significant magnetic field. Another anomaly (seen as a circle to the top right), is the magnetar *SGR 1900+14* with a very high magnetic field but with a relatively slow spin. The graveyard below the deathline should also be filled with pulsars, but they are not observable to us, and therefore do not appear in the chart.

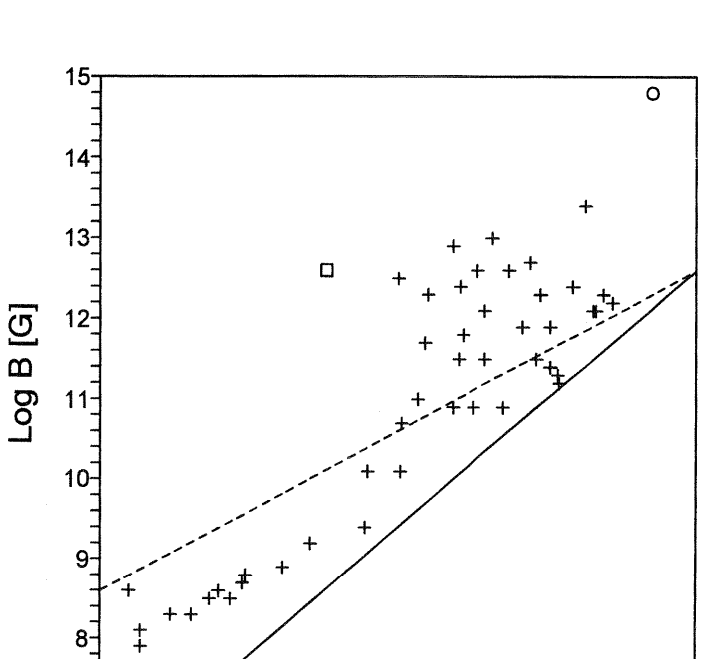

Fig. 5.1 *We see a number of radio pulsar data, collected from the ATNF pulsar catalogue. The upper line is the spin-up line, while the lower line indicates the region where radio pulses are assumed to disappear.*

Millisecond pulsars that have very low magnetic fields (and therefore are assumed to be old) are sometimes referred to as *recycled pulsars*. This is to distinguish them from very young pulsars that also might exhibit pulses in the millisecond region. Some old pulsars that belongs to the pulsar graveyard (below the death line) have magnetic fields that are quite low, and very slow rotation. If these objects for some reason enter an accretion phase, they could be spun up to millisecond spin periods (thus becoming observable in the radio spectrum again) and are therefore in a sense revitalized (or recycled). In this case the magnetic field of the old neutron star is already quite low when accretion starts.

5.1.2 Connection to LMXB

Even if the condition of low magnetic field and a near-Eddington accretion rate is fulfilled, the neutron star may still not achieve millisecond status unless the accretion phase lasts long enough. We can put the maximum rate of angular momentum accretion equal to the product of the accretion rate, and the specific Keplerian angular momentum at the magnetospheric boundary. At this rate of angular momentum enhancement, the neutron star could reach the equilibrium point P_{eq} after a total mass of

$$\Delta M \sim 0.1 M_{\odot} \left(\frac{P_{eq}}{1.5\,\mathrm{ms}} \right)^{-4/3} \tag{5.5}$$

has been accreted [8]. At the Eddington rate we can put $\dot{M} \sim 10^{-8} M_{\odot}\,\mathrm{yr}^{-1}$, and with $P_{eq} = 1.5$ ms we have an estimated millisecond spin-up time at $\gtrsim 10^7$ yr.

If the donor star has a mass well above the mass of the neutron star (HMXB), such a long ($\gtrsim 10^7$ yr) duration of heavy mass transfer is very unlikely to occur. Soon after the beginning of the Roche lobe overflow, mass transfer would become unstable, and a steady flow of matter at Eddington-level would not be possible. In LMXB, as mass transfer proceeds, the orbit tends to expand, keeping the mass transfer stable. Also, the time that heavy O and B-stars spend as stable stars are too short for these systems to act as progenitors to millisecond pulsars. The very slow evolution of the donor star in LMXB insures that ample time ($\sim 10^9$ yr) is available for the pulsar to reach the millisecond regime. It is established that the magnetic field of pulsars in LMXB are lower (by a factor of ~ 100) than in HMXB, so that clear pulses are seen more often in HMXB than in LMXB. This can be explained by the fact that LMXB have much longer accretion time scales, and therefore that the accretion induced field decay has longer time to operate.

The evolution of these LMXB systems can take on basically three different directions after the accretion has stopped:

- It may leave a relatively wide binary with a circular orbit, consisting of a low mass white dwarf ($0.2 - 0,4\,M_{\odot}$) and a millisecond pulsar. In this cass the mass of the donor star is not high enough ($M_d \lesssim 1.5\,M_{\odot}$) to produce a supernova, and thereby another neutron star. The value $M_d \lesssim 1.5\,M_{\odot}$ is used instead of the Chandrasekhar limit, because the accretion phase would typically steal about $0.1\,M_{\odot}$ from the donor.

- There is also the possibility that the pulsar (now turned millisecond pulsar) has evaporated the donor star, or possibly has merged with it, This would leave a non-binary millisecond pulsar left, most likely with no trace of the binary nature of the original system left.

- If $M_d \gtrsim 1.5\,M_\odot$, then the donor star could evolve into a supernova. This would either disrupt the system, leaving two runaway pulsars with large velocities, or it could result in a double pulsar system like the Hulse-Taylor pulsar *PSR B1913+16*. These last possibilities also exists for HMXB systems, where $M_d \gtrsim 10\,M_\odot$.

The first binary millisecond pulsar discovered, namely *PSR 1953+29* fits this description perfectly. Its 117 day orbital period, near perfect circular orbit ($e \sim 3 \cdot 10^{-4}$) and low mass companion $\sim 0.3\,M_\odot$, are all as expected for a LMXB spin-up endproduct. The initial period of the system would have been $\sim$ 12 days, and with the average mass transfer rate estimated to a little below Eddington-rate, the spin period is $P = 6.3$ ms. Several other of the charted binary millisecond pulsars show the same consistency with the above mentioned scenarios.

Several systems containing a millisecond pulsar and a white dwarf also exists. Quite recently, in the binary system PSR *J1909-3744*, the first measurements of the mass of a millisecond pulsar have been conducted, giving a mass very close to the Chandrasekhar limit [73].

5.2 Accreting X-ray Millisecond Pulsars

The discovery of the accreting X-ray millisecond pulsar *SAX J1808.4-3658* in 1998, is by many considered as a clinching argument that pulsar LMXB systems are the precursors of millisecond pulsars. Direct proof in the sense of direct observation and measurements on such a system (caught in the act, one might say) where missing until the 1998 discovery. The *SAX J1808.4-3658* pulsar is spinning with a period of only $P = 2.494$ ms, and with an orbital period of only $P_{orb} = 2.01$ h. In the following years several other similiar millisecond pulsars where discovered. A table of data is given for these objects in Appendix D. We see that the *XTE J1807-294* pulsar has the shortest orbital period of these objects, with a period of only $\sim$ 40 min. This gives an orbiting radius of only $\sim 10^5$ km, and an orbiting velocity of $\gtrsim c/1000$. The binary would fit well inside the Earth-Moon system.

In addition to their ultra short spin period, they all have the following similiar characteristics

- All are transient sources, that undergo outbursts of X-ray activity lasting days or weeks, and then return to an inactive (quiescent) state that may last in the order of months or even years.

- They all have low magnetic fields of the order $10^8 - 10^9$ G. Thus, like for most LMXB sources, the emitted X-ray pulses are faint and very hard to detect, even when the sources are in an active period.

- During outburst all of the sources are low luminosity sources, indicating mass transfer rates that are significantly below Eddington rates.
- All are X-ray burst sources (see Chapter 3.5.4 for a discussion). This is consistent with their low magnetic field strenghts, since X-ray burst models rely on low pulsar magnetic fields to operate.
- Their companions are all faint low mass stars. This underlines the link between such systems and LMXB.

In the case of the source *XTE J1751-305*, a brown dwarf star has been identified as a possible donor star. Brown dwarf stars are faint versions of red dwarf stars, and this particular star has a mass that is only about 15 Jupiter masses, or only $\sim 0.015\, M_\odot$. Its original mass must however have been much higher, so the pulsar has more or less slowly devoured its donor star during an accretion phase that probably has lasted for $\sim 10^9$ yr (if we assume a persistent low accretion rate), and is still going on today. It is thus likely that many of these sources will be observable as isolated millisecond pulsars in the far future.

The transient nature of these objects may be connected to the fact that the corotation radius r_{co} and also the disruption radius r_0 lie very close to the neutron star surface. If the accretion disk persists down to the surface of the star, detectable pulses might not arise, since no field channeling takes place. Thus for typical system parameters associated with the millisecond X-ray pulsars, r_0 might have to lie within a rather restricted range for pulses to be detected. A range of 3-4 in r_0 corresponds to a range in $\dot{M}$ of about a factor of 100 (see (4.42)). However, the observed range in X-ray luminosity, and presumeably also in $\dot{M}$, is of order a factor $\gtrsim 50$ for at least three of the millisecond pulsars. Thus, in the standard accretion paradigm, the magnetic field and the values of $\dot{M}$ would have to be in just the correct range to allow accretion to continue throughout the outburst. If the $\dot{M}$ value changes to a value outside of this range, the source will turn off.

Bibliography

[1] Shklovski I.S. (1967)
Astron. Zhur. **44,** 930.
(English translation in *Sov. Astron. Astrophys. J.* **15,** 377.)

[2] Cameron A.G. & Mock M. (1967)
Nature **215,** 464.

[3] Prendergast K.H. & Burbridge G.R. (1968)
Astrophys. J. Lett. **151,** L83.

[4] Gold T. (1968)
Nature **218,** 731.

[5] Tananbaum H. *et al.* (1972)
Astrophys. J. Lett. **174,** L143.

[6] Nelson R. *et al.* (1996)
Bull. Am. Astron. Soc. **28**, 1425.

[7] Rappaport S.A. & Joss P.C. (1983)
in *"Accretion-driven Stellar X-ray Sources"*
(Eds: Lewin W.H.G. & Van den Heuvel E.P.J.)
Cambridge University Press

[8] Bhattacharya D. (1995)
in *"X-ray Binaries"*
(Eds.: Lewin W.H.G., Van Paradijs J. & Van den Heuvel E.P.J.)
Cambridge University Press

[9] Stella L. *et al.* (2000)
Astrophys. J. **537,** L115

[10] Shapiro S.L. & Teukolsky S.A. (1983)
in *"Black Holes, White Dwarfs and Neutron Stars"*
Wiley-Interscience

[11] Bahcall J.N. (1978)
in *"Physics and Astrophysics of Neutron Stars and Black Holes"*
(Eds.: Giacconi R. & Ruffini R.)
North Holland

[12] Lynden-Bell D. (1969)
Nature **223**, 690.

[13] Steeghs D. *et al.* (1997)
MNRAS **290,** L28.

[14] Frank J., King A. & Raine D. (1992)
in *"Accretion Power in Astrophysics"* 2^{nd} ed.
Cambridge University Press

[15] Blondin J.M., Stevens I.R. & Kallman T.R. (1991)
Astrophys. J. **371**, 684.

[16] Van den Heuvel E.P.J. (1983)
in *"Accretion-driven Stellar X-ray Sources"*
(Eds.: Lewin W.H.G. & Van den Heuvel E.P.J.)
Cambridge University Press

[17] Iben Jr. I., Tutukov A.V. & Fedorova A.V. (1997).
Astrophys. J. **486,** 955.

[18] Leitherer C., Robert C. & Drissen L. (1992)
Astrophys. J. **401,** 596.

[19] Van Paradijs J. & McClintock J.E. (1995)
in "*X-ray Binaries*"
(Eds.: Lewin W.H.G., Van Paradijs J. & Van den Heuvel E.P.J.)
Cambridge University Press

[20] Shakura N.I. (1972)
Astron. Zhur. **49**, 291.

[21] Pringle J.E. & Rees M.J. (1972)
Astron. & Astrophysics **21**, 1.

[22] Shakura N.I. & Sunyaev R.A. (1973)
Astron. & Astrophysics **24**, 337.

[23] Landau L.D. & Lifshitz E.M. (1959)
in "*Fluid Mechanics*"
Pergamon Press

[24] Lynden-Bell D. & Pringle J.E. (1974)
MNRAS **168**, 403

[25] Chen F. (1984)
in "*Introduction to Plasma Physics And Controlled Fusion*" 2^{nd} ed.
Plenum Press

[26] Bath G.T. & Pringle J.E. (1981)
MNRAS **194**, 967.

[27] Balbus S.A. & Hawley J.F. (1998)
Reviews of Modern Physics **70**, 1.

[28] Tayler R.J. (1980)
MNRAS **191,** 135.

[29] Kato S., Fukue J. & Mineshige S. (1998)
in "*Black-Hole Accretion Disks*"
Kyoto University Press

[30] Osaki Y. (1999)
in *"Disk Instabilities in Close Binary Systems"*
(Eds.: Mineshige S. & Wheeler J.C.)
Universal Academy Press, Inc.

[31] Chandrasekhar S. (1960)
in "*Radiative Transfer*"
Dover Publishing, Inc.

[32] In 't Zand J.J.M. *et al.* (1998)
Astron. & Astrophysics **331,** L25.

[33] Gerend L. & Boynton P.E. (1976)
Astrophys. J. **209,** 562.

[34] Jones C.A. & Forman W. (1976)
Astrophys. J. Lett. **209,** L131.

[35] Petterson J.A., Rothschild R.E. & Gruber D.E. (1991)
Astrophys. J. **378,** 696.

[36] Pringle J.E. (1976)
MNRAS **177,** 65.

[37] Piran T. (1978)
Astrophys. J. **221,** 652.

[38] Novikov I.D. & Thorne K.S. (1973)
in "*Black Holes*"
(Eds.: DeWitt C. & DeWitt B.)
Gordon & Breach

[39] Rybicki G.B. & Lightman A.P. (1979)
in "*Radiative Processes in Astrophysics*"
John Wiley & Sons

[40] Lyutyi V.M. & Syunyaev R.A. (1976)
Soviet Astronomy **20,** 652.

[41] Becker R.H. *et al.* (1977)
Astrophys. J. **214,** 879.

[42] Shapiro S.L., Lightman A.P. & Eardley D.M. (1976)
Astrophys. J. **204,** 187.

[43] Petterson J.A. (1980)
Astrophys. J. **241,** 247.

[44] Abramowics M.A., Xu C. & Lasota J.P. (1986)
in "*Quasars: Proceedings of the IAU Symposium, Bangalore, India, Dec.2-6, 1985*"
D. Reidel Publishing Co.

[45] Collins R.E. (1999)
"*Mathematical Methods for Physicists and Engineers*"
Dover Publications, Inc.

[46] Lesur G. & Longaretti P.Y. (2006)
in "*Proceedings of the Annual meeting of the French Society of Astronomy and Astrophysics (SF2A-2006)*"
(Eds.: Barret D., Casoli F., Lagache G., Lecavelier A., Pagani L.)
IfA Publications

[47] Stone J.M. & Pringle J.E. (2001)
MNRAS **322,** 461.

[48] Thorsett S.E. & Chakrabarty D. (1999)
Astrophys. J. **512,** 288.

[49] Pons A. *et al.* (2002)
Astrophys. J. **564,** 981.

[50] Goldreich P. & Julian W.H. (1969)
Astrophys. J. **157,** 869.

[51] Xu R.X., Cui X.H. & Qiao G.J. (2006)
Chin. J. Astron. & Astrophys. **6,** 217.

[52] Ghosh P. & Lamb F.K. (1977)
Astrophys. J. **217,** 578.

[53] Ghosh P. & Lamb F.K. (1979)
Astrophys. J. **232,** 259.

[54] Ghosh P. & Lamb F.K. (1979)
Astrophys. J. **234,** 296.

[55] Lamb F.K. (1989)
in "*Timing Neutron Stars*"
(Eds.: Ögelman H. & Van den Heuvel E.P.J.)
Kluwer Academic Publishers

[56] Spruit H.C. & Taam R.E. (1990)
Astron. & Astrophysics **229**, 475.

[57] Ghosh P. & Lamb F.K. (1978)
Astrophys. J. **223,** L83.

[58] Stella L. & Rosner R. (1984)
Astrophys. J. **277,** 312.

[59] Romanova M.M. *et al.* (2004)
Astrophys. J. **616,** L151.

[60] Casse F. & Ferreira J. (2000)
Astron. & Astrophysics **361,** 1128.

[61] Li J., Wickramasinghe D.T. & Rüdiger G. (1996)
Astrophys. J. **469,** 696.

[62] Li X.D. & Wang Z.R. (1996)
Astron. & Astrophysics **307,** L5.

[63] Wang Y.M. (1995)
Astrophys. J. **449,** L153.

[64] Lorimer D.R. (2005)
Living Reviews in Relativity **8,** 7.

[65] Bildsten L. *et al.* (1997)
Astrophys. J. Supp.Series **113,** 367.

[66] Bogdanov S. *et al.* (2004)
Astrophys. J. **646,** 1104.

[67] Wijnands R. (2005)
eprint arXiv:astro-ph/0501264

[68] ATNF Pulsar Catalogue (2007)
http://www.atnf.csiro.au
Australia Telescope National Facility

[69] Poutanen, J. (2006)
Advances in Space Research **38,** 2697.

[70] Konar S. & Choudhuri A.R. (2002)
Bull. Astron. Soc. India **30,** 697.

[71] Wang Y.M. & Robertson J.A. (1985)
Astron. & Astrophysics **151,** 361.

[72] Elsner R.F. & Lamb F.K. (1977)
Astrophys. J. **215,** 897.

[73] Jacoby B.A. *et al.* (2005)
Bull. Am. Astron. Soc. **37,** 1468.

Appendix A

Radiative Transport

In this appendix I have assembled some of the basic procedures regarding the transport of radiation in a gaseous medium, with an emphasis on the equations we need in standard accretion disks. There are many thorough treatments on the subject, among the best is possibly the one by Chandrasekhar [31].

A.1 The Radiative Transfer Equation

One often starts with constructing the quantity I_ν, called the specific intensity, so that $I_\nu(\boldsymbol{r}, \boldsymbol{n}, t)\, d\nu\, d\Omega$ represents the photon energy in the interval ν to $\nu + d\nu$ passing per unit time through a unit area with normal $\boldsymbol{n}$ into the solid angle $d\Omega$ about $\boldsymbol{n}$. The radiation field is thus fully specified by I_ν. Associated with I_ν are the specific energy density at $\boldsymbol{r}$

$$\epsilon_\nu^r(\boldsymbol{r}, t) \equiv \frac{1}{c} \int I_\nu \, d\Omega \tag{A.1}$$

and the vector function

$$\boldsymbol{F}_\nu(\boldsymbol{r}, t) \equiv \int I_\nu \cdot \boldsymbol{n} \, d\Omega \tag{A.2}$$

measures the specific flux along the direction $\boldsymbol{n}$. The total intensity, energy density and flux are obtained by integrating their monochromatic counterparts over frequency. For the special case of local thermodynamic equilibrium at temperature T, I_ν is given by the well known Planck function (or distribution)

$$I_\nu = B_\nu = \frac{2h\nu^3}{c^2} \frac{1}{e^{h\nu/kT} - 1} \tag{A.3}$$

We also have $\epsilon_\nu^r = \epsilon_\nu^P = 4\pi B_\nu / c$, and $\epsilon_r = \epsilon_P = aT^4$, where a is the usual radiation density constant and P denotes Planck. Consider now the emission and absorption of photons in a gaseous medium. Define the emission coefficient, or *emissivity* $j_\nu(\boldsymbol{r}, \boldsymbol{n}, t)$ so that $j_\nu\, d\nu\, d\Omega$

is the spontaneous energy emission rate per unit volume in the interval ν to $\nu + d\nu$ and in the solid angle $d\Omega$ about $\boldsymbol{n}$ at time t. Likewise define the absorption coeffisient, or *opacity*, $\kappa_\nu(\boldsymbol{r}, \boldsymbol{n}, t)$ so that $\kappa_\nu \rho I_\nu \, d\nu \, d\Omega$ gives the corresponding energy absorbed per unit volume per unit time from a beam of given intensity I_ν (thus κ_ν is measured in $m^2\, kg^{-1}$). Assuming that photons travel in straight lines in the medium, the total change in I_ν in a distance ds, measured along a light ray in the direction $\boldsymbol{n}$ equals

$$\frac{1}{c}\frac{\partial I_\nu}{\partial t} + \boldsymbol{n} \cdot \boldsymbol{\nabla} I_\nu = j_\nu - \kappa_\nu \rho \, I_\nu \tag{A.4}$$

where local changes in both distance and time are included. This is known as the *equation of radiative transfer*. For many circumstances, including local thermodynamical equilibrium, j_ν and κ_ν assume the same relative values that they would have in strict thermodynamic equilibrium, when $I_\nu = B_\nu = \text{constant}$. In this situation, the left-hand side of the equation of radiative transfer must vanish, giving

$$\frac{j_\nu}{\kappa_\nu \rho} = B_\nu(T) \tag{A.5}$$

where T is the local matter temperature. This equation is known as *Kirchoff's law* and expresses the detailed balance that must prevail between absorption and emission in thermodynamic equilibrium.

If we insert Kirchoff's law into the (A.4) we get

$$\frac{1}{c}\frac{\partial I_\nu}{\partial t} + \boldsymbol{n} \cdot \boldsymbol{\nabla} I_\nu = \kappa_\nu \, \rho \, (B_\nu - I_\nu) \tag{A.6}$$

If we integrate this over $d\Omega$, and employ (A.1) and (A.2) and $\epsilon_\nu^r = 4\pi B_\nu / c$ we get

$$\frac{\partial \epsilon_\nu^r}{\partial t} + \boldsymbol{\nabla} \boldsymbol{F}_\nu = c \kappa_\nu \rho \, (\epsilon_\nu^P - \epsilon_\nu^r) \tag{A.7}$$

Here we have assumed that κ_ν is isotropic. Equation (A.7) is essentially an equation of continuity for radiation of a given frequency, including sources and sinks of radiation. A formal solution to the equation of radiative transfer can be obtained by assuming that those functions depending upon the local thermodynamic state of the gas (such as for example B_ν and κ_ν are known functions of space and time. If we assume steady-state (ignoring time derivatives), then (A.6) may be regarded as an ordinary differential equation for I_ν along the direction of propagation

$$\frac{dI_\nu}{ds} = \kappa_\nu \rho \, (B_\nu - I_\nu) \tag{A.8}$$

where it is natural to define the *optical depth* τ_ν along the propagation direction as $d\tau_\nu \equiv \kappa_\nu \rho \, ds$.

The equation of radiative transport simplifies considerably when the radiation field is only weakly anisotropic. If we multiply (A.6) with $\boldsymbol{n}$ and then integrate over all angles (noting that $\kappa_\nu \rho B_\nu$ is independent of direction, and so does not contribute to the integral), while using the definition (A.2) for $\boldsymbol{F}_\nu$ we get

$$\frac{1}{c}\frac{\partial \boldsymbol{F}_\nu}{\partial t} + \int \boldsymbol{n}\,(\boldsymbol{n}\cdot\boldsymbol{\nabla} I_\nu)\, d\Omega = -\kappa_\nu \rho \boldsymbol{F}_\nu \tag{A.9}$$

We can next assume that the radiation may be treated as quasisteady at each instant of time, in which case (A.9) reduces to

$$\int \boldsymbol{n}\,(\boldsymbol{n}\cdot\boldsymbol{\nabla} I_\nu)\, d\Omega = -\kappa_\nu \rho \boldsymbol{F}_\nu \tag{A.10}$$

(A.10) remains valid even if the radiation field changes with time, provided the changes are sufficiently slow that they may be described completely through the time variation of the gas temperature and density. It is possible to evaluate the left-hand side of (A.10) by keeping leading-order parts of the expression. If this is done (see for instance [10]) we get

$$\boldsymbol{F}_\nu = -\frac{c}{3\kappa_\nu \rho}\nabla \epsilon_\nu^r \tag{A.11}$$

Taken together with (A.7) in the quasisteady limit

$$\boldsymbol{\nabla} \boldsymbol{F}_\nu = c\kappa_\nu \rho\,(\epsilon_\nu^P - \epsilon_\nu^r) \tag{A.12}$$

(A.11) and (A.12) constitute the *diffusion approximation* to the radiative transport equations. This approximation is valid whenever the radiation field is isotropic over distances comparable to, or less than a radiation mean free path $\lambda_\nu \equiv 1/\kappa_\nu \rho$.

A.1.1 Frequency Integrated Radiation Flux

Let us now assume that local thermodynamic equilibrium holds and consider the frequency-integrated version of (A.11). Given local thermodynamic equilibrium we can set $\epsilon_\nu^r = \epsilon_\nu^P$, so that on integrating over ν we obtain the integrated radiative flux

$$\boldsymbol{F} = -\frac{c}{3\rho}\int_0^\infty \frac{1}{\kappa_\nu}\nabla \epsilon_\nu^P \, d\nu \tag{A.13}$$

In light of this we define an average opacity, the *Rosseland mean opacity* $\bar{\kappa}$, by

$$\frac{1}{\bar{\kappa}} \equiv \frac{\int_0^\infty \frac{1}{\kappa_\nu} \frac{d\epsilon_\nu^P}{dT} d\nu}{\int_0^\infty \frac{d\epsilon_\nu^P}{dT} d\nu} \tag{A.14}$$

Then we can rewrite (A.13) to become

$$\boldsymbol{F} = -\frac{c}{3\bar{\kappa}\rho} \nabla \epsilon_P = -\frac{c}{3\bar{\kappa}\rho} \nabla (aT^4) = -\frac{4acT^3}{3\bar{\kappa}\rho} \nabla T \tag{A.15}$$

which is the frequency integrated radiation flux we wanted.

A.1.2 Optical Depth

Optical depth is a measure of transparency, and is defined as the fraction of radiation (or light) that is scattered or absorbed on a path. One way of visualizing optical depth is to think of a fog. The fog between you and an object that is immediately in front of you has an optical depth of zero. As the object moves away, the optical depth increases until it reaches a large value and the object is no longer visible.

For accretion disk purposes we can express the the optical depth τ as

$$\tau = \int_0^H \bar{\kappa}\rho \, dz = \frac{\bar{\kappa}\Sigma}{2} \tag{A.16}$$

which we will use in the disk models. In light of the above it is clear that we can define a gas to be *optically thick* if $\tau \gg 1$. In this case practically all radiation will be absorbed or scattered on it's way through the medium. If this is the case, and absorption dominates scattering, the gas will have a blackbody spectrum emission at all local points. Likewise we can define the gas to be *optically thin* to outgoing photons if $\tau \ll 1$. In this case photons can escape freely from their point of emission without ever undergoing absorption or scattering.

Sometimes the *effective optical depth* for absorption τ^* is used. The same definitions for optical thick ($\tau^* \gg 1$) or optical thin ($\tau^* \ll 1$) applies. We define [9]

$$\tau^* = \begin{cases} \left(\sqrt{\kappa_{ff}\kappa_{es}}\right) \rho H & \kappa_{ff} < \kappa_{es} \\ \left(\kappa_{ff}\right) \rho H & \kappa_{ff} > \kappa_{es} \end{cases}$$

A.2 Opacity Sources

Radiative transport in plasmas is governed by several different opacity sources. Which, and if, one source dominates depends on the thermodynamic state of the gas, that is on ρ and T. For the thermodynamic parameters that govern the Shakura-Sunyaev model we

assume that two different types of opacity will contribute, and which will be dominant in different regions of the disk.

A.2.1 Inverse Bremsstrahlung

This is the absorption of photons by free electrons in the presence of positive ions (in this case protons). The mean Rosseland opacity $\bar{\kappa}_{ff}$ of free-free absorption in this plasma is [38]

$$\bar{\kappa}_{ff} = \kappa_0 \rho T^{-7/2} \tag{A.17}$$

where $\kappa_0 = 7.5 \cdot 10^{19}\,\mathrm{m^5\,kg^{-2}\,K^{7/2}}$. Any opacity that varies in this way is called a *Kramers opacity*. If the gas is not completely ionized, there may be other comparable (but smaller) contributions to absorption from "bound-bound" line transitions and "bound-free" ionization transitions, but these will contribute (if at all) only in the very outer regions of the disk.

A.2.2 Scattering from Free Electrons

The major source to photon scattering is Thompson scattering. The scattering cross-section for protons is a factor $(m_e/m_p)^2 \approx 2.5 \cdot 10^{-7}$ smaller, so we will not include this. The cross section σ_T is given by the Thompson formula $\sigma_T = (8\pi/3)(e^2/m_e c^2)^2$. The scattering is elastic, and since it is also frequency independent, the Rosseland mean opacity $\bar{\kappa}_{es}$ becomes a constant

$$\bar{\kappa}_{es} = 0.038\,\mathrm{m^2\,kg^{-1}} \tag{A.18}$$

A.2.3 Comptonization

Comptonization is the process by which photons can gain or lose energy by scattering off thermal electrons. The process has proven to be somewhat significant for the generation of hard X-rays emitted from the very hot inner regions of accretion disks, especially optically thin advection dominated flows around black holes. We sometimes use the y-parameter to describe the regime of Comptonization [39]

$$y = \begin{cases} \frac{4kT}{m_e c^2}\tau_{es} & \tau_{es} \leq 1 \\ \frac{4kT}{m_e c^2}\tau_{es}^2 & \tau_{es} > 1 \end{cases}$$

where the first factor approximates the energy increases per scattering (for $h\nu < 4kT$), and the second factor represents the mean number of scatterings. For $y \gg 1$, coherent (Thompson) scattering is important. When $y \ll 1$ however, Comptonization becomes important.

Appendix B

Solution of the Linear Diffusion Equation for $\bar{\nu} = \bar{\nu}(r)$

For a Keplerian disk, we have the diffusion equation (3.23)

$$\frac{\partial \Sigma}{\partial t} = \frac{3}{r}\frac{\partial}{\partial r}\left[r^{1/2}\frac{\partial}{\partial r}\left(\nu \Sigma r^{1/2}\right)\right] \tag{B.1}$$

subject to $r^{1/2}\bar{\nu}\Sigma = 0$ at $r = 0$. We will consider the linear case for which $\nu = \nu(r)$. In this case, the general solution may be found as a linear superposition of elementary solutions. One may look for solutions in the conventional way, in which the variables are separated

$$\Sigma = r^{\beta}\sigma(r)e^{-\lambda t} \tag{B.2}$$

Here λ is a positive real number, representing the decay rate of the mode. β is a free parameter to be chosen at our convenience. Then

$$-\lambda r^{\beta}\sigma = \frac{3}{r}\frac{d}{dr}\left[r^{1/2}\frac{d}{dr}(r^{\beta+1/2}\bar{\nu}\sigma\right] \tag{B.3}$$

Suppose that $\bar{\nu}$ is constant, then

$$r^2\frac{d^2\sigma}{dr^2} + \left(2\beta + \frac{3}{2}\right)r\frac{d\sigma}{dr} + \beta\left(\beta + \frac{1}{2}\right)\sigma + \frac{\lambda}{3\bar{\nu}}r^2\sigma = 0 \tag{B.4}$$

Choose $\beta = -1/4$ for convenience. Then

$$r^2\frac{d^2\sigma}{dr^2} + r\frac{d\sigma}{dr} + \left(k^2r^2 - \frac{1}{16}\right)\sigma = 0 \tag{B.5}$$

where $k^2 = \lambda/(3\bar{\nu})$. This is *Bessel's equation* of order $1/4$. The general solution is

$$\sigma = A\,J_{1/4}(kr) + B\,Y_{1/4}(kr) \tag{B.6}$$

For small r, the Bessel functions behave as

$$J_{1/4}(kr) \propto r^{1/4} \qquad Y_{1/4}(kr) \propto r^{-1/4} \tag{B.7}$$

so that in light of the boundary value we put $B = 0$, and the solution with vanishing torque at $r = 0$ is then

$$\Sigma \propto r^{-1/4} J_{1/4}(kr)\, e^{-3\bar{\nu}k^2 t} \tag{B.8}$$

If we consider the more general initial-value problem, we resolve the initial surface density into Bessel functions

$$\Sigma(r,0) = \int_0^\infty f(k)\, r^{-1/4} J_{1/4}(kr)\, dk = \delta(r - r_0) \tag{B.9}$$

The general solution is then found by

$$\Sigma(r,t) = \int_0^\infty f(k)\, r^{-1/4} J_{1/4}\, e^{-3\bar{\nu}k^2 t}\, dk \tag{B.10}$$

If we recall the properties of *Hankel transforms*

$$\begin{aligned} A(r) &= \int_0^\infty a(k) J_\nu(kr) k^{1/2} r^{1/2}\, dk \\ a(k) &= \int_0^\infty A(r) J_\nu(kr) k^{1/2} r^{1/2}\, dk \end{aligned} \tag{B.11}$$

where ν is the order of the Bessel functions used, we may write

$$r^{3/4}\, \Sigma(r,0) = \int_0^\infty k^{-1/2} f(k) J_{1/4}(kr) k^{1/2} r^{1/2}\, dk \tag{B.12}$$

and the inverse is then

$$k^{-1/2} f(k) = \int_0^\infty s^{3/4}\, \Sigma(s,0) J_{1/4}(ks) k^{1/2} s^{1/2}\, ds \tag{B.13}$$

The general solution may then be written in the form

$$\Sigma(r,t) = \int_0^\infty G(r,s,t)\, \Sigma(s,0)\, ds \tag{B.14}$$

and where

$$G(r,s,t) = r^{-1/4} s^{5/4} \int_0^\infty J_{1/4}(kr) J_{1/4}(ks)\, k e^{-3\bar{\nu}k^2 t}\, dk \tag{B.15}$$

is a *Green function*. This may be evaluated explicitly as [45]

$$G(r,s,t) = \frac{r^{-1/4}s^{5/4}}{6\bar{\nu}t} I_{1/4}\left(\frac{rs}{6\bar{\nu}t}\right) e^{-\frac{(r^2+s^2)}{12\bar{\nu}t}} \tag{B.16}$$

where I_ν is a modified Bessel function. Inserted into (B.14) with the δ-function boundary value condition, and integrated over s, returns our analytical solution (3.25).

Appendix C

Magnetohydrodynamics (MHD)

The theory of magnetohydrodynamics (MHD) describes the fluid mechanics of plasmas and the behaviour of their magnetic fields. Maxwell's equations for the electromagnetic field are combined with the equations of hydrodynamics. For non-relativistic flow speeds, the magnetic force can be expressed as a function of the field $\boldsymbol{B}$ and its derivatives, and this dominates the electric force. The electric field and charge density can be eliminated from the equations, and so do not have to be explicitly considered. Faraday's law of induction is very important, and shows how $\boldsymbol{B}$ is affected and diffused by the fluid motions. Simplified forms of the equations can be used in some cases of course. If the diffusion time-scale is much longer than the flow time-scale, the magnetic field lines are frozen to the plasma. Material is therefore threaded onto field lines, which are advected and distorted by the flow. I here use SI versions of all equations and constants.

C.1 The Induction Equation

In addition to the two well known source equations $\boldsymbol{\nabla} \cdot \boldsymbol{E} = \rho_c/\epsilon_0$ and $\boldsymbol{\nabla} \cdot \boldsymbol{B} = 0$, we need

$$\boldsymbol{\nabla} \times \boldsymbol{E} = -\frac{\partial \boldsymbol{B}}{\partial t} \tag{C.1}$$

$$\boldsymbol{\nabla} \times \boldsymbol{B} = \mu_0 \boldsymbol{J} + \frac{1}{c^2}\frac{\partial \boldsymbol{E}}{\partial t} \tag{C.2}$$

where ρ_c is the charge density and $\boldsymbol{J}$ is the current density. The equations of non-relativistic MHD are derived using the condition $v \ll c$ and working to first order in v/c. Since $\boldsymbol{v}, \boldsymbol{B}$ and $\boldsymbol{E}$ are causally inter-related, a typical velocity is $v \sim \ell/\tau$, where ℓ and τ are the length and time-scales for $\boldsymbol{E}$ and $\boldsymbol{B}$. The induction equation (C.1) then gives

$$\frac{E}{B} \sim \frac{\ell}{\tau} \sim v \tag{C.3}$$

It therefore follows in (C.2) that

$$\frac{|\partial \boldsymbol{E}/\partial t|}{c^2\,|\boldsymbol{\nabla}\times\boldsymbol{B}|} \sim \frac{\ell E}{c^2 \tau B} \sim \left(\frac{v}{c}\right)^2 \ll 1 \tag{C.4}$$

so the displacement current can be neglected and we get

$$\boldsymbol{\nabla}\times\boldsymbol{B} = \mu_0 \boldsymbol{J} \tag{C.5}$$

If we use the current $\boldsymbol{J} = \sigma(\boldsymbol{E} + \boldsymbol{v}\times\boldsymbol{B})$, where σ is the electrical conductivity, with the above we get the induction equation

$$\boldsymbol{\nabla}\times(\boldsymbol{v}\times\boldsymbol{B}) - \boldsymbol{\nabla}\times(\eta\boldsymbol{\nabla}\times\boldsymbol{B}) = \frac{\partial \boldsymbol{B}}{\partial t} \tag{C.6}$$

with the magnetic diffusivity $\eta = 1/\mu_0\sigma$.

C.2 Magnetic Threading and Flux Tubes

In the case that $\eta \to 0$ (or $\sigma \to \infty$) the induction equation reduces to

$$\boldsymbol{\nabla}\times(\boldsymbol{v}\times\boldsymbol{B}) = \frac{\partial \boldsymbol{B}}{\partial t} \tag{C.7}$$

There are several ways of showing that in this limit the magnetic field is frozen to the plasma, so field lines are attached to fluid elements. One is to consider the magnetic flux through a contour C, this is given by

$$\Phi = \int_S \boldsymbol{B}\cdot d\boldsymbol{S} \tag{C.8}$$

where S is an open surface ending on C. If the contour is taken to always be composed of the same fluid elements, then conservation of Φ is consistent with the field being frozen to the plasma. Hence the material derivative Φ/dt should vanish if (C.7) is satisfied. We denote the contour at time t by C, and at time $t+\delta t$ by $\tilde{C}$. In the time interval δt an arc length $d\boldsymbol{l}$ of C sweeps out an area $d\boldsymbol{l}\times\boldsymbol{v}\delta t$. The surface consisting of the union of a surface S ending on C, a surface $\tilde{S}$ ending on $\tilde{C}$ and the band joining C and $\tilde{C}$ is a closed surface. The total flux through this closed surface at time $t+\delta t$ is

$$-\int_S \boldsymbol{B}(\boldsymbol{r}, t+\delta t)\cdot d\boldsymbol{S} + \int_{\tilde{S}} \boldsymbol{B}(\boldsymbol{r}, t+\delta t)\cdot d\tilde{\boldsymbol{S}} + \oint_C \boldsymbol{B}(\boldsymbol{r}, t+\delta t)\cdot(d\boldsymbol{l}\times\boldsymbol{v}\delta t) = 0 \tag{C.9}$$

The negative sign arises since the outward normal is required on S, and the total flux of $\boldsymbol{B}$ through any closed surface is zero since $\boldsymbol{\nabla} \cdot \boldsymbol{B} = 0$. The change in flux through the moving contour is therefore

$$\begin{aligned} \delta\Phi &= \int_{\tilde{S}} \boldsymbol{B}(\boldsymbol{r}, t+\delta t) \cdot d\tilde{\boldsymbol{S}} - \int_S \boldsymbol{B}(\boldsymbol{r}, t) \cdot d\boldsymbol{S} && \text{(C.10)} \\ &= \int_S [\boldsymbol{B}(\boldsymbol{r}, t+\delta t) - \boldsymbol{B}(\boldsymbol{r}, t)] \cdot d\boldsymbol{S} + \delta t \oint_C \boldsymbol{B}(\boldsymbol{r}, t) \cdot (\boldsymbol{v} \times d\boldsymbol{l}) && \text{(C.11)} \\ &= \delta t \left[\int_S \frac{\partial \boldsymbol{B}}{\partial t} \cdot d\boldsymbol{S} - \oint_C \boldsymbol{v} \times \boldsymbol{B} \cdot d\boldsymbol{l} \right] && \text{(C.12)} \end{aligned}$$

Dividing by δt, letting $\delta t \to 0$ and using Stokes' integral theorem, gives

$$\frac{\partial \Phi}{\partial t} = \int_S \left[\frac{\partial \boldsymbol{B}}{\partial t} - \boldsymbol{\nabla} \times (\boldsymbol{v} \times \boldsymbol{B}) \right] \cdot d\boldsymbol{S} \qquad \text{(C.13)}$$

Now (C.7) shows that $\partial\Phi/\partial t = 0$, which is consistent with frozen $\boldsymbol{B}$-fields.

Magnetic Flux Tubes

The concept of magnetic flux tubes will be useful to us. A flux tube is the volume enclosed by the set of field lines which intercept a simple closed curve. Since no field lines cross the surface of the tube, it follows from $\boldsymbol{\nabla} \cdot \boldsymbol{B} = 0$ that for any volume of it contained between two cross-sections, as much flux leaves as enters. Hence the flux Φ through the tube, given by (C.8) with $d\boldsymbol{S}$ having the same sense as $\boldsymbol{B}$, is constant. When $\eta \to 0$ (or $\sigma \to \infty$), matter can flow along flux tubes, but not across them.

C.3 Lorentz Force

The Lorentz force density on ions and electrons is

$$\boldsymbol{F} = n_i Ze(\boldsymbol{E} + \boldsymbol{v}_i \times \boldsymbol{B}) - n_e e(\boldsymbol{E} + \boldsymbol{v}_e \times \boldsymbol{B}) \qquad \text{(C.14)}$$

where n_i and n_e are the number densities of ions and electrons. This gives

$$\boldsymbol{F} = \rho_c \boldsymbol{E} + \boldsymbol{J} \times \boldsymbol{B} \qquad \text{(C.15)}$$

The ratio of the electric to magnetic force is

$$\frac{\rho_c |\boldsymbol{E}|}{|\boldsymbol{J} \times \boldsymbol{B}|} \sim \epsilon_0 \mu_0 \left(\frac{E}{B} \right)^2 \sim \left(\frac{v}{c} \right)^2 \qquad \text{(C.16)}$$

where the first relation follows from $\nabla \cdot \boldsymbol{E} = \rho_c/\epsilon_0$ and (C.5), and the second from (C.3). The electric force density is therefore negligible so

$$\boldsymbol{F} = \boldsymbol{F}_m = \boldsymbol{J} \times \boldsymbol{B} \tag{C.17}$$

and use of (C.5) then gives

$$\boldsymbol{F}_m = \frac{1}{\mu_0}(\nabla \times \boldsymbol{B}) \times \boldsymbol{B} \tag{C.18}$$

Now employing the identity

$$\nabla(\boldsymbol{F} \cdot \boldsymbol{G}) = (\boldsymbol{F} \cdot \nabla)\,\boldsymbol{G} + (\boldsymbol{G} \cdot \nabla)\,\boldsymbol{F} + \boldsymbol{F} \times (\nabla \times \boldsymbol{G}) + \boldsymbol{G} \times (\nabla \times \boldsymbol{F}) \tag{C.19}$$

(C.18) can be written

$$\boldsymbol{F}_m = \frac{1}{\mu_0}(\boldsymbol{B} \cdot \nabla)\boldsymbol{B} - \nabla\left(\frac{B^2}{2\mu_0}\right) \tag{C.20}$$

Hence $\boldsymbol{F}_m$ can be expressed in the Cartessian tensor form

$$F_{mi} = \frac{\partial M_{ij}}{\partial x_j} \tag{C.21}$$

where the summation convention is used, and

$$M_{ij} = \frac{1}{\mu_0} B_i B_j - \frac{B^2}{2\mu_0}\delta_{ij} \tag{C.22}$$

is the Maxwell stress tensor. The $B_i B_j/\mu_0$ term represents a tension along the magnetic field, while $B^2/2\mu_0$ can be interpreted as a pressure. Writing $\boldsymbol{B} = B\hat{\boldsymbol{s}}$ and $\hat{\boldsymbol{s}} \cdot \nabla = d/ds$, then

$$(\boldsymbol{B} \cdot \nabla)\boldsymbol{B} = B^2 \frac{d}{ds}(\hat{\boldsymbol{s}}) + \hat{\boldsymbol{s}} \frac{d}{ds}\left(\frac{B^2}{2}\right) = \frac{B^2}{R_{curv}}\hat{\boldsymbol{n}} + \nabla_{\shortparallel}\left(\frac{B^2}{2}\right) \tag{C.23}$$

where R_{curv} is the local radius of curvature of a field line, $\hat{\boldsymbol{n}}$ is a unit vector directed at the centre of curvature and $\nabla_{\shortparallel}$ measures the spatial rate of change along $\boldsymbol{B}$. Substitution into (C.20) gives

$$\boldsymbol{F}_m = \frac{B^2}{\mu_0 R_{curv}}\hat{\boldsymbol{n}} - \nabla_{\perp}\left(\frac{B^2}{2\mu_0}\right) \tag{C.24}$$

The magnetic force therefore results from curvature of the field lines, which are stressed along their length, and from the variation of magnetic pressure acroos field lines.

There are two non-trivial cases in which the magnetic force density vanishes. A current-free region has $\boldsymbol{J} = \boldsymbol{0}$ and hence zero $\boldsymbol{F}_m$. The second case of vanishing $\boldsymbol{F}_m$ arises when $\boldsymbol{J}$ is finite but parallel to $\boldsymbol{B}$. These force-free fields tend to occur when the plasma has low density, and the magnetospheric region of a pulsar is assumed to be approximately force-free environment.

Appendix D

Pulsar Tables

D.1 Regular Pulsars

By regular pulsars we mean pulsars that are neither X-ray binary pulsars or millisecond pulsars. The number of catalogued and known pulsars (of any type) is an estimated $\sim$ 1700 [64], as of 2007, and about 80% of these can be categorized as regular pulsars. The number depends to some degree on the survey, and how strict the requirements are for verification, but certainly it is $\gtrsim$ 1000 [65]. Empirical models based on this then esitmates the number of galactic pulsars to $\sim 10^5$, while the number of neutron stars should be in the millions, as many of these objects are too old to exhibit pulsar features. Table D.1ab contains the data for ordinary nominal radio pulsars that are used in Fig. 5.1 in Chapter 5, and are gathered from the ATNF Catalogue [68], of the Australia Telescope National Facility.

Name	P [ms]	Log B [G]	Name	P [ms]	Log B [G]
J1022+1001	16.453	8.9	B0531+21	33.084	12.6
J1019-5749	162.498	12.3	J0535-6935	200.511	12.2
J2235+1506	59.767	9.4	J0407+1607	25.701	9.2
J1811-1736	104.182	10.1	J1702-4310	240.523	12.9
B1820-11	279.828	11.8	J1622-4802	265.072	11.5
B1800-27	334.415	10.9	J1000-5149	255.677	11.7
J1334-5839	107.718	10.7	J1650-4921	156.399	11.7
J0134-2937	136.961	11.0	1822B-14	269.186	12.4
J1903+0925	357.154	12.6	J1753-1914	62.954	10.1
B1706-44	102.459	12.5	J0520-2553	241.642	10.9

Table D.1a *Data for 20 regular radio pulsars with $P < 0.375$ s. The magnetic field B is the estimated polar magnetic field strength.*

Name	P [ms]	Log B [G]	Name	P [ms]	Log B [G]
J1834-0742	788.353	12.7	J1740-3052	570.309	12.6
B1504-06	709.064	11.9	J0045-7319	926.276	12.3
J1141-6545	393.898	12.1	B2025+21	398.173	11.5
B1831-00	520.954	10.9	B0820+02	864.873	11.5
J1355-5747	2038.673	12.1	B2154+40	1525.265	12.4
B0105+68	1071.118	11.4	J0656-2228	1224.754	11.3
J0534-6703	1817.565	13.4	J0818-3232	2161.258	12.1
B1753+52	2391.396	12.3	J0737-3039B	2773.460	12.2
B2303+46	1066.371	11.9	SGR 1900+14	5168.900	14.8
J0656-2228	1224.754	11.2	J1841-0524	445.748	13.0

Table D.1b *Data for 20 regular radio pulsars with $P > 0.375$ s. The magnetic field B is the estimated polar magnetic field strength.*

D.2 X-ray Binary and Millisecond Pulsars

The total number of known X-ray binary pulsars are $\gtrsim 100$, though the number is uncertain. An X-ray pulsar source is often difficult to differentiate from a white dwarf or black hole source, and of the X-ray binaries known, many are as yet unclassified.

Name	P [s]	$\bar{L}$ [10^{30}J s^{-1}]	$-\dot{P}/P$ [yr^{-1}]
Her X-1	1.24	1.0	$9.9 \cdot 10^{-6}$
GX 1+4	122.00	3.0	$2.1 \cdot 10^{-2}$
4U 1627-67	7.68	0.6	$1.9 \cdot 10^{-4}$
SMC X-1	0.71	50.0	$7.1 \cdot 10^{-4}$
4U 0115+63	3.61	0.9	$3.2 \cdot 10^{-5}$
GX 301-2	700.00	0.3	$4.5 \cdot 10^{-3}$
Cen X-3	4.84	4.5	$2.8 \cdot 10^{-4}$
Vela X-1	283.00	0.1	$3.6 \cdot 10^{-5}$
X Per	836.00	$4 \cdot 10^{-4}$	$1.2 \cdot 10^{-4}$
A 0535+26	104.00	6.0	$3.0 \cdot 10^{-2}$

Table D.2 *Data for 10 X-ray binary pulsars. The magnetic field B is the estimated polar magnetic field strength. The upper pulsars are LMXB, while the lower are HMXB.*

In Table D.2, I have put together data for 10 of the most well known X-ray binary pulsars. These data are used in Fig. 4.4 in Chapter 4, and gathered from [65]. Of the total number

of known X-ray binary pulsars however, the large majority are HMXB. So far there are only known a handful LMXB ($\lesssim 10$), that are pulsars, and only 3-4 of them have been sufficiently charted so as to give away reliable data.

Millisecond Pulsars

The number of confirmed millisecond pulsars known today are well above 100 [64]. These figures are rising steadily due to the recent discoveries of many such objects in globular clusters [66], which seems to be rich breeding grounds for millisecond pulsars due to exchange events in the dense cluster core, resulting in the capture of an old neutron star by an evolving star.

The real number of millisecond pulsars however, is higher, as not all pulsars with millisecond periods are labeled as millisecond pulsars. Very young pulsars such as the Crab Pulsar spin with a millisecond period ($\sim$ 33 ms), but are not grouped with the millisecond pulsars because their rapid loss of angular momentum suggests a strong magnetic field and a recent birth. In Table D.3 there are gathered data for some radio millisecond pulsars that are used in Fig. 5.1 in Chapter 5 [64].

Name	P [ms]	Log B [G]	P_{orb} [d]
B1937+21	1.558	8.6	n.a.
J1843111	1.846	8.1	n.a.
J17441134	4.075	8.3	n.a.
J00340534	1.877	7.9	1.59
J19093744	2.947	8.3	1.53
B1855+09	5.362	8.5	12.33
B1257+12	6.219	8.6	Planetary system
J10454509	7.474	8.5	4.08
J17575322	8.870	8.7	0.45
J18042717	9.343	8.8	11.13

Table D.3 *Data for 10 millisecond pulsars. The magnetic field B is the estimated polar magnetic field strength. The upper pulsars are isolated pulsars, while the lower are in binary systems, or in fact in planetary systems.*

As mentioned, only a few millisecond pulsars are accreting X-ray pulsars, and the few that are known have been discovered very recently. In Table D.4, we see some data for these systems, collected from [69]. We see that these systems are extremely close binaries, some with a binary period as short as half an hour. All of them are low-luminosity transients

with low mass accretion rates. It appears that the magnetic fields of these objects is of the same order as for most millisecond pulsars $\sim 10^8 - 10^9$ s [67].

Name	Year	P [ms]	P_{orb} [h]
SAX J1808.4-3658	1998	2.494	2.01
XTE J1751-305	2002	2.299	0.71
XTE J0929-314	2002	5.405	0.73
XTE J1807-294	2003	5.236	0.68
XTE J1814-338	2003	3.185	4.27
IGR J00291+5934	2004	1.669	2.46
HETE J1900.1-2455	2005	2.653	1.39

Table D.4 *Data for the seven presently known accreting X-ray binary millisecond pulsars*